ION PERMEATION THROUGH GRAPHENE OXIDE MEMBRANES

A thesis submitted to
The University of Manchester
for the Degree of Doctor of Philosophy
in the Faculty of Science & Engineering

2018

JIJO ABRAHAM

SCHOOL OF PHYSICS AND ASTRONOMY

Blank Page

Table of Contents

Word Count: 43228

Blank Page

List of Figures

List of Tables

Blank Page

Abstract

Graphene oxide (GO), a promising membrane material consisting of oxygenated graphene sheets, hosts a wealth of physicochemical properties such as exceptional chemical stability, flexibility, hygro-responsivity, ultrafast water permeation and exceptional molecular sieving properties, to list a few. However their use in desalination applications requires a stable sub nanometre channels, which are difficult to achieve in GO due to hydration mediated swelling of graphene capillaries. The work presented in this thesis mainly describes how to achieve tunable and swelling controlled sub nanometre capillaries in GO membranes by physical confinement, ion/water transport through such capillaries and the governing transport mechanism. GO membrane with interlayer spacing in the range of ~6-10 Å was obtained by utilizing its hygro-responsive property and the subsequent physical confinement by epoxy resin limits the swelling. The epoxy resin acts as physical wall on both sides of the GO laminates, restricting the capillaries from hydration when exposed to water. Regardless of the steric effects, ions still pass through these channels even though the channel size is smaller than the hydrated ion diameter size. This unique observation of violation of steric effects in sub nanometre channel cases is explained by a phenomenon called dehydration. Beyond the sake of fundamental understanding of the transport mechanism in sub nanometre capillaries, our results open the door for developing GO membranes with dehydration mediated ion selectivity for water desalination and separation applications.

Blank Page

Declaration

No portion of the work referred to in the thesis has been submitted in support of an application for another degree or qualification of this or any other university or other institute of learning.

Blank Page

Copyright Statement

i. The author of this thesis (including any appendices and/or schedules to this thesis) owns certain copyright or related rights in it (the "Copyright") and s/he has given The University of Manchester certain rights to use such Copyright, including for administrative purposes.

ii. Copies of this thesis, either in full or in extracts and whether in hard or electronic copy, may be made only in accordance with the Copyright, Designs and Patents Act 1988 (as amended) and regulations issued under it or, where appropriate, in accordance with licensing agreements which the University has from time to time. This page must form part of any such copies made.

iii. The ownership of certain Copyright, patents, designs, trademarks and other intellectual property (the "Intellectual Property") and any reproductions of copyright works in the thesis, for example graphs and tables ("Reproductions"), which may be described in this thesis, may not be owned by the author and may be owned by third parties. Such Intellectual Property and Reproductions cannot and must not be made available for use without the prior written permission of the owner(s) of the relevant Intellectual Property and/or Reproductions.

iv. Further information on the conditions under which disclosure, publication and commercialisation of this thesis, the Copyright and any Intellectual Property and/or Reproductions described in it may take place is available in the University IP Policy (see http://documents.manchester.ac.uk/DocuInfo.aspx?DocID=24420), in any relevant Thesis restriction declarations deposited in the University Library, The University Library's regulations (see http://www.library .manchester.ac.uk/ about/regulations/) and in The University's policy on Presentation of Theses

Blank Page

Dedicated to my loving family...................

Blank Page

Acknowledgement

First of all, I would like to begin the acknowledgement mentioning my supervisor. When I got the PhD offer from the University of Manchester to work on graphene based membranes, I felt very happy, but at the same time, anxious. My PhD supervisor is Prof Rahul R Nair, who is already well known in the graphene community. He was about to start his group at Manchester, with me being his first PhD student. There's always pressure for all the supervisor's first PhD students and my case was also not an exception. The first two years of my PhD life were stressful but my guide, Prof Rahul R Nair, who patiently waited for the research output I delivered and stood with me in all my difficult times. He is such a hardworking and dynamic researcher who always wants to mine down to the central core of a research problem. He is known for his simplicity and always opens the door for discussion and you can meet him for discussion at any time, even in the night. It is from him I started learning many things; how to do the science and writing skills in particular. One of the many remarkable things about Rahul is his ability to attract and fill his lab with a wonderful group of people. There were only 2 people when, I joined, now there is a team of 15, four years later. Rahul, I am very grateful to have had the chance to work with you and thank you for the guidance and supervision over the years.

Secondly I express my sincere gratitude to Sir Andre Geim and his wife Prof Irina Grigorieva. The fruitful discussion we had with Andre helped a lot in understanding more aspects of the dehydration mechanism we proposed in our paper and the corrections he made in the manuscript have resulted in the quality improvement of the paper and ended up in publishing in a reputed scientific journal. Irina was my main supervisor when I joined and became the co-supervisor when Rahul got the readership in Physics. I thank you for all the assistance and support you offered to me during my PhD study at the University of Manchester.

A deep sense of gratitude to the simulation and modelling collaborators: Dr Paola Carbone, Dr Christopher D. Williams and Dr James Dix from School of Chemical Engineering and Analytical Science. Their wonderful simulation work and theories helped to better elucidate the ion transport mechanism in GO membranes. It was nice experience collaborating with such great people.

A special mention goes to Mr. Paul Lythgoe and Mr. Alastair Bewsher of Williamson Research Centre, School of Earth, Atmospheric and Environmental Sciences for their help and support in analysing the chemical composition of the sample we gave after the diffusion experiments. These two people deserve a great acknowledgement as they were instrumental behind the successful finish of our research project on controlling GO hydration by confinement. Dear Paul and Alastair, you were truly amazing!!

During my PhD study at Manchester, I was lucky to have a great number of people to work with. I would like to mention the names of all those smart minds of our lab for their cooperation, useful discussions and for creating a friendly atmosphere in the lab. The names appear in chronological order: Dr Su Yang, Dr Vasu Siddeswara Kalangi, Dr Christie Thomas Cherian, Dr Kai-Ge Zhou, Kun Huang, Chengyi Hu, Chenglong Chi, Vishnu Sreepal, Dr Amritroop Achari, Dr Avishek Pal, Tobias Bohn, Hui Xiao, Danny Wagemans and Dr Premlal B Pillai. Working with them was a real pleasure. Besides being my lab mates, these people were also all good friends to me and together we shared nice memories in our group gathering, especially in our food parties. Special thanks to Tobias, Vasu, Amritroop, Su Yang and Christie for proof reading the thesis. Their comments and suggestions have helped to increase the quality of the thesis. I am grateful to Dr Kalon Gopinadhan from Andre's lab, who taught me the basics of electrical ion transport measurements and made me familiar with LabVIEW software's.

I am very much thankful for the technical support offered by Mark Sellers, Paul Richardson and Stan Gillott of School of Physics. Of these people, Stan retired from the service in 2015; he was the mockery machine of condensed matter physics group, who always made fun of me. They are approachable, relaxed guys and made many permeation devices for me and finished all the jobs I have given in a timely fashion. Dear Mark, Paul and Stan, I am very much thankful to you for all the services you have provided. I would like to mention one more name in this section, Mr.Jonathan Hird from Physics Rapid Prototyping Facility, who helped me a lot in the final year of my PhD.

During my PhD period at Manchester, myself and Christie ordered many things in the beginning when Rahul was setting up the lab in NGI. I was a regular visitor of the Physics and NGI store. People there in both the stores, Mr Rowan Holland, Mr Chris Livingston, Mr Noel Ogden, Mr Michael Musgrave are so generous to me and treated me like a friend. If something went wrong with the delivery, they are very keen in sorting out the things which makes me feeling relaxed. Thank you all for all your assistances.

The financial assistance I got from Lockheed Martin is gratefully acknowledged.

I must mention one name here, Prof N.V Unnikrishnan from School of Pure and Applied Physics, Mahatma Gandhi University, Kottayam who recommended me for the PhD position. He is an amazing mentor and always supportive of his students. Dear Prof Unnikrishnan, without your support and help, I won't get this opportunity to work in such a vibrant atmosphere.

Besides the research life, I am thankful to Prof Rahul R Nair and his wife Mrs Anju N Nair for their hospitality and affection.

Heartfelt thanks to my roomie and badminton company: Dr.Vinod Kumar Puthiyapura, a continental specialist and a good critic who always provokes me with his jokes. Thank you very much for all the nice memories.

There are some special friends I got from Manchester outside of academia who are now a part of daily life. Of these, Fr Thomas Thaikkottathil MST was my companion, moreover a friend and together we had many journeys. Fr, thank you for all the support. Mr Anil Adhikaram, Mrs Tessmol Anil, Mr Joseph Mathai, Mrs Jincymole Joseph, Mr. Tony Kurian, Mrs. Ani George and their children are some others to name but a few. They cooked and cared for me. Their constant support and unconditional love makes me feel like being in home. Thank you very much for all those awesome memories.

Here comes the most integral part of my life, my family. Pappa, mummy and my two sisters: Jiji and Jilu. Dear pappa and mummy, thank you very much for not refusing my request to go to UK when I got the PhD offer from the University of Manchester. Very special thanks to my sisters Jiji and Jilu for your constant encouragement and support, which made me who I am today. You are simply amazing and special mention to both of you for taking care of our mother in the finishing stage of my PhD and sorting out all the troubles we faced.

Finally and foremost, I would like to thank God Almighty for giving me the strength, knowledge and courage to undertake this PhD study.

Blank Page

Preface

Graphene is a single atomic plane of graphite which exhibits many unusual properties. It is the thinnest material ever known to science, and, hosts a high quality and unique electron system, good conductor of heat and electricity, nearly 100% transparent; the list is endless. The unique electronic band structure resulted from the confinement of electrons in two-dimensional (2D) honeycomb carbon lattice has led to new exciting quantum phenomena, even today. Similar to electron transport, graphene and its derivatives have special fingerprints in the field of research in molecular transport. However for observing such exotic behaviour, ions/molecules must be confined to an extremely small space, analogous to the electron confinement in 2D plane of graphene. The successful exfoliation of graphene derivatives, graphene oxide (GO) in particular has started the quest for molecular self-assembling approach to construct membranes by restacking of the exfoliated sheets. Moreover, while restacking individual GO sheets into a membrane structure, a new space is formed in between two mutually facing GO sheets, known as interlayer space, where water, ions/molecules can be confined and move under the constraint of GO sheets. The little fraction of this atomically thin volume in the membrane is well connected across its thickness, providing networks of tiny capillaries, through which mass transport occurs. As indicated, the interlayer space in the membrane provides a new room to confine ions/molecules by restricting the mass transport in two dimensions. Particularly, the ion transport in GO membranes strongly depends on the level of confinement that one can achieve in GO. Owing to the notable hygroscopic property of GO, the interlayer space varies reversibly between 6-10 Å with the humidity. Moreover, it further expands to~ 13-14 Å when GO is exposed to liquid water. If we remove the graphene thickness from interlayer spacing, the available effective free space is close to 10 Å which is larger than the hydrated diameters of any common salts, limiting the observation of ion size effects. Here, we have developed a new strategy to fabricate GO membrane with an interlayer space in the range of sub nanometre by physical confinement and studied the ion transport under such extreme confined regions. We have achieved an interlayer spacing even down to~6 Å using this method. In addition, when the interlayer spacing is decreased to sub-nanometres, a new transport regime has emerged, where the capillary size is smaller than the hydrated ion diameter size. The work presented in this thesis mainly focuses on the ion transport through this new regime, which hasn't been demonstrated experimentally in GO so far. The thesis entitled **"Ion Permeation through Graphene Oxide Membranes"** is organized into 5 chapters

Chapter 1: General Overview of Two Dimensional Materials is an updated survey on what has been achieved so far in the two-dimensional materials world. General overviews of all currently existing 2D materials are provided, with more emphasis on two families of materials, graphene and 2D transition metal dichalcogenides (TMDCs). Three members are chosen from graphene family, including, graphene, GO, hexagonal boron nitride (hBN) and the other contain all the 2D TMDCs that have been discovered so far. The status and prospects of these two families of materials is presented in the first chapter.

Chapter 2: Introduction to Graphene-based Membranes examines the current graphene-based membrane research, the progress achieved and the current status. Depending on the pathway for the mass transport of water, ions or molecules, chapter is divided into three different sections: molecular transport through (1) artificially created pores/ inherent pores in CVD grown/mechanically exfoliated graphene; (2) artificial angstrom scale graphene channels by van der Waals assembly of graphene crystals; (3) assembled GO laminate. Fabrication procedure of corresponding transport pathway, governing transport mechanisms and the applications in desalination, gas/ion separation and other properties are summarized.

Chapter 3: Characterization Techniques and Methodology presents a brief overview of the main characterization techniques and the methodology adopted in the entire study. The chapter is divided into two parts. The first part describes the research methodology and the material synthesis and the second one presents the physical characterization techniques used in this study. A brief outline of the working principle of the experimental tools used is also mentioned.

Chapter 4: Tunable sieving of ions using graphene oxide membranes presents the first experimental evidence for the ion dehydration in sub nanometre pores published last year. The dehydration mediated selectivity in sub-nanometre graphene capillaries is the main theme of the finding.

Chapter 5: Conclusions and Future Outlook briefs the main conclusions of the work presented in this thesis with an outlook to future possible directions/ avenues to be explored.

Chapter 1- General Overview of Two-Dimensional Materials

Blank Page

1.1 Introduction

Since the isolation of graphene in 2004, there is a growing interest in the synthesis, characterization and application exploration of 2D materials as evident from the exponential increase in the number of articles and reviews related to 2D materials appearing in the areas of physics, chemistry and materials science. Research on 2D materials is now in the forefront of research attention; new members are continuallybeing added into the 2D library and this research direction is likely to remain one of the most intense topics for upcoming years. Some remarkable changes in the properties of the material occur when charge and heat transport is confined to a single plane and the emergence of such unusual phenomena may lead to many scientific breakthroughs. In short, two-dimensional materials are single layer materials in which atomic arrangement and bond strength in two dimensions are similar but larger than along the third dimension[1]. By far the best known material is graphene, but there is a large and growing family of other 2D materials with unique functionalities that promise to revolutionize the materials world. With the development of new synthesis methods, many novel materials, which only existed theoretically, have been realized and started manifesting its unique properties, for example silicene[2-4] and germanane[5, 6]. The most common class of crystalline materials that can be exfoliated into layered sheets down to single atom or few-atom polyhedral thick layers are layered van der Waals (vdW) solids. Their crystal structure consists of single-atom-thick or polyhedral-thick layers of atoms that are covalently or ionically bonded along their plane and the layers are held together by weak van der Waals bonding along the third axis. The weak out of plane van der Waals interaction facilitate the exfoliation of the 3D material into 2D sheets. A few decades back Frindt *et al.* showed the possibility to exfoliate layered van der Waals materials, such as TMDCs into single/few layers by mechanical/chemical exfoliation[7-10]. A huge surge of interest in the synthesis and exfoliation of 2D materials has risen with the exfoliation of graphene and the past 12 years of graphene research has offered many protocols for the synthesis, characterization, detection, transfer, and manipulation of the properties of layered van der Waals materials. Among the 2D family, graphene is apparently the most versatile and intriguing member owing to its wealth of electronic, mechanical and optical properties, the second place goes to 2D hexagonal boron nitride (hBN) or white graphene[11] and 2D TMDCs probably in the next place with more emphasis on MoS_2.The current members in the family of 2D materials is given in table 1.1.

Another interesting class of 2D materials are oxides including monolayers of TiO_2, MoO_3, WO_3, mica and perovskite-like crystals such as BSCCO and $Sr_2Nb_3O_{10}$ to name a few[12-16] (Table 1.1).

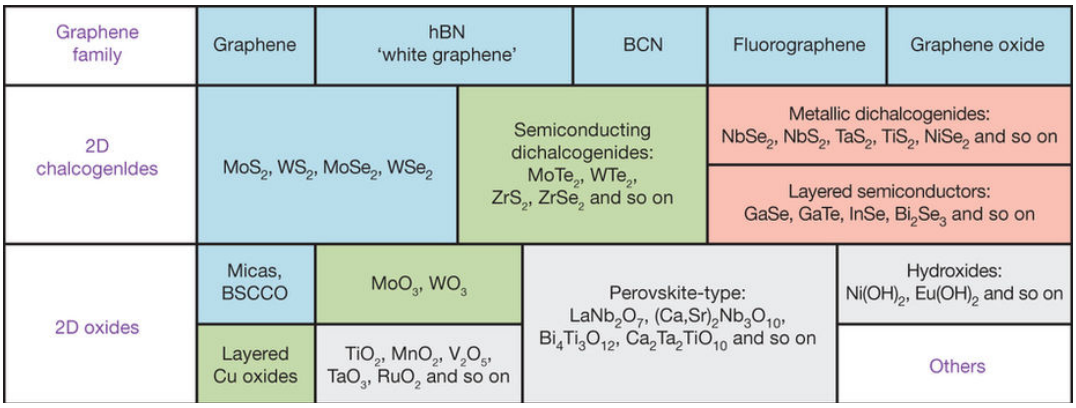

Graphene family	Graphene	hBN 'white graphene'	BCN	Fluorographene	Graphene oxide
2D chalcogenides	MoS_2, WS_2, $MoSe_2$, WSe_2	Semiconducting dichalcogenides: $MoTe_2$, WTe_2, ZrS_2, $ZrSe_2$ and so on		Metallic dichalcogenides: $NbSe_2$, NbS_2, TaS_2, TiS_2, $NiSe_2$ and so on	
				Layered semiconductors: GaSe, GaTe, InSe, Bi_2Se_3 and so on	
2D oxides	Micas, BSCCO	MoO_3, WO_3	Perovskite-type: $LaNb_2O_7$, $(Ca,Sr)_2Nb_3O_{10}$, $Bi_4Ti_3O_{12}$, $Ca_2Ta_2TiO_{10}$ and so on	Hydroxides: $Ni(OH)_2$, $Eu(OH)_2$ and so on	
	Layered Cu oxides	TiO_2, MnO_2, V_2O_5, TaO_3, RuO_2 and so on		Others	

Table 1.1 Current members of the 2D family. *Stable and unstable monolayers in ambient condition are given in shaded blue and green; shaded grey region indicates 3D compounds exfoliatable into single layer sheets. 'Others' include borides, carbides, nitrides. BCN, boron carbon nitride. Adapted from ref*[11]*.Copyright 2013, Springer Nature.*

The chapter briefly outlines the different 2D materials, their status and prospects. Based on the fundamental aspects and technological applications; two families of 2D materials are chosen for the detailed discussion, which includes graphene, hBN and graphene oxide from the graphene family and the other include all the 2D-TMDCs discovered so far. The fundamental properties, material synthesis and applications of the 2D materials are included in each section.

1.2 Graphene

1.2.1 Graphene: a general outlook

Carbon is the most intriguing and versatile element in the periodic table as it is able to form many allotropes. Diamond and graphite [17-23] are widely known three dimensional (3D) allotropes of carbon and studied for centuries. The (0D) fullerene, 1D carbon nanotube (CNT)[24-30] and the relatively new 2D form of carbon allotrope i.e. graphene are other notable discoveries in the past three decades. Specifically, graphene or 2D graphite, obtained recently in 2004, has already shown potential for a wide variety of applications and attracted attention among material scientist, physicist and chemist alike to unveil all its exotic fundamental properties. Graphene is the most studied carbon allotrope theoretically and its electronic properties have been a subject of intense theoretical interest for sixty years[31, 32] and the experimental realization occurred only forty years later[33].Graphene is the first stable monolayer thick material where carbon atoms in two dimensions are tightly-packed into a 2D honeycomb lattice. Graphene: also described as the mother of all graphitic structures because it is the primitive building block for all graphitic materials[34] (Figure 1.1a). Graphite is a layered material consisting of individual graphene sheets stacked on top of each other. The weak coupling between individual graphene layers helped Manchester scientists; Sir Andre Geim and Sir Kostya Novoselov to isolate single graphene sheet from graphite using a technique called micromechanical cleavage [33, 35]. The idea is seemingly simple, elegant and remarkably easier to obtain clean graphene sheets. The method involves a scotch tape to peel off flakes of graphite from a chunk of highly ordered pyrolytic graphite (HOPG) and which were subsequently transferred onto an oxidised silicon wafer. Peeling and sticking the flakes several times will bring down the graphite flake to its single atomic thickness. Following the isolation of graphene, majority of the scientific community has focused on graphene for studying its optical, mechanical and electronic properties and graphene suddenly became a star in the material science. For the pioneering work regarding two-dimensional atomic crystals and for revealing its 2-dimensional properties, Sir Andre Geim and Sir Kostya Novoselov shared the 2010 Nobel Prize in Physics. In graphene, the carbon atoms are sp^2 hybridized with a carbon-to-carbon inter-atomic length of 1.42 Å [36, 37]. The atoms are located at the corners of the hexagons and the lattice can be visualized consisting of two interpenetrating triangular sub-lattices A and B, containing two carbon atoms per unit cell

(Figure 1.1b) with a lattice constant $a \approx 2.45$ Å[38, 39]. The atoms at the lattice site of one sub-lattice (i.e. A) are at the centre of the triangles defined by the neighbouring sub-lattice (i.e. B) which are interpenetrated to the former. Each carbon atoms forms σ bonds with each other by the superposition of the s, p_x and p_y orbitals of the carbon atoms, leaving the p_z orbital unhybridized (Figure 1.1c). The sp^2 hybridized orbital is trigonal planar by geometry and the spare p_z orbital overlaps with the next closest carbon atom to form the π^* (conduction) and π (valence) bands.

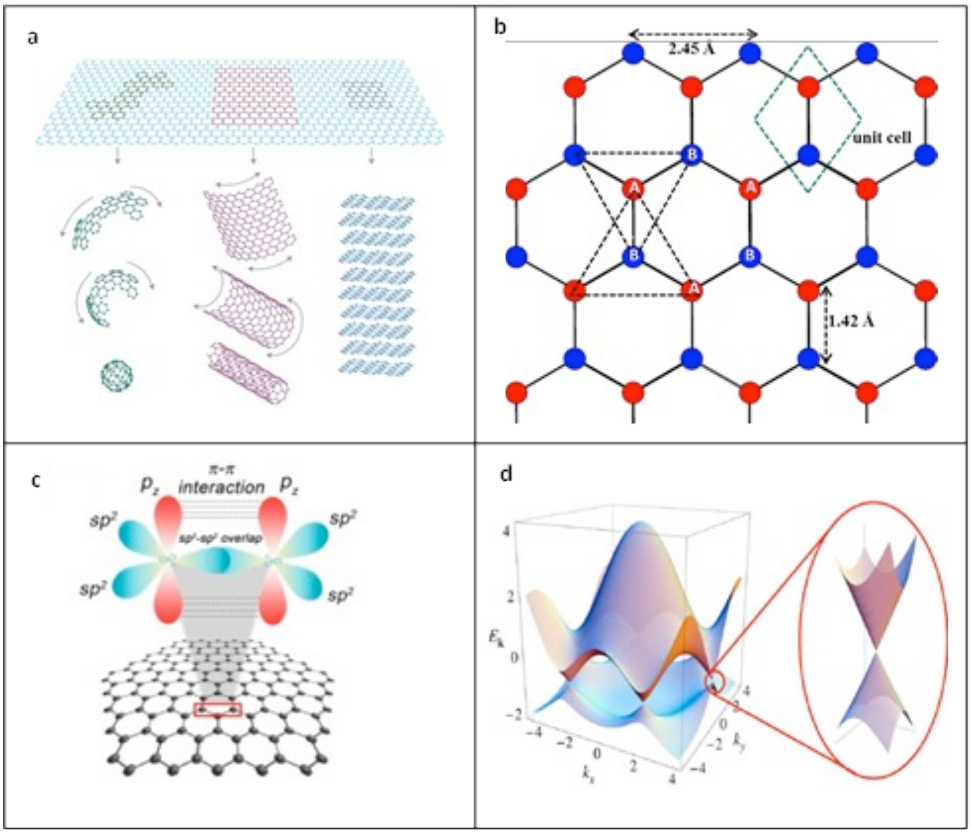

Figure 1.1 Atomic and electronic structure of graphene. ***(a)*** *Also known as the mother of graphitic structures, can be wrapped into 0D fullerenes, rolled into tiny 1D carbon nanotube or stacked into 3D graphite. Adapted from ref*[40]*.Copyright 2007, Springer Nature.* ***(b)*** *Crystal structure of graphene, honeycomb graphene lattice consists of two interpenetrating triangular sub-lattices. The atoms at the lattice site of one sub-lattice are at the centre of the triangles defined by the neighbouring sub-lattice. The lattice has two carbon atoms per unit cell and is invariant under 120° rotation around any lattice site.* ***(c)*** *sp^2 hybridized carbon atoms in graphene. Adapted from ref*[41]*.* ***(d)*** *Band structure of graphene. The six Dirac cones are positioned on a hexagonal lattice where valence band meets the conduction band. Reproduced from ref*[42]*.Copyright 2009, American Physical Society.*

Notably, it is these π electrons that are responsible for the extraordinary electronic properties of graphene. The sp^2 hybridized carbon atom in graphene is responsible for its high mechanical strength. The stacking in graphite is either ABAB (Bernal type) or ABCABC (rhombohedral type) with an interplanar distance of 3.45 Å.

1.2.2 Properties

Graphene is a zero band gap semiconductor (Figure 1.1d) and the electrons in graphene are considered as massless Dirac fermions with speed, 1/300 the speed of light, showing micrometre-scale ballistic transport even at room temperature[43, 44]. The carrier mobility value varies from 500 to 50 0000 $cm^2\ V^{-1}\ s^{-1}$ for the substrate supported and 10^5 to 10^6 $cm^2V^{-1}\ s^{-1}$ for the suspended and annealed samples, the largest reported value for a semiconductor or a semimetal[33, 35, 45-48]. Graphite crystals become optically transparent when exfoliated down to monolayers with an opacity of only 2.3%[49], depending only on the fine structure constant $\alpha = 2\pi e^2/hc$ = 1/137 (c, the speed of light). Such characteristic has possible advantages as transparent electrodes for solar cell applications and flexible displays[50]. The transmittance for a 2 nm thick graphene films is as high as above 95% and decreases with increasing thickness[51, 52]. The optical spectrum of graphene is flat and featureless in the range of 500 to 3000 nm and the absorption becomes dominant only below 400 nm[53]. All the carbon allotropes, graphite, diamond and carbon nanotubes are well known for its high mechanical strength and graphene is also not an exception to the list. It is the strongest material ever measured[54], stiffness of the order of 300–400 N/m with a breaking strength of 42 N/m. The material yield an intrinsic tensile strength of 130.5 GPa and its Young's modulus is approximately 0.5–1.0 TPa, close to the value for bulk graphite[55]. All these demonstrate its high mechanical strength which could find application in nano electromechanical systems as pressure sensors and resonators[56]. In addition to its atomic thinness and extraordinary mechanical properties, the material also exhibits an extremely high thermal conductivity of the order of 5000 $W\ m^{-1}\ K^{-1}$[57] and an exceptionally great surface area of2630 $m^2\ g^{-1}$.The reported value for graphene's thermal conductivity is superior to the value reported for any conventional material and outperforms individual suspended CNTs even[58, 59].

1.2.3 Production

Mechanical exfoliations using scotch tape method and epitaxial growth by chemical vapour deposition (CVD) are the two notable techniques for the production of graphene sheets. Graphene crystals could be easily exfoliated from bulk graphite by simple scotch tape method via repeated stick and peal process. This process eventually brings the graphite to monolayer thickness and exfoliated graphene sheet can be visualised by transferring to Si/SiO2 substrate (oxide layer thickness of either 300 or 90 nm[60-62]). Mechanical exfoliation by scotch tape technique is a top-down; low cost and simple method for the production of high quality graphene. It requires neither sophisticated equipment nor complex synthesis route for the production. The uneven flake distribution and limited industrial scalability are the practical limitations of this technique. Single/few-layer graphene can also be produced by bottom-up epitaxial growth technique [63-65]. Here the films are grown epitaxially by chemical vapour deposition of hydrocarbons on metal substrates or by decomposition of hydrocarbons [66-68]. Although the CVD growth technique is scalable enough to produce centimetre-sized continuous graphene films[69], the formation of different single crystal domains or grain boundaries within the same graphene layer would have a dominant effect on the mobility of the charge carriers. The reported mobility is lower compared to mechanically exfoliated graphene.

1.2.4 Applications

Due to the exceptional mechanical, electronic and thermal properties, graphene is believed to find application in diverse fields. Electronic industry: companies like Intel and IBM are investing in graphene research because of its rich electronics; mainly the high mobility of the charge carriers. By inducing band gap in graphene, it can be used in graphene based field-effect transistor (FET) devices [70, 71]. Graphene can also be employed in wearable electronic gadgets such as e-textiles and watches/cell phones due to its high flexibility and good optical transmittance [72, 73]. In addition to the use of graphene in electronic/ wearable electronics, the good chemical response of the graphene makes it interesting for gas sensing applications. The molecules adsorption onto the graphene will lead to the charge transfer from the graphene sheet and this phenomenon is used to detect a variety of species from gases to biomolecules[74-79].The high electrical conductivity, optical transparency, and carrier mobility of graphene show great promise to use as transparent conductive films (TCFs) in mobiles and tablets. Films can be spray coated onto any substrates either directly from aqueous reduced graphene oxide (rGO) suspensions or from the GO suspensions followed by chemical reduction. TCFs can be deposited on glass, quartz, or poly methyl methacrylate (PMMA) substrates[80].Layer-by-layer assembly of GO sheets followed by reduction yield a transmittance of 95.4% at 650 nm wavelength[81]. High surface area of graphene and the potential to make the charge transfer easier along its two-dimensional surface make graphene an interesting candidate as electrode material in clean energy devices[82]. Graphene-based electrodes are started using in rechargeable lithium ion batteries (RLBs) and electrochemical double layer capacitors (EDLCs)[83-87].Graphene-polymer nanocomposites is another interesting field where graphene could be widely employed[88-91].

1.3 Graphene Oxide

1.3.1 Graphene Oxide: a chemical derivative of graphene

Graphene oxide is an atomically thin, two dimensional layered material consists of hydrophilic oxygenated graphene sheets, containing hydroxyl and epoxy groups on the basal plane; smaller amounts of hydroxyl, carboxyl, ketone, and ester groups on the edges[92-94]which together gives GO excellent dispersibility in water. The research interest on GO has witnessed an exponential increase for the last 10 years, covering all its fundamental and technological aspects, which includes the possibility to create membrane for desalination[95], utilizing its ability to modify the surface functionalization for biomedical[96-98] and energy storage applications[99]. The oxygen enriched functional groups on the GO sheets influence the electronic, mechanical, and electrochemical properties differentiating GO from pristine graphene sheets, despite their similar backbone carbon structure and monolayer thickness. The oxygen containing functional groups act as active sites for the modification of the physicochemical properties of GO nanosheets via covalent or non-covalent attachment to design GO for a specific application[100, 101].Unlike graphene, GO is a poor conductor of electricity due to the presence of adsorbates which induce an energy gap in the electron density of states [102-104]. Single layer GO crystallites have three types of regions: holes, oxidized and pristine graphene regions. Their relative sizes depend very much on details of GO preparation (different degree of oxidation). In GO, 40-60% of the carbon atoms in the basal plane are sp^2 hybridized, without affected by oxidation with O/C ratio of 1:5[94, 105]. GO sheets consist of sp^2 and sp^3-hybridized carbons, both arranged in a hexagonal manner. As the presence of both sp^2 and sp^3 clusters in GO make it an electronically hybrid material consists of both conducting and non-conducting path originating from π-states and σ-states of sp^2 and sp^3 hybridized carbon atoms. Reduction is versatile protocol to tune the band gap of GO with a possibility to convert GO from its insulating nature to a semiconducting and graphene like semi-metal by controlling the amount of sp^2 and sp^3 clusters [94, 106]. More specifically, the electrical conductivity of the graphene oxide sheet can be recovered by rebuilding the π –network by controlled reduction using reducing agents which will remove the C-O bonds within the GO sheets, ending up with a product known as reduced graphene oxide with a distorted lattice structure. As expected, rGO shows significantly small carrier mobility compared to pristine graphene sheet[107, 108]. The precise atomic structure of GO is still unclear because of the non-stoichiometric atomic composition of the parent graphite oxide. The primary reasons include variations in sample to sample due to different synthesis routes, difference in the extend of oxidation and hygro-responsive nature of graphite oxide. The oxygen functionalities attached to the graphene sheets will adsorb the water molecules into the inter layer galleries and the water adsorption will increase with increasing humidity, which result in the swelling of GO film.

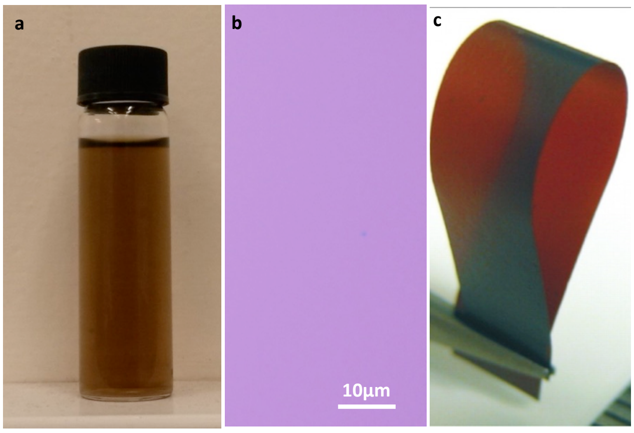

***Figure 1.2 Graphene Oxide: an oxygenated graphene sheet (a)** Photograph of a graphene oxide suspension; GO sheets dispersed in water, concentration=1mg/mL). **(b)** Optical micrograph of GO sheets deposited on 150nm SiO2/Si. **(c)** Photograph of a 5µm thick GO paper showing its semi transparency and flexibility in handling. Image is adapted from ref[109].Copyright 2007, Springer Nature.*

Interlayer distance in a multilayer GO stack varies from~6-14 Å, depending on the water content inside [95, 110, 111]. GO is usually prepared by mild sonication of the graphite oxide slurry. The suspension has a mostly monolayer GO crystallites with lateral dimension ranges few nm to several micrometres[112] and an average roughness of 0.6 nm[105]. The size of GO sheets depends on the flake size of starting graphite, the oxidation time and the type of oxidation procedure[113, 114]. Although graphite oxide has been known to the research community since 1855, the research interest in GO has propelled with the isolation of graphene in 2004[82, 100]. GO paper was prepared by Ruoff's group[109] for the first time in 2007 (Figure 1.2c)by the self-assembly of individual GO sheets, exhibiting extraordinary flexibility and excellent mechanical properties. A typical GO suspension has a brownish colour depending on its concentration. When assembled into paper form; appears as dark brown under transmitted white light and nearly black in reflection when the thickness is higher than 5 micrometres[109].

1.3.2 Methods of preparation

GO is synthesized from the parent graphite material through oxidation in a strongly acidic environment and the first attempt was reported in 1859 by Brodie et.al[115].So far different GO synthesis procedures have been reported which includes Staudenmaier[116], Brodie[115],Hofmann[117], Hummers[118], and Tour methods[119] (Table 1.2). The atomic composition of the GO sheets differs from one method to the other because of different choices of oxidizing agents and the quality of the starting graphite material

Method	Oxidizing agent	Reaction media	Carbon-to oxygen ratio
Brodie[115]	$KClO_3$	$HNO_3 + H_2SO_4$	-
Staudenmaier[116]	$KClO_3$	Fuming HNO_3	1.17
Hofmann[117]	$KClO_3$	Non-fuming HNO_3	1.15
Hummers[118]	$KMnO_4 + NaNO_3$	Conc. H_2SO_4	0.84
Tour[119]	$KMnO_4$	$H_2SO_4 + H_3PO_4$	0.74

Table 1.2 Different synthesis route for the production of GO. *Reproduced from ref[120].Copyright 2014, Royal Society of Chemistry.*

1.3.3 Structural models

The chemical and atomic structure of GO is quite complex and has been a subject of debate in the graphene research field. To date, the chemical structure of GO is not clear and fully understood due to the non-stoichiometric and amorphous nature of the material. In spite of all the difficulties and challenges in understanding the atomic composition and stoichiometry of the compound, a significant and substantial effort has been made in understanding the structural properties of GO (Figure 1.3&Figure 1.4). Hofmann and Holst made the first attempt to understand the chemical structure of GO[117]. According to their model, epoxy groups are decorated at the sp^2 hybridized basal planes of graphite as a repeating unit with a net molecular formula of C_2O. A slight change to this model was put forward by Ruess in 1946 with the addition of hydroxyl groups onto the basal planes, accounting for the hydrogen content in the structure. However, Ruess model altered the hybridization of carbon atoms in the basal plane from sp^2 to sp^3 to include the hydroxyl groups in its basal structure. In 1969, Scholz and Boehm suggested a structure omitting the epoxide and ether groups; instead regular quinoidal species are added in place of the removed species which make the carbon network corrugated.

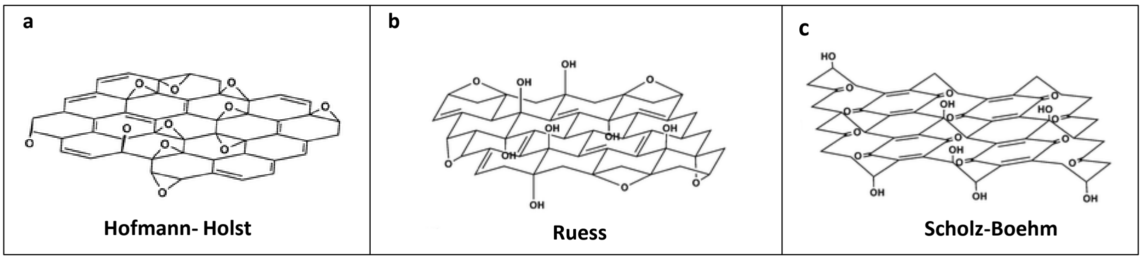

Figure 1.3 Several older structural models of GO. *Reproduced from[121], Copyright 2010,Royal Society of Chemistry and ref[92].Copyright 2006, American Chemical Society.*

The most widely accepted and well-known model was the one proposed by Lerf and Klinowski[122] which discarded the earlier lattice based models and concentrated on an amorphous non-stoichiometric substitutes. Both Lerf and Klinowski conducted several studies on the hydration dynamics of GO and their structural model is the most heavily cited one in the graphene research field. Based on the current understanding of experimental observations on functional modifications and hydration behaviour, GO sheets consists of hexagonal carbon networks with sp^2 (40-60%) and sp^3 hybridization differentiating it from pristine graphene sheets. The carbon atoms are covalently bonded to oxygen functional groups especially hydroxyl, epoxy, and carboxyl group. The covalent binding will generate *sp*^{3} clusters particularly known as oxidised region and the rest free from functionalization known as pristine region which are *sp*^{2} in nature, constitute the major portion of the GO. Among the oxygen functional groups, which are above or below the graphene sheet, epoxide and hydroxyl groups are attached to the aromatic rings, while carboxyl groups are most likely attached to the edges of the GO sheets.

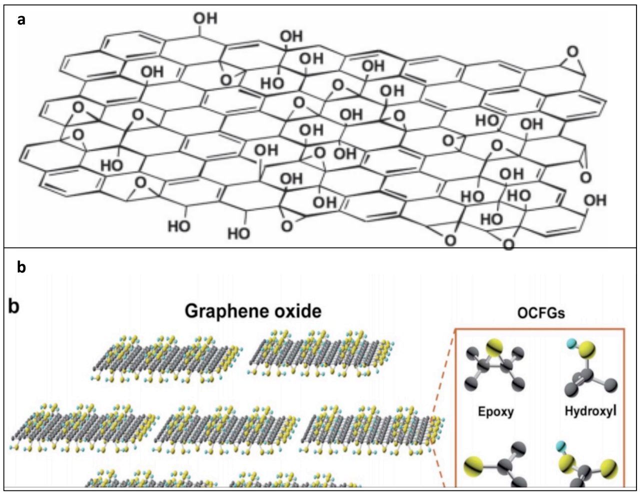

Figure 1.4 Widely acknowledged structural model of GO. (a) *Chemical structure of GO in the proposed Lerf-Klinowski model. Reproduced from ref 122, Copyright 1998 Elsevier Science* ***(b)*** *Schematic representation of the Lerf-Klinowski model. Reproduced from ref123.Copyright 2017, Royal Society of Chemistry*

1.3.4Applications

Although the presence of oxygen containing functional groups limits the usability of GO in electronic devices, it provides enhanced chemical activity compared to graphene which could be exploited in optical, thermal, mechanical, and electrochemical applications. Despite the insulating nature of GO, it can be made useful in electronic devices via chemical/thermal reduction of GO. Such converted graphene sheets still exhibit excellent conductivity despite defects and disorder [124-126]present after reduction. GO can be used as humidity sensor because of its affinity with water molecules [127-129]. As GO can be mass produced by simple, low cost synthesis method, it emerges as a good precursor for the fabrication of graphene-based TCFs. Another area where GO is employed is for the gas sensing applications. The functional groups attached on the graphene sheets facilitate the interactions with the gaseous molecules which make GO to sense various gaseous species

[130, 131]. Because of the intrinsic reactivity of the GO sheets, GO can be used for catalytic applications [132-134]. GO can also be employed as a filler to enhance the mechanical stability of polymer nanocomposites.[135]. GO for biomedical application is also getting wide-spread interest and was shown in the recent works such as; bio sensing [96, 97, 130, 136, 137], drug delivery [138-141] and therapeutic uses[142, 143]. Most of the research attention in the GO material has now focused on utilizing its self-assembling ability to form membrane which consists of tiny angstrom sized channels. Such membrane can act as selective channel for the transport of water and salt molecules which could be exploited in desalination and water filtration applications [95, 144-146].

1.4 Hexagonal Boron Nitride (hBN)

Boron nitride is a compound made up of boron (B) and nitrogen (N) atoms with the chemical formula BN. It is not a naturally occurring material but can be synthesized from a chemical reaction involving (H_3BO_3) or boron trioxide (B_2O_3) and KCN [147-149]. Due to the specific bonding involved in BN, it forms many polymorphs[150], such as cubic BN (c-BN), wurtzite BN (w-BN), hexagonal BN (h-BN)[151], rhombohedral BN (r-BN)[152] ,amorphous BN[153, 154], BN nanotubes[155], and BN nanomesh[156]. The most common crystalline structure of BN is h-BN and r-BN. Stacking order of h-BN is AB whereas it is ABC for r-BN. Among the list of all the polymorphs of boron nitride, h-BN has been widely studied due to the structural similarities with graphene (white graphene) [157]. With the isolation of graphene in 2004, many groups started examining the feasibility of the existence of 2D BN sheets, which resulted in the successful exfoliation of BN crystals a few years later. It has a high thermal conductivity (κ~484 W m^{-1} K^{-1}), is mechanically strong [158, 159](elastic constant of 220–510 N m^{-1} and Young's modulus of~1TPa) and can be used as a lubricant due to the week out–of-plane van der Waals bonding. The heteroatom B-N bonds are slightly ionic due to the difference in electronegativity of B and N atoms in comparison with the C-C bonds in graphitic structures. 2D h-BN sheet is a 2D insulator (bandgap of 5–6 eV) and structural analogous to graphene, as the sp^2 bonding and honeycomb lattice structure is shared in both materials. The sub lattices are occupied by an equal number of boron and nitrogen atoms with lattice parameters of a = 0.250 nm and c = 0.666 nm. The layers (002) are arranged with an interlayer spacing of 0.33-0.34 nm, close to graphite. The small lattice mismatch (1.5%[160]) between graphene and 2D-hBN makes the interaction with graphene sheets stronger which would further benefit 2D-hBN to be used in graphene-based electronic devices[161]. Several processing techniques have been reported recently for the fabrication of 2D-h-BN, including mechanical exfoliation[162, 163], liquid exfoliation[164-168], chemical vapor deposition[169-171] (CVD), physical vapor deposition (PVD)[172, 173], vapor phase epitaxy[174], pulse laser deposition (PLD)[175] and still more to follow. 2D h-BN is widely used as substrates for high quality graphene electronic devices[161, 176]. Taking advantage from its high thermal conductivity, BN nanomaterials can be employed as fillers in thermally conducting polymers to increase its thermal conductivity[177, 178]. Recent theoretical calculations show that BN sheets can also be employed as substrates for catalytic and sensing applications [179, 180] which were thought may be impossible before. Experimental and theoretical studies performed recently on BN nanotubes reveal its potential in osmotic power generation[181] and water treatment applications[182, 183].

1.5 2D transition metal dichalcogenides

The absence of band gap in graphene has stimulated the research in other two dimensional alternatives which exhibits semiconducting behaviour and transition metal dichalcogenides (TMDCs) is a promising substitute owing to its inherent semiconducting character. TMDCs are well-studied materials in the family of van der Waals solid displaying layered structure having strong in-plane bonds but weak out of plane van der Waals bonds, allowing exfoliation into 2D layers with single unit cell thickness. With the discovery of new exfoliation/synthesis routes, new materials are constantly being added into the 2D material family and TMDCs in particular.[1, 184, 185].TMDCs are semiconductors with a stoichiometric formula MX_2, where M is a transition metal atom from group IV (Ti, Zr ,Hf,), group V(like V, Nb, Ta, Re) or group VI (Mo,W etc.) and X is a chalcogen atom (S, Se , Te)[1, 186, 187].These materials show a layered structure in the form X–M–X, with metal atoms sandwiched between two hexagonal planes of chalcogen atoms (Figure 1.5). The current list of 2D TMDCs includes molybdenum disulfide (MoS2), molybdenum diselenide (MoSe2), molybdenum ditelluride ($MoTe_2$), tungsten disulfide (WS2), and tungsten diselenide (WSe2) and so on. TMDCs exist in two structural phases: trigonal prismatic (2H) and octahedral (1T) phase, showing more structural stability in the 2H phase. The different stacking order of the three atomic planes resulted in several structural phases; 2H phases with ABA stacking and 1T phases with ABC stacking. Various methods have been reported for the production of 2D TMDCs which involves both top-down and bottom-up approaches. Top- down route involves adhesive tapes [35, 188-190] to exfoliate a bulk crystal by a method known as micromechanical cleavage just like the case in graphene exfoliation. Liquid phase exfoliation is another top-down method for the production of large quantities of 2D TMDCs[191]. The unique feature of this technique is that composites and hybrid materials can be synthesized[192] by combing dispersions from two different exfoliated materials which is not possible with any other technique. The previously developed growth techniques for graphene production such as CVD on metal substrates[193-195] and epitaxial growth on SiC[196]can also be employed for the production of 2D TMDCs. Single crystals of MoS_2[197] and $MoSe_2$ can also be prepared by a hydrothermal method in an autoclave at high temperature and pressure[198]. MoX_2 and WX_2 compounds are generally semiconducting, but $NbX_2$and TaX_2 [199-204]are metallic. The carrier mobility for the monolayer TMDC sheets varies from 100–1000 $cm^2\ V^{-1}\ s^{-1}$[205], according to the carrier mobility chart. The majority of 2D TMDCs have a direct band gap when exfoliated into monolayers, whereas the band gap is indirect in the bulk phase; GaSe and ReS_2 are exceptions from this behaviour[206, 207]. The band gap covers the full visible and infrared range[208, 209] with tunablility up to ≈ 2 eV[210].

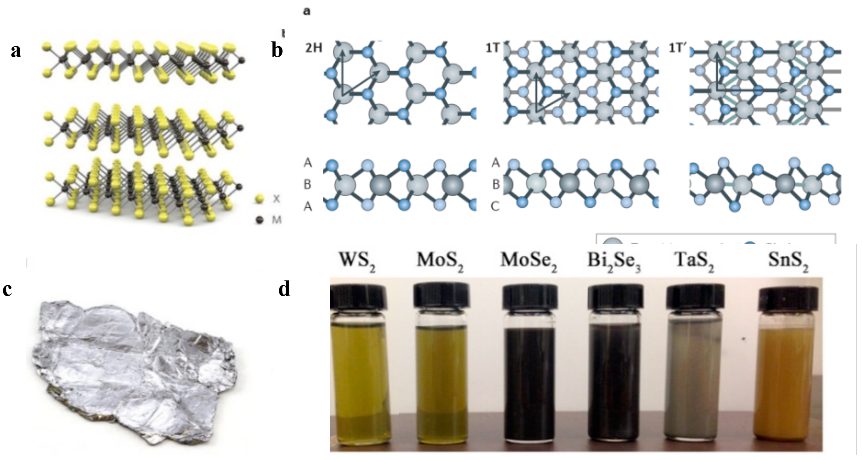

Figure 1.5 Family of 2D TMDCs crystals. ***(a)*** *Three dimensional structural representation of TMDC crystals with typical formula* MX_2*, chalcogen atoms (X) and metal atoms (M) are represented in yellow and in grey colours. Reproduced from ref*[187]*.Copyright 2012, Springer Nature.* ***(b)*** *Atomic structure of single layers of transition metal dichalcogenides (TMDCs) in their trigonal prismatic (2H), distorted octahedral (1T) and dimerized (1T′) phases and corresponding stacking of atomic planes. Reproduced from ref*[186]*.Copyright 2017, Springer Nature.* ***(c)*** *Photograph of a bulk MoS2 crystal.* ***(d)*** *Suspensions of layered materials from liquid-phase exfoliation in solvents. Adapted from ref*[211]*.Copyright 2015, American Chemical Society.*

TMDCs also show excellent mechanical properties, similar to graphene, with a Young's modulus (E) and stiffness of~0.33 TPa and 180 N m^{-1} for single layer MoS_2 sheets[212, 213], respectively. The metallic 1T phase of chemically exfoliated MoS_2 is 10^7moreconductive than the semiconducting 2H phase[214]. Two dimensional TMDCS are considered as promising materials for many applications. The large surface area of the TMDCs enables them to be applied in energy storage devices such as supercapacitors and Li-ion batteries. Among the TMDCs family, MoS_2 is the most studied material due to its high mechanical strength, promise for exfoliation down to monolayer thickness, colossal spin–orbit coupling, which opened up new possible applications in diverse fields from electronic/optoelectronics to energy harvesting and from DNA sequencing to molecular medicine[186, 187, 215-219]. MoS_2 is widely used as an electrode material in supercapacitors owing to its large electrical double layer capacitance (EDLC)[220-223]. Chemical and bio sensing is also another major area where MoS_2 sheets are employed and several reports have been published describing its chemical and bio-sensing behaviour[224-228]. MoS2 nanopores can be used for DNA base detection[229, 230] and osmotic power generation[231]. Besides the usage of MoS_2nanosheets for electronics and energy harvesting applications, new discoveries reveal that MoS_2nanopores or assembled MoS_2 membrane are promising candidate for water desalination and separation applications[232-234].

1.6 References

1. Butler, S. Z.; Hollen, S. M.; Cao, L.; Cui, Y.; Gupta, J. A.; Gutiérrez, H. R.; Heinz, T. F.; Hong, S. S.; Huang, J.; Ismach, A. F.; Johnston-Halperin, E.; Kuno, M.; Plashnitsa, V. V.; Robinson, R. D.; Ruoff, R. S.; Salahuddin, S.; Shan, J.; Shi, L.; Spencer, M. G.; Terrones, M.; Windl, W.; Goldberger, J. E. *ACS Nano* **2013,** 7, (4), 2898-2926.

2. Aufray, B.; Kara, A.; Vizzini, S.; Oughaddou, H.; Léandri, C.; Ealet, B.; Le Lay, G. *Appl. Phys. Lett.* **2010,** 96, (18), 183102.

3. Lalmi, B.; Oughaddou, H.; Enriquez, H.; Kara, A.; Vizzini, S.; Ealet, B.; Aufray, B. *Appl. Phys. Lett.* **2010,** 97, (22), 223109.

4. Kara, A.; Enriquez, H.; Seitsonen, A. P.; Voon, L.; Vizzini, S.; Aufray, B.; Oughaddou, H. *Surf. Sci. Rep.* **2012,** 67, (1), 1-18.

5. Bianco, E.; Butler, S.; Jiang, S.; Restrepo, O. D.; Windl, W.; Goldberger, J. E. *ACS Nano* **2013,** 7, (5), 4414-4421.

6. Pulci, O.; Gori, P.; Marsili, M.; Garbuio, V.; Del Sole, R.; Bechstedt, F. *EPL (Europhysics Letters)* **2012,** 98, (3), 37004.

7. Frindt, R. F. *J. Appl. Phys.* **1966,** 37, (4), 1928-1929.

8. *Proceedings of the Royal Society of London. Series A. Mathematical and Physical Sciences* **1963,** 273, (1352), 69.

9. Joensen, P.; Frindt, R. F.; Morrison, S. R. *Mater. Res. Bull.* **1986,** 21, (4), 457-461.

10. Yang, D.; Frindt, R. F. *J. Phys. Chem. Solids* **1996,** 57, (6), 1113-1116.

11. Geim, A. K.; Grigorieva, I. V. *Nature* **2013,** 499, 419.

12. Mas-Balleste, R.; Gomez-Navarro, C.; Gomez-Herrero, J.; Zamora, F. *Nanoscale* **2011,** 3, (1), 20-30.

13. Osada, M.; Sasaki, T. *Adv. Mater.* **2012,** 24, (2), 210-228.

14. Wang, Q. H.; Kalantar-Zadeh, K.; Kis, A.; Coleman, J. N.; Strano, M. S. *Nat. Nanotechnol.* **2012,** 7, (11), 699.

15. Xu, M.; Liang, T.; Shi, M.; Chen, H. *Chem. Rev.* **2013,** 113, (5), 3766-3798.

16. Butler, S. Z.; Hollen, S. M.; Cao, L.; Cui, Y.; Gupta, J. A.; Gutiérrez, H. R.; Heinz, T. F.; Hong, S. S.; Huang, J.; Ismach, A. F. *ACS Nano* **2013,** 7, (4), 2898-2926.

17. Enoki, T.; Suzuki, M.; Endo, M., *Graphite intercalation compounds and applications*. Oxford University Press: 2003.

18. Dresselhaus, M. S.; Dresselhaus, G. *Advances in physics* **2002,** 51, (1), 1-186.

19. Draine, B. *The Astrophysical Journal Supplement Series* **1985,** 57, 587-594.

20. Charlier, J.-C.; Gonze, X.; Michenaud, J.-P. *Phys. Rev. B* **1991,** 43, (6), 4579.

21. Mounet, N.; Marzari, N. *Phys. Rev. B* **2005,** 71, (20), 205214.

22. Robertson, J. *Surf. Coat. Technol.* **1992,** 50, (3), 185-203.

23. Zaitsev, A. M., *Optical properties of diamond: a data handbook*. Springer Science & Business Media: 2013.

24. Forró, L.; Mihály, L. *Reports on Progress in Physics* **2001,** 64, (5), 649.

25. Wang, Y.; Cheng, L. T. *The Journal of Physical Chemistry* **1992,** 96, (4), 1530-1532.

26. Foote, C. S., Photophysical and photochemical properties of fullerenes. In *Electron Transfer I*, Springer: 1994; pp 347-363.

27. Weaver, J.; Poirier, D., Solid state properties of fullerenes and fullerene-based materials. In *Solid State Physics*, Elsevier: 1994; Vol. 48, pp 1-108.

28. Saito, R.; Dresselhaus, G.; Dresselhaus, M. S., *Physical properties of carbon nanotubes*. World Scientific: 1998.

29. Coleman, J. N.; Khan, U.; Blau, W. J.; Gun'ko, Y. K. *Carbon* **2006,** 44, (9), 1624-1652.

30. Collins, P. G.; Bradley, K.; Ishigami, M.; Zettl, d. A. *Science* **2000,** 287, (5459), 1801-1804.

31. Wallace, P. R. *Physical Review* **1947,** 71, (9), 622-634.

32. McClure, J. *Physical Review* **1956,** 104, (3), 666.

33. Novoselov, K. S.; Geim, A. K.; Morozov, S. V.; Jiang, D.; Zhang, Y.; Dubonos, S. V.; Grigorieva, I. V.; Firsov, A. A. *Science* **2004,** 306, (5696), 666.

34. Geim, A. K.; Kim, P. *Sci. Am.* **2008,** 298, (4), 90-97.

35. Novoselov, K. S.; Jiang, D.; Schedin, F.; Booth, T. J.; Khotkevich, V. V.; Morozov, S. V.; Geim, A. K. *Proc. Natl. Acad. Sci. U. S. A.* **2005,** 102, (30), 10451.

36. Soldano, C.; Mahmood, A.; Dujardin, E. *Carbon* **2010,** 48, (8), 2127-2150.

37. Biro, L. P.; Nemes-Incze, P.; Lambin, P. *Nanoscale* **2012,** 4, (6), 1824-1839.

38. Hattab, H.; N'Diaye, A. T.; Wall, D.; Klein, C.; Jnawali, G.; Coraux, J.; Busse, C.; van Gastel, R.; Poelsema, B.; Michely, T.; Meyer zu Heringdorf, F.-J.; Horn-von Hoegen, M. *Nano Lett.* **2012,** 12, (2), 678-682.

39. Zakharchenko, K. V.; Katsnelson, M. I.; Fasolino, A. *Phys. Rev. Lett.* **2009,** 102, (4), 046808.

40. Geim, A. K.; Novoselov, K. S. *Nat. Mater.* **2007,** 6, 183.

41. Suvarnaphaet, P.; Pechprasarn, S. *Sensors* **2017,** 17, (10).

42. Castro Neto, A. H.; Guinea, F.; Peres, N. M. R.; Novoselov, K. S.; Geim, A. K. *Reviews of Modern Physics* **2009,** 81, (1), 109-162.

43. Mayorov, A. S.; Gorbachev, R. V.; Morozov, S. V.; Britnell, L.; Jalil, R.; Ponomarenko, L. A.; Blake, P.; Novoselov, K. S.; Watanabe, K.; Taniguchi, T.; Geim, A. K. *Nano Lett.* **2011,** 11, (6), 2396-2399.

44. Taychatanapat, T.; Watanabe, K.; Taniguchi, T.; Jarillo-Herrero, P. *Nat. Phys.* **2013,** 9, 225.

45. Novoselov, K. S.; Geim, A. K.; Morozov, S. V.; Jiang, D.; Katsnelson, M. I.; Grigorieva, I. V.; Dubonos, S. V.; Firsov, A. A. *Nature* **2005,** 438, 197.

46. Mayorov, A. S.; Elias, D. C.; Mukhin, I. S.; Morozov, S. V.; Ponomarenko, L. A.; Novoselov, K. S.; Geim, A. K.; Gorbachev, R. V. *Nano Lett.* **2012,** 12, (9), 4629-4634.

47. Bao, W.; Velasco, J.; Zhang, F.; Jing, L.; Standley, B.; Smirnov, D.; Bockrath, M.; MacDonald, A. H.; Lau, C. N. *Proceedings of the National Academy of Sciences USA* **2012,** 109, (27), 10802.

48. Du, X.; Skachko, I.; Barker, A.; Andrei, E. Y. *Nat. Nanotechnol.* **2008,** 3, 491.

49. Nair, R. R.; Blake, P.; Grigorenko, A. N.; Novoselov, K. S.; Booth, T. J.; Stauber, T.; Peres, N. M. R.; Geim, A. K. *Science* **2008,** 320, (5881), 1308.

50. Kim, K. S.; Zhao, Y.; Jang, H.; Lee, S. Y.; Kim, J. M.; Kim, K. S.; Ahn, J.-H.; Kim, P.; Choi, J.-Y.; Hong, B. H. *Nature* **2009,** 457, 706.

51. Blake, P.; Brimicombe, P. D.; Nair, R. R.; Booth, T. J.; Jiang, D.; Schedin, F.; Ponomarenko, L. A.; Morozov, S. V.; Gleeson, H. F.; Hill, E. W.; Geim, A. K.; Novoselov, K. S. *Nano Lett.* **2008,** 8, (6), 1704-1708.

52. Wang, X.; Zhi, L.; Müllen, K. *Nano Lett.* **2008,** 8, (1), 323-327.

53. Hernandez, Y.; Nicolosi, V.; Lotya, M.; Blighe, F. M.; Sun, Z.; De, S.; McGovern, I. T.; Holland, B.; Byrne, M.; Gun'Ko, Y. K.; Boland, J. J.; Niraj, P.; Duesberg, G.; Krishnamurthy, S.; Goodhue, R.; Hutchison, J.; Scardaci, V.; Ferrari, A. C.; Coleman, J. N. *Nat. Nanotechnol.* **2008,** 3, 563.

54. Lee, C.; Wei, X.; Kysar, J. W.; Hone, J. *Science* **2008,** 321, (5887), 385.

55. Bunch, J. S.; van der Zande, A. M.; Verbridge, S. S.; Frank, I. W.; Tanenbaum, D. M.; Parpia, J. M.; Craighead, H. G.; McEuen, P. L. *Science* **2007,** 315, (5811), 490.

56. Frank, I. W.; Tanenbaum, D. M.; van der Zande, A. M.; McEuen, P. L. *Journal of Vacuum Science & Technology B: Microelectronics and Nanometer Structures Processing, Measurement, and Phenomena* **2007,** 25, (6), 2558-2561.

57. Balandin, A. A. *Nat. Mater.* **2011,** 10, 569.

58. Balandin, A. A.; Ghosh, S.; Bao, W.; Calizo, I.; Teweldebrhan, D.; Miao, F.; Lau, C. N. *Nano Lett.* **2008,** 8, (3), 902-907.

59. Pop, E.; Mann, D.; Wang, Q.; Goodson, K.; Dai, H. *Nano Lett.* **2006,** 6, (1), 96-100.

60. Blake, P.; Hill, E.; Castro Neto, A.; Novoselov, K.; Jiang, D.; Yang, R.; Booth, T.; Geim, A. *Appl. Phys. Lett.* **2007,** 91, (6), 063124.

61. Gao, L.; Ren, W.; Li, F.; Cheng, H.-M. *ACS Nano* **2008,** 2, (8), 1625-1633.

62. Jung, I.; Pelton, M.; Piner, R.; Dikin, D. A.; Stankovich, S.; Watcharotone, S.; Hausner, M.; Ruoff, R. S. *Nano Lett.* **2007,** 7, (12), 3569-3575.

63. Land, T. A.; Michely, T.; Behm, R. J.; Hemminger, J. C.; Comsa, G. *Surf. Sci.* **1992,** 264, (3), 261-270.

64. Kim, K. S.; Zhao, Y.; Jang, H.; Lee, S. Y.; Kim, J. M.; Kim, K. S.; Ahn, J.-H.; Kim, P.; Choi, J.-Y.; Hong, B. H. *nature* **2009,** 457, (7230), 706.

65. Yang, W.; Chen, G.; Shi, Z.; Liu, C.-C.; Zhang, L.; Xie, G.; Cheng, M.; Wang, D.; Yang, R.; Shi, D. *Nat. Mater.* **2013,** 12, (9), 792.

66. Emtsev, K. V.; Bostwick, A.; Horn, K.; Jobst, J.; Kellogg, G. L.; Ley, L.; McChesney, J. L.; Ohta, T.; Reshanov, S. A.; Röhrl, J. *Nat. Mater.* **2009,** 8, (3), 203.

67. Wu, Y.; Ye, P.; Capano, M. A.; Xuan, Y.; Sui, Y.; Qi, M.; Cooper, J. A.; Shen, T.; Pandey, D.; Prakash, G. *Appl. Phys. Lett.* **2008,** 92, (9), 092102.

68. Choucair, M.; Thordarson, P.; Stride, J. A. *Nat. Nanotechnol.* **2009,** 4, (1), 30.

69. Reina, A.; Jia, X.; Ho, J.; Nezich, D.; Son, H.; Bulovic, V.; Dresselhaus, M. S.; Kong, J. *Nano Lett.* **2009,** 9, (1), 30-35.

70. Zhou, S. Y.; Gweon, G. H.; Fedorov, A. V.; First, P. N.; de Heer, W. A.; Lee, D. H.; Guinea, F.; Castro Neto, A. H.; Lanzara, A. *Nat. Mater.* **2007,** 6, 770.

71. Novoselov, K. *Nat. Mater.* **2007,** 6, 720.

72. Karim, N.; Afroj, S.; Tan, S.; He, P.; Fernando, A.; Carr, C.; Novoselov, K. S. *ACS Nano* **2017,** 11, (12), 12266-12275.

73. Kang, M.; Kim, J.; Jang, B.; Chae, Y.; Kim, J.-H.; Ahn, J.-H. *ACS Nano* **2017,** 11, (8), 7950-7957.

74. Schedin, F.; Geim, A. K.; Morozov, S. V.; Hill, E. W.; Blake, P.; Katsnelson, M. I.; Novoselov, K. S. *Nat. Mater.* **2007,** 6, 652.

75. Dan, Y.; Lu, Y.; Kybert, N. J.; Luo, Z.; Johnson, A. T. C. *Nano Lett.* **2009,** 9, (4), 1472-1475.

76. Robinson, J. T.; Perkins, F. K.; Snow, E. S.; Wei, Z.; Sheehan, P. E. *Nano Lett.* **2008,** 8, (10), 3137-3140.

77. Tang, L.; Wang, Y.; Li, Y.; Feng, H.; Lu, J.; Li, J. *Adv. Funct. Mater.* **2009,** 19, (17), 2782-2789.

78. Mohanty, N.; Berry, V. *Nano Lett.* **2008,** 8, (12), 4469-4476.

79. Ohno, Y.; Maehashi, K.; Yamashiro, Y.; Matsumoto, K. *Nano Lett.* **2009,** 9, (9), 3318-3322.

80. Li, X.; Zhu, Y.; Cai, W.; Borysiak, M.; Han, B.; Chen, D.; Piner, R. D.; Colombo, L.; Ruoff, R. S. *Nano Lett.* **2009,** 9, (12), 4359-4363.

81. Cote, L. J.; Kim, F.; Huang, J. *J. Am. Chem. Soc.* **2009,** 131, (3), 1043-1049.

82. Zhu, Y.; Murali, S.; Cai, W.; Li, X.; Suk, J. W.; Potts, J. R.; Ruoff, R. S. *Advanced Materials* **2010,** 22, (35), 3906-3924.

83. Liang, M.; Zhi, L. *J. Mater. Chem.* **2009,** 19, (33), 5871-5878.

84. Stoller, M. D.; Park, S.; Zhu, Y.; An, J.; Ruoff, R. S. *Nano Lett.* **2008,** 8, (10), 3498-3502.

85. Li, N.; Chen, Z.; Ren, W.; Li, F.; Cheng, H.-M. *Proceedings of the National Academy of Sciences* **2012,** 109, (43), 17360-17365.

86. El-Kady, M. F.; Strong, V.; Dubin, S.; Kaner, R. B. *Science* **2012,** 335, (6074), 1326-1330.

87. Zhang, L. L.; Zhou, R.; Zhao, X. *J. Mater. Chem.* **2010,** 20, (29), 5983-5992.

88. Huang, X.; Qi, X.; Boey, F.; Zhang, H. *Chem. Soc. Rev.* **2012,** 41, (2), 666-686.

89. Stankovich, S.; Dikin, D. A.; Dommett, G. H.; Kohlhaas, K. M.; Zimney, E. J.; Stach, E. A.; Piner, R. D.; Nguyen, S. T.; Ruoff, R. S. *Nature* **2006,** 442, (7100), 282.

90. Kuilla, T.; Bhadra, S.; Yao, D.; Kim, N. H.; Bose, S.; Lee, J. H. *Prog. Polym. Sci.* **2010,** 35, (11), 1350-1375.

91. Bai, X.; Zhai, Y.; Zhang, Y. *J. Phys. Chem. C* **2011,** 115, (23), 11673-11677.

92. Szabó, T.; Berkesi, O.; Forgó, P.; Josepovits, K.; Sanakis, Y.; Petridis, D.; Dékány, I. *Chem. Mater.* **2006,** 18, (11), 2740-2749.

93. Hontoria-Lucas, C.; López-Peinado, A. J.; López-González, J. d. D.; Rojas-Cervantes, M. L.; Martín-Aranda, R. M. *Carbon* **1995,** 33, (11), 1585-1592.

94. Loh, K. P.; Bao, Q.; Eda, G.; Chhowalla, M. *Nat. Chem.* **2010,** 2, 1015.

95. Abraham, J.; Vasu, K. S.; Williams, C. D.; Gopinadhan, K.; Su, Y.; Cherian, C. T.; Dix, J.; Prestat, E.; Haigh, S. J.; Grigorieva, I. V.; Carbone, P.; Geim, A. K.; Nair, R. R. *Nature Nanotechnology* **2017,** 12, 546.

96. Chung, C.; Kim, Y.-K.; Shin, D.; Ryoo, S.-R.; Hong, B. H.; Min, D.-H. *Acc. Chem. Res.* **2013,** 46, (10), 2211-2224.

97. Peng, E.; Choo, E. S. G.; Chandrasekharan, P.; Yang, C.-T.; Ding, J.; Chuang, K.-H.; Xue, J. M. *Small* **2012,** 8, (23), 3620-3630.

98. Yang, Y.; Asiri, A. M.; Tang, Z.; Du, D.; Lin, Y. *Mater. Today* **2013,** 16, (10), 365-373.

99. Li, F.; Jiang, X.; Zhao, J.; Zhang, S. *Nano Energy* **2015,** 16, 488-515.

100. Eda, G.; Chhowalla, M. *Advanced Materials* **2010,** 22, (22), 2392-2415.

101. Mattevi, C.; Eda, G.; Agnoli, S.; Miller, S.; Mkhoyan, K. A.; Celik, O.; Mastrogiovanni, D.; Granozzi, G.; Garfunkel, E.; Chhowalla, M. *Adv. Funct. Mater.* **2009,** 19, (16), 2577-2583.

102. Jung, I.; Dikin, D. A.; Piner, R. D.; Ruoff, R. S. *Nano Lett.* **2008,** 8, (12), 4283-4287.

103. Geim, A. K. *Science* **2009,** 324, (5934), 1530.

104. Boukhvalov, D. W.; Katsnelson, M. I. *J. Am. Chem. Soc.* **2008,** 130, (32), 10697-10701.

105. Mkhoyan, K. A.; Contryman, A. W.; Silcox, J.; Stewart, D. A.; Eda, G.; Mattevi, C.; Miller, S.; Chhowalla, M. *Nano Lett.* **2009,** 9, (3), 1058-1063.

106. Eda, G.; Mattevi, C.; Yamaguchi, H.; Kim, H.; Chhowalla, M. *J. Phys. Chem. C* **2009,** 113, (35), 15768-15771.

107. Gómez-Navarro, C.; Weitz, R. T.; Bittner, A. M.; Scolari, M.; Mews, A.; Burghard, M.; Kern, K. *Nano Lett.* **2007,** 7, (11), 3499-3503.

108. Gilje, S.; Han, S.; Wang, M.; Wang, K. L.; Kaner, R. B. *Nano Lett.* **2007,** 7, (11), 3394-3398.

109. Dikin, D. A.; Stankovich, S.; Zimney, E. J.; Piner, R. D.; Dommett, G. H. B.; Evmenenko, G.; Nguyen, S. T.; Ruoff, R. S. *Nature* **2007,** 448, 457.

110. Buchsteiner, A.; Lerf, A.; Pieper, J. *The Journal of Physical Chemistry B* **2006,** 110, (45), 22328-22338.

111. Rezania, B.; Severin, N.; Talyzin, A. V.; Rabe, J. P. *Nano Lett.* **2014,** 14, (7), 3993-3998.

112. Su, C.-Y.; Xu, Y.; Zhang, W.; Zhao, J.; Tang, X.; Tsai, C.-H.; Li, L.-J. *Chem. Mater.* **2009,** 21, (23), 5674-5680.

113. Zhang, L.; Liang, J.; Huang, Y.; Ma, Y.; Wang, Y.; Chen, Y. *Carbon* **2009,** 14, (47), 3365-3368.

114. Pan, S.; Aksay, I. A. *ACS Nano* **2011,** 5, (5), 4073-4083.

115. Brodie, B. C. *Philosophical Transactions of the Royal Society of London* **1859,** 149, 249-259.

116. Staudenmaier, L. *Eur. J. Inorg. Chem.* **1898,** 31, (2), 1481-1487.

117. Hofmann, U.; König, E. *Z. Anorg. Allg. Chem.* **1937,** 234, (4), 311-336.

118. Hummers, W. S.; Offeman, R. E. *J. Am. Chem. Soc.* **1958,** 80, (6), 1339-1339.

119. Marcano, D. C.; Kosynkin, D. V.; Berlin, J. M.; Sinitskii, A.; Sun, Z.; Slesarev, A.; Alemany, L. B.; Lu, W.; Tour, J. M. *ACS Nano* **2010,** 4, (8), 4806-4814.

120. Dreyer, D. R.; Todd, A. D.; Bielawski, C. W. *Chemical Society Reviews* **2014,** 43, (15), 5288-5301.

121. Dreyer, D. R.; Park, S.; Bielawski, C. W.; Ruoff, R. S. *Chemical Society Reviews* **2010,** 39, (1), 228-240.

122. He, H.; Klinowski, J.; Forster, M.; Lerf, A. *Chem. Phys. Lett.* **1998,** 287, (1), 53-56.

123. Yang, T.; Lin, H.; Zheng, X.; Loh, K. P.; Jia, B. *Journal of Materials Chemistry A* **2017,** 5, (32), 16537-16558.

124. Wang, S.; Ang, P. K.; Wang, Z.; Tang, A. L. L.; Thong, J. T. L.; Loh, K. P. *Nano Lett.* **2010,** 10, (1), 92-98.

125. Su, C.-Y.; Xu, Y.; Zhang, W.; Zhao, J.; Liu, A.; Tang, X.; Tsai, C.-H.; Huang, Y.; Li, L.-J. *ACS Nano* **2010,** 4, (9), 5285-5292.

126. Wang, S.; Chia, P.-J.; Chua, L.-L.; Zhao, L.-H.; Png, R.-Q.; Sivaramakrishnan, S.; Zhou, M.; Goh, R. G. S.; Friend, R. H.; Wee, A. T. S.; Ho, P. K. H. *Adv. Mater.* **2008,** 20, (18), 3440-3446.

127. Borini, S.; White, R.; Wei, D.; Astley, M.; Haque, S.; Spigone, E.; Harris, N.; Kivioja, J.; Ryhänen, T. *ACS Nano* **2013,** 7, (12), 11166-11173.

128. Bi, H.; Yin, K.; Xie, X.; Ji, J.; Wan, S.; Sun, L.; Terrones, M.; Dresselhaus, M. S. *Scientific Reports* **2013,** 3, 2714.

129. Huang, X.; Leng, T.; Georgiou, T.; Abraham, J.; Raveendran Nair, R.; Novoselov, K. S.; Hu, Z. *Scientific Reports* **2018,** 8, (1), 43.

130. Prezioso, S.; Perrozzi, F.; Giancaterini, L.; Cantalini, C.; Treossi, E.; Palermo, V.; Nardone, M.; Santucci, S.; Ottaviano, L. *J. Phys. Chem. C* **2013,** 117, (20), 10683-10690.

131. Pustelny, T.; Drewniak, S.; Setkiewicz, M.; Maciak, E.; Urbańczyk, M.; Procek, M.; Gut, K.; Opilski, Z.; Jagiello, J.; Lipinska, L., The sensitivity of sensor structures with oxide graphene exposed to selected gaseous atmospheres. In *Bulletin of the Polish Academy of Sciences: Technical Sciences*, 2013; Vol. 61, p 705.

132. Jia, H.-P.; Dreyer, D. R.; Bielawski, C. W. *Adv. Synth. Catal.* **2011,** 353, (4), 528-532.

133. Boukhvalov, D. W.; Dreyer, D. R.; Bielawski, C. W.; Son, Y.-W. *ChemCatChem* **2012,** 4, (11), 1844-1849.

134. Kim, Y.; Some, S.; Lee, H. *Chem. Commun.* **2013,** 49, (50), 5702-5704.

135. Cao, Y.; Lai, Z.; Feng, J.; Wu, P. *J. Mater. Chem.* **2011,** 21, (25), 9271-9278.

136. Lu, C.-H.; Yang, H.-H.; Zhu, C.-L.; Chen, X.; Chen, G.-N. *Angewandte Chemie International Edition* **2009,** 48, (26), 4785-4787.

137. Huang, Y.; Dong, X.; Liu, Y.; Li, L.-J.; Chen, P. *J. Mater. Chem.* **2011,** 21, (33), 12358-12362.

138. Liu, Z.; Robinson, J. T.; Sun, X.; Dai, H. *J. Am. Chem. Soc.* **2008,** 130, (33), 10876-10877.

139. Liu, J.; Cui, L.; Losic, D. *Acta Biomater.* **2013,** 9, (12), 9243-9257.

140. Weaver, C. L.; LaRosa, J. M.; Luo, X.; Cui, X. T. *ACS Nano* **2014,** 8, (2), 1834-1843.

141. Sun, X.; Liu, Z.; Welsher, K.; Robinson, J. T.; Goodwin, A.; Zaric, S.; Dai, H. *Nano research* **2008,** 1, (3), 203-212.

142. Akhavan, O.; Ghaderi, E. *ACS Nano* **2010,** 4, (10), 5731-5736.

143. Santos, C. M.; Tria, M. C. R.; Vergara, R. A. M. V.; Ahmed, F.; Advincula, R. C.; Rodrigues, D. F. *Chem. Commun.* **2011,** 47, (31), 8892-8894.

144. Joshi, R. K.; Carbone, P.; Wang, F. C.; Kravets, V. G.; Su, Y.; Grigorieva, I. V.; Wu, H. A.; Geim, A. K.; Nair, R. R. *Science* **2014,** 343, (6172), 752-754.

145. Nair, R. R.; Wu, H. A.; Jayaram, P. N.; Grigorieva, I. V.; Geim, A. K. *Science* **2012,** 335, (6067), 442.

146. Hu, M.; Mi, B. *Environmental Science & Technology* **2013,** 47, (8), 3715-3723.

147. Pakdel, A.; Bando, Y.; Golberg, D. *Chem. Soc. Rev.* **2014,** 43, (3), 934-959.

148. Balmain, W. H. *The London, Edinburgh, and Dublin Philosophical Magazine and Journal of Science* **1842,** 21, (138), 270-277.

149. Bernard, S.; Miele, P. *Mater. Today* **2014,** 17, (9), 443-450.

150. Golberg, D.; Bando, Y.; Stéphan, O.; Kurashima, K. *Appl. Phys. Lett.* **1998,** 73, (17), 2441-2443.

151. Paine, R. T.; Narula, C. K. *Chem. Rev.* **1990,** 90, (1), 73-91.

152. Sachdev, H.; Müller, F.; Hüfner, S. *Diamond Relat. Mater.* **2010,** 19, (7-9), 1027-1033.

153. Schmolla, W.; Hartnagel, H. *Solid-State Electron.* **1983,** 26, (10), 931-939.

154. Hamilton, E. J.; Dolan, S. E.; Mann, C. M.; Colijn, H. O.; McDonald, C. A.; Shore, S. G. *Science* **1993,** 260, (5108), 659-661.

155. Zhi, C.; Bando, Y.; Tang, C.; Golberg, D. *Materials Science and Engineering: R: Reports* **2010,** 70, (3-6), 92-111.

156. Corso, M.; Auwärter, W.; Muntwiler, M.; Tamai, A.; Greber, T.; Osterwalder, J. *Science* **2004,** 303, (5655), 217.

157. Gannett, W.; Regan, W.; Watanabe, K.; Taniguchi, T.; Crommie, M.; Zettl, A. *Appl. Phys. Lett.* **2011,** 98, (24), 242105.

158. Zhou, H.; Zhu, J.; Liu, Z.; Yan, Z.; Fan, X.; Lin, J.; Wang, G.; Yan, Q.; Yu, T.; Ajayan, P. M. *Nano Research* **2014,** 7, (8), 1232-1240.

159. Kumar, R.; Rajasekaran, G.; Parashar, A. *Nanotechnology* **2016,** 27, (8), 085706.

160. Wang, J.; Ma, F.; Sun, M. *RSC Advances* **2017,** 7, (27), 16801-16822.

161. Dean, C. R.; Young, A. F.; Meric, I.; Lee, C.; Wang, L.; Sorgenfrei, S.; Watanabe, K.; Taniguchi, T.; Kim, P.; Shepard, K. L. *Nat. Nanotechnol.* **2010,** 5, (10), 722.

162. Pacilé, D.; Meyer, J. C.; Girit, Ç. Ö.; Zettl, A. *Appl. Phys. Lett.* **2008,** 92, (13), 133107.

163. Li, L. H.; Chen, Y.; Behan, G.; Zhang, H.; Petravic, M.; Glushenkov, A. M. *J. Mater. Chem.* **2011,** 21, (32), 11862-11866.

164. Han, W.-Q.; Wu, L.; Zhu, Y.; Watanabe, K.; Taniguchi, T. *Appl. Phys. Lett.* **2008,** 93, (22), 223103.

165. Zhi, C.; Bando, Y.; Tang, C.; Kuwahara, H.; Golberg, D. *Adv. Mater.* **2009,** 21, (28), 2889-2893.

166. Wang, Y.; Shi, Z.; Yin, J. *J. Mater. Chem.* **2011,** 21, (30), 11371-11377.

167. Cao, L.; Emami, S.; Lafdi, K. *Materials Express* **2014,** 4, (2), 165-171.

168. Shen, J.; He, Y.; Wu, J.; Gao, C.; Keyshar, K.; Zhang, X.; Yang, Y.; Ye, M.; Vajtai, R.; Lou, J. *Nano letters* **2015,** 15, (8), 5449-5454.

169. Paffett, M.; Simonson, R.; Papin, P.; Paine, R. *Surf. Sci.* **1990,** 232, (3), 286-296.

170. Auwärter, W.; Suter, H. U.; Sachdev, H.; Greber, T. *Chem. Mater.* **2004,** 16, (2), 343-345.

171. Müller, F.; Stöwe, K.; Sachdev, H. *Chem. Mater.* **2005,** 17, (13), 3464-3467.

172. Wang, H.; Zhang, X.; Liu, H.; Yin, Z.; Meng, J.; Xia, J.; Meng, X.-M.; Wu, J.; You, J. *Adv. Mater.* **2015,** 27, (48), 8109-8115.

173. Camilli, L.; Sutter, E.; Sutter, P. *2D Materials* **2014,** 1, (2), 025003.

174. Gehring, P.; Gao, B. F.; Burghard, M.; Kern, K. *Nano Lett.* **2012,** 12, (10), 5137-5142.

175. Velázquez, D.; Seibert, R.; Man, H.; Spentzouris, L.; Terry, J. *J. Appl. Phys.* **2016,** 119, (9), 095306.

176. Wang, M.; Jang, S. K.; Jang, W. J.; Kim, M.; Park, S. Y.; Kim, S. W.; Kahng, S. J.; Choi, J. Y.; Ruoff, R. S.; Song, Y. J. *Adv. Mater.* **2013,** 25, (19), 2746-2752.

177. Song, W.-L.; Wang, P.; Cao, L.; Anderson, A.; Meziani, M. J.; Farr, A. J.; Sun, Y.-P. *Angewandte Chemie International Edition* **2012,** 51, (26), 6498-6501.

178. Yu, J.; Huang, X.; Wu, C.; Wu, X.; Wang, G.; Jiang, P. *Polymer* **2012,** 53, (2), 471-480.

179. Gao, M.; Lyalin, A.; Taketsugu, T. *J. Phys. Chem. C* **2012,** 116, (16), 9054-9062.

180. Wang, L.; Shen, L.; Xu, X.; Xu, L.; Qian, Y. *RSC Advances* **2012,** 2, (28), 10689-10693.

181. Siria, A.; Poncharal, P.; Biance, A.-L.; Fulcrand, R.; Blase, X.; Purcell, S. T.; Bocquet, L. *Nature* **2013,** 494, (7438), 455.

182. Won, C. Y.; Aluru, N. *J. Am. Chem. Soc.* **2007,** 129, (10), 2748-2749.

183. Suk, M.; Raghunathan, A.; Aluru, N. *Appl. Phys. Lett.* **2008,** 92, (13), 133120.

184. Jariwala, D.; Sangwan, V. K.; Lauhon, L. J.; Marks, T. J.; Hersam, M. C. *ACS Nano* **2014,** 8, (2), 1102-1120.

185. Duan, X.; Wang, C.; Pan, A.; Yu, R.; Duan, X. *Chem. Soc. Rev.* **2015,** 44, (24), 8859-8876.

186. Manzeli, S.; Ovchinnikov, D.; Pasquier, D.; Yazyev, O. V.; Kis, A. *Nat Rev Mater* **2017,** 2, 17033.

187. Wang, Q. H.; Kalantar-Zadeh, K.; Kis, A.; Coleman, J. N.; Strano, M. S. *Nature Nanotechnology* **2012,** 7, 699.

188. Alem, N.; Erni, R.; Kisielowski, C.; Rossell, M. D.; Gannett, W.; Zettl, A. *Phys. Rev. B* **2009,** 80, (15), 155425.

189. Lee, C.; Yan, H.; Brus, L. E.; Heinz, T. F.; Hone, J.; Ryu, S. *ACS Nano* **2010,** 4, (5), 2695-2700.

190. Mak, K. F.; Lee, C.; Hone, J.; Shan, J.; Heinz, T. F. *Phys. Rev. Lett.* **2010,** 105, (13), 136805.

191. Tsai, H.-L.; Heising, J.; Schindler, J. L.; Kannewurf, C. R.; Kanatzidis, M. G. *Chem. Mater.* **1997,** 9, (4), 879-882.

192. Coleman, J. N.; Lotya, M.; O'Neill, A.; Bergin, S. D.; King, P. J.; Khan, U.; Young, K.; Gaucher, A.; De, S.; Smith, R. J.; Shvets, I. V.; Arora, S. K.; Stanton, G.;

Kim, H.-Y.; Lee, K.; Kim, G. T.; Duesberg, G. S.; Hallam, T.; Boland, J. J.; Wang, J. J.; Donegan, J. F.; Grunlan, J. C.; Moriarty, G.; Shmeliov, A.; Nicholls, R. J.; Perkins, J. M.; Grieveson, E. M.; Theuwissen, K.; McComb, D. W.; Nellist, P. D.; Nicolosi, V. *Science* **2011,** 331, (6017), 568.

193. Li, X.; Cai, W.; An, J.; Kim, S.; Nah, J.; Yang, D.; Piner, R.; Velamakanni, A.; Jung, I.; Tutuc, E.; Banerjee, S. K.; Colombo, L.; Ruoff, R. S. *Science* **2009,** 324, (5932), 1312.

194. Zhan, Y.; Liu, Z.; Najmaei, S.; Ajayan, P. M.; Lou, J. *Small* **2012,** 8, (7), 966-971.

195. Liu, K.-K.; Zhang, W.; Lee, Y.-H.; Lin, Y.-C.; Chang, M.-T.; Su, C.-Y.; Chang, C.-S.; Li, H.; Shi, Y.; Zhang, H.; Lai, C.-S.; Li, L.-J. *Nano Lett.* **2012,** 12, (3), 1538-1544.

196. Hass, J.; Heer, W. A. d.; Conrad, E. H. *J. Phys.: Condens. Matter* **2008,** 20, (32), 323202.

197. Peng, Y.; Meng, Z.; Zhong, C.; Lu, J.; Yu, W.; Yang, Z.; Qian, Y. *J. Solid State Chem.* **2001,** 159, (1), 170-173.

198. Peng, Y.; Meng, Z.; Zhong, C.; Lu, J.; Yu, W.; Jia, Y.; Qian, Y. *Chem. Lett.* **2001,** 30, (8), 772-773.

199. Kuc, A.; Zibouche, N.; Heine, T. *Physical Review B* **2011,** 83, (24), 245213.

200. Kobayashi, K.; Yamauchi, J. *Phys. Rev. B* **1995,** 51, (23), 17085-17095.

201. Li, T.; Galli, G. *J. Phys. Chem. C* **2007,** 111, (44), 16192-16196.

202. Liu, L.; Kumar, S. B.; Ouyang, Y.; Guo, J. *IEEE Trans. Electron Devices* **2011,** 58, (9), 3042-3047.

203. Ding, Y.; Wang, Y.; Ni, J.; Shi, L.; Shi, S.; Tang, W. *Physica B: Condensed Matter* **2011,** 406, (11), 2254-2260.

204. Ataca, C.; Şahin, H.; Ciraci, S. *J. Phys. Chem. C* **2012,** 116, (16), 8983-8999.

205. Yu, Z.; Ong, Z.-Y.; Li, S.; Xu, J.-B.; Zhang, G.; Zhang, Y.-W.; Shi, Y.; Wang, X. *Adv. Funct. Mater.* **2017,** 27, (19), 1604093-n/a.

206. Pozo-Zamudio, O. D.; Schwarz, S.; Sich, M.; Akimov, I. A.; Bayer, M.; Schofield, R. C.; Chekhovich, E. A.; Robinson, B. J.; Kay, N. D.; Kolosov, O. V.; Dmitriev, A. I.; Lashkarev, G. V.; Borisenko, D. N.; Kolesnikov, N. N.; Tartakovskii, A. I. *2D Materials* **2015,** 2, (3), 035010.

207. Tongay, S.; Sahin, H.; Ko, C.; Luce, A.; Fan, W.; Liu, K.; Zhou, J.; Huang, Y.-S.; Ho, C.-H.; Yan, J.; Ogletree, D. F.; Aloni, S.; Ji, J.; Li, S.; Li, J.; Peeters, F. M.; Wu, J. *Nat. Commun.* **2014,** 5, 3252.

208. Xia, F.; Wang, H.; Xiao, D.; Dubey, M.; Ramasubramaniam, A. *Nat. Photonics* **2014,** 8, 899.

209. Choi, W.; Choudhary, N.; Han, G. H.; Park, J.; Akinwande, D.; Lee, Y. H. *Mater. Today* **2017,** 20, (3), 116-130.

210. Coehoorn, R.; Haas, C.; Dijkstra, J.; Flipse, C. J. F.; de Groot, R. A.; Wold, A. *Physical Review B* **1987,** 35, (12), 6195-6202.

211. Shen, J.; He, Y.; Wu, J.; Gao, C.; Keyshar, K.; Zhang, X.; Yang, Y.; Ye, M.; Vajtai, R.; Lou, J.; Ajayan, P. M. *Nano Lett.* **2015,** 15, (8), 5449-5454.

212. Castellanos-Gomez, A.; Poot, M.; Steele, G. A.; van der Zant, H. S. J.; Agraït, N.; Rubio-Bollinger, G. *Adv. Mater.* **2012,** 24, (6), 772-775.

213. Bertolazzi, S.; Brivio, J.; Kis, A. *ACS Nano* **2011,** 5, (12), 9703-9709.

214. Kappera, R.; Voiry, D.; Yalcin, S. E.; Jen, W.; Acerce, M.; Torrel, S.; Branch, B.; Lei, S.; Chen, W.; Najmaei, S.; Lou, J.; Ajayan, P. M.; Gupta, G.; Mohite, A. D.; Chhowalla, M. *APL Mater.* **2014,** 2, (9), 092516.

215. Lopez-Sanchez, O.; Lembke, D.; Kayci, M.; Radenovic, A.; Kis, A. *Nat. Nanotechnol.* **2013,** 8, 497.

216. Farimani, A. B.; Min, K.; Aluru, N. R. *ACS Nano* **2014,** 8, (8), 7914-7922.

217. Feng, J.; Liu, K.; Bulushev, R. D.; Khlybov, S.; Dumcenco, D.; Kis, A.; Radenovic, A. *Nat. Nanotechnol.* **2015,** 10, 1070.

218. Liu, K.; Feng, J.; Kis, A.; Radenovic, A. *ACS Nano* **2014,** 8, (3), 2504-2511.

219. Li, X.; Zhu, H. *Journal of Materiomics* **2015,** 1, (1), 33-44.

220. Fang, C.; Ellis, A. V.; Voelcker, N. H. *Electrochim. Acta* **2012,** 59, 346-353.

221. Hwang, H.; Kim, H.; Cho, J. *Nano Lett.* **2011,** 11, (11), 4826-4830.

222. Stephenson, T.; Li, Z.; Olsen, B.; Mitlin, D. *Energy Environ. Sci.* **2014,** 7, (1), 209-231.

223. Acerce, M.; Voiry, D.; Chhowalla, M. *Nat. Nanotechnol.* **2015,** 10, 313.

224. Kalantar-zadeh, K.; Ou, J. Z. *ACS Sensors* **2016,** 1, (1), 5-16.

225. Donarelli, M.; Prezioso, S.; Perrozzi, F.; Bisti, F.; Nardone, M.; Giancaterini, L.; Cantalini, C.; Ottaviano, L. *Sensors and Actuators B: Chemical* **2015,** 207, 602-613.

226. Kou, L.; Frauenheim, T.; Chen, C. *J. Phys. Chem. Lett.* **2014,** 5, (15), 2675-2681.

227. Perkins, F. K.; Friedman, A. L.; Cobas, E.; Campbell, P. M.; Jernigan, G. G.; Jonker, B. T. *Nano Lett.* **2013,** 13, (2), 668-673.

228. Trepagnier, E. H.; Radenovic, A.; Sivak, D.; Geissler, P.; Liphardt, J. *Nano Lett.* **2007,** 7, (9), 2824-2830.

229. Loan, P. T. K.; Zhang, W.; Lin, C. T.; Wei, K. H.; Li, L. J.; Chen, C. H. *Adv. Mater.* **2014,** 26, (28), 4838-4844.

230. Yuan, Y.; Li, R.; Liu, Z. *Anal. Chem.* **2014,** 86, (7), 3610-3615.

231. Feng, J.; Graf, M.; Liu, K.; Ovchinnikov, D.; Dumcenco, D.; Heiranian, M.; Nandigana, V.; Aluru, N. R.; Kis, A.; Radenovic, A. *Nature* **2016,** 536, 197.

232. Heiranian, M.; Farimani, A. B.; Aluru, N. R. *Nat. Commun.* **2015,** 6, 8616.

233. Hirunpinyopas, W.; Prestat, E.; Worrall, S. D.; Haigh, S. J.; Dryfe, R. A. W.; Bissett, M. A. *ACS Nano* **2017,** 11, (11), 11082-11090.

234. Li, W.; Yang, Y.; Weber, J. K.; Zhang, G.; Zhou, R. *ACS Nano* **2016,** 10, (2), 1829-1835.

Blank Page

Chapter 2- Introduction to Graphene-based Membranes

Blank Page

2.1 Graphene-based membranes: an overlook

Ever since the isolation of graphene in 2004, the interest on 2D materials leaped suddenly with frequent additions to the 2D material library. The large aspect ratio of 2D materials makes the mutual interaction between 2D layers stronger, facilitating the formation of membranes by self-assembly of 2D sheets. The idea of molecular self-assembly has offered a new research direction to explore, providing an excellent platform for developing 2D membranes with unique functionalities. A membrane is a selective barrier allowing some species to pass through while blocking others. Species to be separated may be ions, molecules, micro pollutants and other natural organic matters. The atomically thin nature and the frictionless carbon surface enables graphene sheet to form membranes; the large aspect ratio, mechanical and chemical stability of the exfoliated 2D graphene sheets further facilitates the development of other graphene based membranes e.g. GO and graphene-based composites. Once the provision for van der Waal assembly of 2D sheets and atomic smoothness of graphene sheet are fully utilized, it is even feasible to create synthetic graphene based artificial channels with a height of several angstroms and above. Furthermore, angstrom sized pores can be introduced into the graphene lattice by ion bombardment and etching processes which would transform impermeable graphene sheet into a permeable one to be used in water desalination and separation applications. The exceptional molecular sieving properties and promising water permeability demonstrated by graphene based membranes is due to the versatile physicochemical properties shown by graphene, the nano-building block of all the graphene based membranes and is expected to have a huge impact in the current membrane technology. This chapter aims to present all the developments and progresses witnessed in graphene based membrane research, both from a theoretical and experimental perspective. Based on the main transport pathway in graphene based membranes, the chapter is divided into three sections: molecular transport through (1) artificially created pores/ inherent pores in CVD grown/mechanically exfoliated graphene; (2) artificial angstrom scale graphene channel by van der Waal assembly of graphene crystals; (3) assembled GO laminate. In each section, the fabrication route to construct the respective molecular transport pathway, the protocol for water/ion transport measurements, the fundamental transport mechanism and its impact on water desalination, gas/ion separation and other applications are summarized.

2.2 Nanoporous graphene membranes

2.2.1 Introduction to nanoporous graphene membranes

Despite being the thinnest membrane, a defect free monolayer of graphene is impermeable to all atoms and molecules[1, 2] except for thermal protons, which are highly permeable at room temperature[3]. The impermeability to all ions and gaseous molecules is due to the fact that graphene's p-orbitals form a highly dense delocalised electronic cloud that blocks the gap within its aromatic rings. Theoretical calculations performed by Berry and his colleagues[2] in 2013 showed that there is no vacant space in the electron-density around the aromatic rings to allow the permeation of molecules (Figure 2.1c). If the vdW radius of carbon atom of 0.11 nm is added, the geometric pore size of graphene would decrease from 0.246 to 0.064 nm, which is smaller than the diameter helium (0.28 nm) and hydrogen (0.314 nm), making it the thinnest barrier ever known to science. The impermeability and robustness of graphene membrane motivated the theoretical and experimental research alike to focus on porous graphene membranes as a selective barrier for water filtration and gas separation applications. Graphene's impermeablity to gas molecules was first demonstrated experimentally by Bunch *et al.*[1] in 2008.

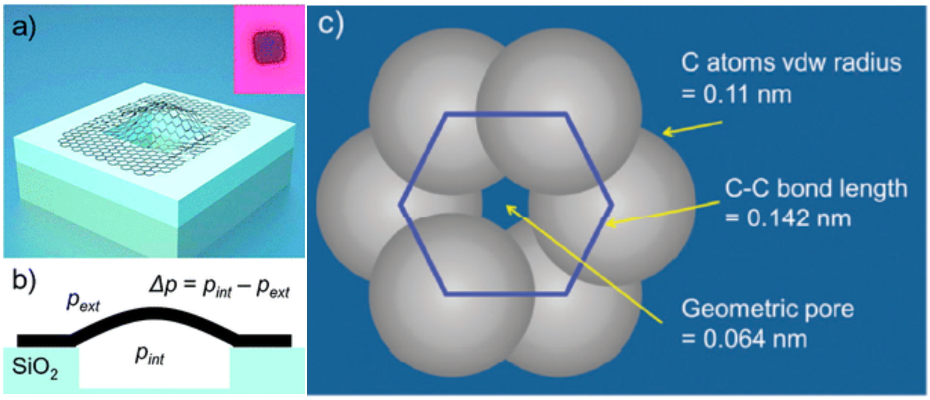

***Figure 2.1 Impermeability of Graphene membranes. (a)** Schematic of a graphene capped micro chamber. (Inset) optical image of a single atomic layer graphene drumhead on 440 nm of SiO2. The dimensions of the microchamber are 4.75 µm× 4.75 µm× 380 nm. **(b)** The side view schematic of the graphene sealed microchamber. Reprinted from ref[1].Copyright 2008, American Chemical Society. **(c)** Geometric pores of graphene. Reproduced from ref[4].Copyright 2015, Royal Society of Chemistry*

Permeance of several standard gases was tested through a graphene sealed micro-cavity (Figure 2.1 a, b). The leak rate values were calculated by measuring the pressure change across the membrane. The leak rate didn't change with the membrane thickness which indicates the leak is neither through the graphene sheets, nor through the intrinsic defects in the sheet. The thickness independent nature of the leak rate confirmed the impermeability of graphene membrane. Followed by this, Sint *et al.*[5] employed molecular dynamics (MD) simulations to investigate the ion diffusion through functionalised graphene nanopores with a pore diameter of ~5 Å.

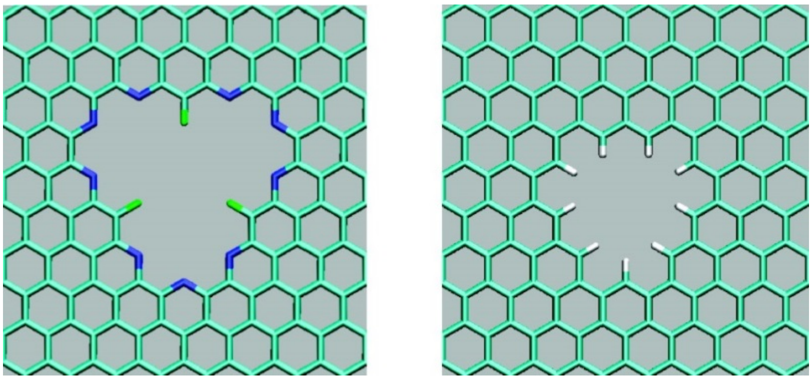

Figure 2.2 Functionalized graphene nanopores**.** ***(Left)*** *The N-terminated nanopore.* ***(Right)*** *The H-terminated nanopore. Reproduced from ref*[5]*.Copyright 2008, American Chemical Society.*

They observed that nanopores terminated by negatively charged atoms, such as nitrogen and fluorines (F-N-pore), will favour the passage of cations (Figure 2.2). Whereas, (H-pore), the pore terminated by positively charged hydrogens, facilitate the passage of anions. The nanopores could be introduced into the graphene lattice in several ways such as ion etching and the chemical modifications by local oxidation. This is the first demonstration highlighting the scope of graphene nanopores as ion selective membrane for desalination and water filtration applications. In another simulation work, Aluru's group investigated the water transport through ultrathin (less than 10 nm) porous graphene membranes (in both cases pore size varies from 0.75nm to 2.75nm) and compared its performance with the CNT of same pore size[6]. For smaller pore diameters, the CNT's water flux was higher compared to a porous graphene membrane with a correlated single file movement of water molecules. However for larger diameters, the water flux of graphene membranes was higher than of CNTs, deviating from the single file structure to bulk. Pioneering simulation work of Grossman *etal.*[7] on nanoporous graphene membrane showed that nanometer sized pores in single-layer freestanding graphene can filter out NaCl effectively from water. Their work represents the first attempt of using graphene nanopores for desalination applications. The computational study mainly examined how the desalination dynamics of single layer graphene membranes vary with pore size, pore chemistry, and applied hydrostatic pressure. It was found that the pores must have a threshold diameter to allow the permeation of water molecules and the diameter should not exceed 5.5 Å; the critical diameter, above which all ions entering the pore can easily cross the membrane without experiencing the presence of any barrier. To understand the influence of pore chemistry on the permeability-selectivity trade off, pores were passivated with hydrophilic and hydrophobic functionalities: hydrogen atoms and hydroxyl groups (Figure 2.3). The pores terminated with hydroxyl (-OH) groups shows an enhancement in the water permeability compared to the H terminated pore. This could be due to the larger amount of hydrogen bonding networks inside the hydroxyl terminated pore. In contrast, the salt rejection for the H-functionalised pore is significantly higher than that of OH-functionalized pore which could be attributed to the hydrophilic nature of the OH- terminated pore. The hydrophilic OH groups would facilitate hydrogen bond formation with salt ions as in the case of water molecules, hence a lower free energy barrier for ions entry into the nanopore. In the case of hydrogenated pores, the pore passivation with hydrogen atoms makes it hydrophobic, restricting the hydrogen bond formation with the salt ions, resulting in ion selectivity enhancement.

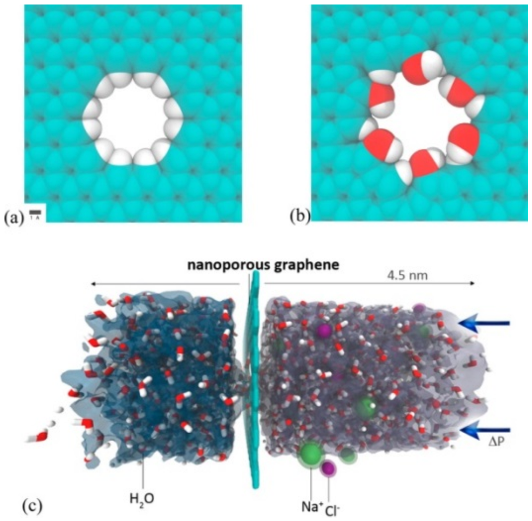

Figure 2.3 Nanoporous graphene membrane cleans up water. ***(a)*** *Hydrogenated and* ***(b)*** *hydroxylated nanoporous graphene membranes* ***(c)*** *Side view of the simulation system used in the work.Reproduced from ref*[7]*.Copyright 2012, American Chemical Society.*

Overall, their computational results show that the water can flow through graphene nanopores at a rate of 10−100 L/cm^2/day/MPa with good salt rejection and the flow rate is

2 to 3 orders of magnitude higher than that of commercially available reverse osmosis (RO) membranes, projecting nanoporous graphene membranes an excellent candidate in filtration and desalination applications.

Gas permeability and selectivity of graphene membrane with well defined sub nanometere pores were first proposed theoritically by Jiang *et al.*[8]. The theoretical calculations gave an estimation of the diffusion barrier for gas molecules through nitrogen terminated pores (3 Å) and hydrogenated pores (2.5 Å). The H_2/CH_4 selectivity was as high as 10^8 and 10^{23} for the nitrogen and hydrogen functionalised pores and the performance is superior to the state-of-the-art polymer and silica membranes.

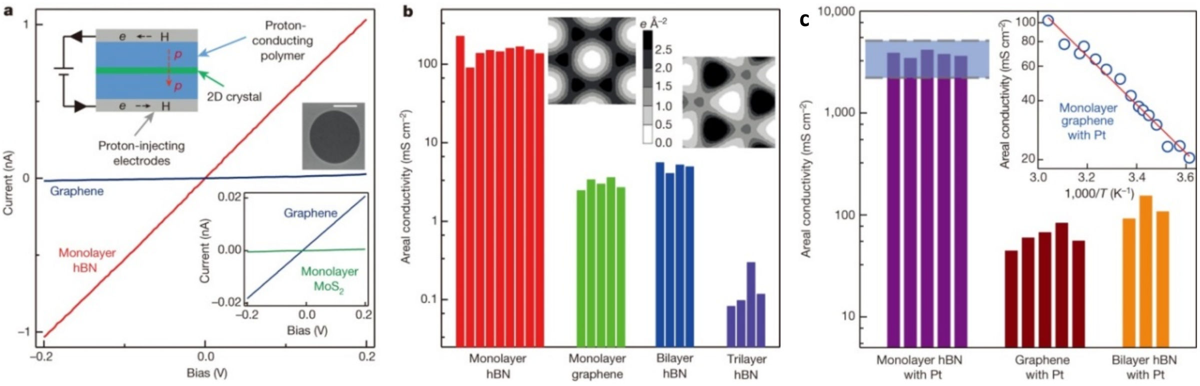

***Figure 2.4 Proton transport through 2D crystals**. **(a)** I–V characteristics for monolayers of hBN, graphite and MoS_2. Inset shows a sketch of the experimental set-up. SEM image of graphene membrane (scale bar: 1μm). **(b)** Proton conductivity of different 2D crystals and the statistics showing the measurement reproducibility. Inset show the charge densities of graphene (left) and hBN (right).**(c)** Proton conductivity of 2D crystals decorated with catalytic nanoparticles and the Inset shows the Arrhenius-type behaviour observed for proton permeation. Reprinted with permission from ref[3].Copyright, 2014, Springer Nature.*

The breakthrough discovery regarding graphene's permeability to protons was reported by Hu *et al.*[3]. They measured the electric current across micrometre-sized flakes of graphene, hBN or MoS_2 sandwiched between hydrated nafion membranes. Regardless of all the existing theories explaining its barrier behaviour [1, 2], the study found that protons pass through the ultra-thin crystals easily and the conductivity can be increased further by decorating them with catalytic nanoparticles such as platinum. Except for MoS_2 membranes, a significant proton current was observed across the other two membranes, graphene and hBN and the current was higher for hBN (Figure 2.4).The proton conductivity of both monolayer graphene and hBN showed Arrhenius-type behaviour. The unexpected passage of protons through these crystals is originating from the porosity of atomically thin electron clouds. The high proton conductivity through 2D membranes of graphene and hBN demonstrates its realistic possibilities as proton exchange membranes in fuel cells. In addition, the zero point energy difference between protons and deuterons in 2D crystals of graphene and hBN could be used for hydrogen isotope separation, showing a separation factor of 10 between protons and deutrons[9].

The simulation studies on single layer graphene membranes for ion sieving, desalination and gas separation applications show the great potential of nanoporous graphene membranes. To realize nanoporous single/ multilayer graphene membranes for desalination, pores of similar or smaller size than the hydrated ions need to be drilled on the graphene lattice. The pores can be introduced into the CVD grown or mechanically exfoliated graphene sheets using oxidative etching or electron/ion bombardment. Inherent pore generation may occur in the CVD grown graphene sheets due to the formation of grain-boundary and point defects, resulting in leakage pathways in the system. This will make the system more complex and hard to disentangle the contribution of the intrinsic defects and drilled holes. Extra care is needed for the optimization of the growth conditions of CVD synthesis for a high quality graphene sheet.

2.2.1.1 Nanopore generation in graphene membrane

A nanopore is a nanometre sized gap within a membrane, formed by either pore-forming proteins (biological pore) or as a hole in synthetic materials (solid-state pore) such as silicon or graphene[10-12]. Biological pores are formed through specific transmembrane proteins that are found naturally in cell membrane, acting as transporters for ions and molecules in and out of the cell membrane. In typical customized biological measurements a single protein nanopore is perforated into a lipid bilayer membrane and single channel measurements are performed. In solid-state nanopores the artificial gaps within a solid state membrane are fabricated using state- of -the art- engineering techniques. The pores are fabricated either by a focussed ion or electron beam with a tunable size, having precision down to sub nanometre.

Potential application of graphene membrane for molecular sieving and filtration applications depends on the ability to introduce high density and chemical stable sub-nanometre pores. Irradiating graphene with focussed electron beams above the carbon knockout potential (~80 kV) will create pores smaller than 2 nm [13-15] and the oxidative processes can be applied to create pores of desired sizes in larger macroscopic areas[16-18]. The exposure of graphene to high-temperature atmospheric oxygen, ozone, ultraviolet light [16, 19] and hydrogen plasma[17] has been reported (Figure 2.5) as effective methods for the creation of pores in larger areas. However, extra defects can be introduced during the etching process due to the vigorous reactivity of the carbon atoms with the etching species [20-22]. Moreover, these oxidation techniques generally lead to the pores of variable size[17], as the grain boundaries in graphene are more reactive than the basal planes. Russo *et al.*[23] used diffusive electron beam on defective graphene for the pore enlargement instead of oxidative etching.

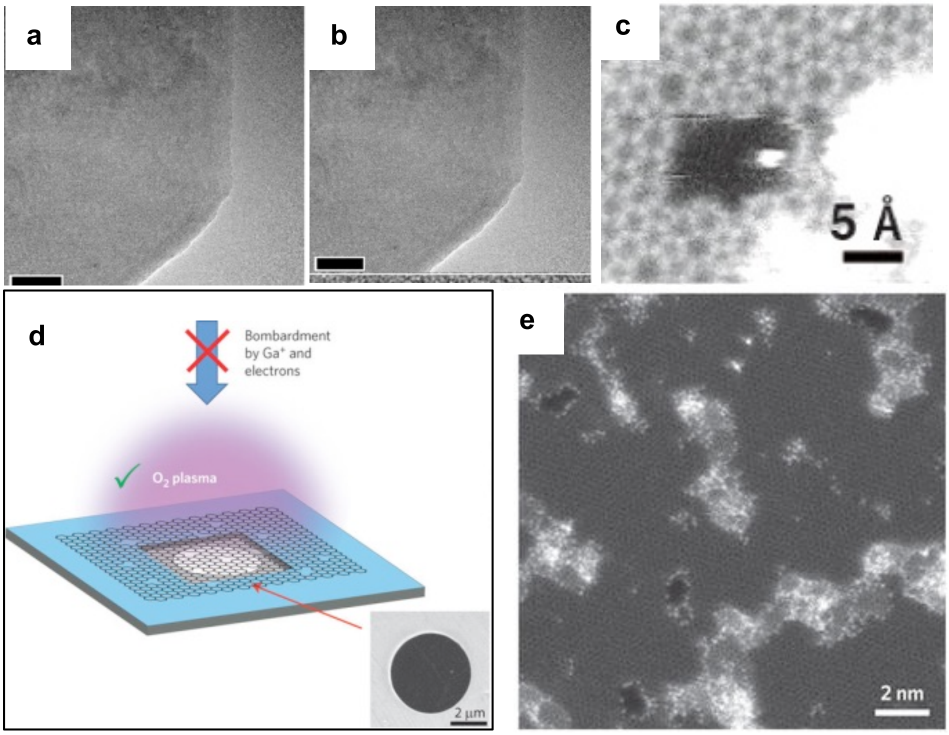

Figure 2.5 Different ways to create pores in graphene membrane. (a), (b) *TEM image of a suspended graphene membrane before and after the pore creation by electron beam ablation. Scale bar, 50 nm and 2 nm. Reproduced from ref[24].Copyright 2008, AIP Publishing.* ***(c)*** *Sub nanometre pores in graphene membrane made by ion bombardment and oxidative etching. Reproduced with permission from ref[25]Copyright 2014, American Chemical Society.* ***(d)*** *Schematic and SEM image of single-layer graphene sheet suspended on a 5-µm-diameter hole covered with nanometre pores produced by oxygen plasma treatment.* ***(e)*** *Aberration-corrected STEM images of graphene after 1.5 s exposure to oxygen plasma. Pore size is ~1 nm. Reproduced from ref[26], Copyright 2015, Springer Nature.*

2.2.1.2 Molecular transport through nanoporous graphene membranes

The first attempt, demonstrating the formation of isolated and selective synthetic pores on mechanically exfoliated graphene membrane was shown by Bunch *et al.*[19]. The same experimental protocol was used as in the pressurized blister test of graphene membranes[1] and angstrom scale pores were introduced through ultraviolet-induced oxidative etching technique. Mechanical signals were used to measure the transport of gas molecules through the porous graphene membrane, which later could be converted into the leak rate and separation factor. According to them, the etching technique is the only method able to successfully generate controllable pores in the graphene lattice with angstrom resolution. The result match quite well with the theoretical prediction and was a landmark in realizing the potential aspects of graphene for gas separation.

First approach of using CVD graphene membrane as selective molecular sieve was reported by Karnik's group[27]. Using pressure driven filtration experiments they observed size selective transport of ions and molecules through single layer CVD graphene. The selective molecular/ion transport is attributed to the commonly occurring intrinsic pores with diameters of 1-15 nm, formed during the CVD growth process. Inspired by the selectivity offered from the intrinsic defects in CVD graphene membrane, the same group tested the gas transport in CVD graphene membrane[28]. The micrometre scale tears and nanometre scale defects present in the CVD grown graphene membrane were characterized by measuring the permeance of standard gases. A theoretical model encompassing the contribution of intrinsic defects and tears has been developed and matched quite well with the experimentally measured flow rates. Their results indicate that the gas transport is defect mediated, as the transport through the interlayer galleries formed by the graphene layer stacking is negligible. To employ graphene membranes for separation and filtration purposes at a pilot scale, it is necessary to have high-density, controllable and chemically stable sub nanometre pores. In this line, it is possible to create isolated and reactive defects in macroscopic single layer graphene membranes by ion bombardment and such defects can be enlarged later into permeable pores with diameters of 0.40 ± 0.24 nm using acidic potassium permanganate etchant[25]. The onset of the defect creation by gallium ion bombardment is evident from the appearance of defect related raman peaks[28]. The measured membrane potential, using a KCl solution, shows selectivity in the transport of K^+ ions over Cl^- ions. The observed selectivity originates from the combined effect of the pore size and the charge interaction between the negatively charged groups terminating at the pore edges and the ions. A significant progress was achieved by Surwade *et al.*[26]; the possibility of using single layer graphene sheet for water desalination. Effort has been made to examine experimentally, the transport of ions and water molecules through stable sub nanometre pores on a suspended single-layer graphene membrane. Pores are created on the CVD grown single layer graphene membrane by exposing it to oxygen plasma for a short period of time and is evident from the increase in the I_D/I_G ratio. Weight loss, ionic conductivity and forward osmosis experiments across nanoporous single layer CVD graphene membranes (Figure 2.6) demonstrate its great potential for water treatment applications with a notable flux of $\sim 10^6$ g m^{-2} s^{-1} combined with excellent water-ion selectivity.

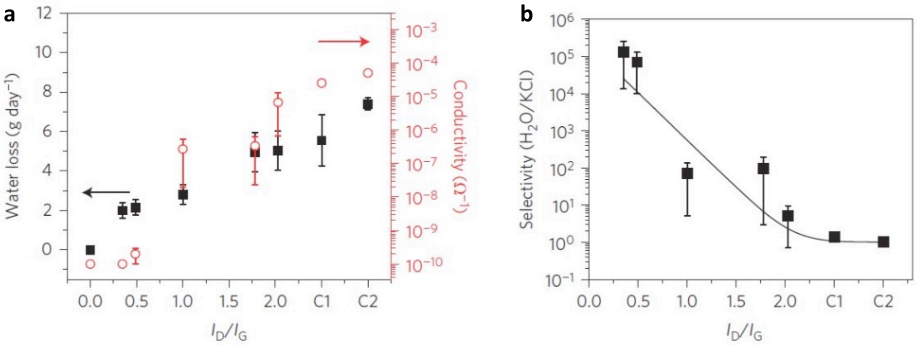

Figure 2.6 Water desalination using nanoporous single layer graphene membrane.

(a) *Water loss after 24 h through nanoporous single layer grapheme and the second y axis shows ionic conductivity through the same membrane .Both measurements were done by varying the I_D/I_G ratio (different exposure time to oxygen plasma).* ***(b)*** *Water/salt selectivity as a function of I_D/I_G ratio. Reprinted from ref*[26]*, Copyright 2015, Springer Nature.*

During the CVD growth process on copper substrates and the graphene transfer, there is a high chance of defect formation and tears (~100–200 nm) [27] in the membrane. Intrinsic defects and tears in the CVD grown graphene will degrade the potential aspect of graphene membrane for desalination applications. The occurrence of such inherent defects can be sealed by coating graphene with metal oxides. [29] The defects on graphene were sealed by selectively coating the graphene with HfO_2 using atomic layer deposition (ALD) followed by interfacial polymerization. A hafnia deposition on graphene decreased the flux of potassium chloride to ~40%, and the successive interfacial polymerization further decreased it to ~8% of that across a PCTE membrane without graphene. The KCl flux decrease is a proof for the defect sealing in CVD graphene membrane.

2.3 Artificial graphene nanochannels

2.3.1 Atomic scale graphene nanocapillaries

Membranes with pore dimensions approaching nanometre scale have long been studied because of exotic fluid phenomena arising at the molecular scale. The recent development of nanofabrication techniques has enabled the researchers to fabricate such permselective synthetic membranes, which opens new avenues to be explored in the field of nanofluidics[30-32]. In fact, studies related to fluidic behaviour have long been demonstrated in membrane and colloidal sciences, the exact usage of the term nanofluidics has started with the emergence of state–of-the-art nanofabrication techniques, thus allowing the fabrication of nanofluidic channels and devices [33]. A nanochannel or nanocapillary is a hollow structure with at least one dimension of its cross section in the range of 1–100 nm[34, 35]. Based on the cross-sectional configuration, nanochannels can be classified into "two dimensional (2D)" nanochannel i.e. nanoslit with width/length in the nanometre regime or a "one-dimensional (1D)" nanochannel or a nanotube with its diameter in the nanometre regime. There are two possible ways to fabricate nanochannels, top down approach and bottom-up approach[36]. Top down approach often uses microfabrication techniques to create nanoscale structures by milling/ shaping of the material. The technique has realized nanochannels with diameter as small as to 2 nm, but further reduction in the size is limited by the surface roughness of the channel[37]. The other way, bottom up approach, generally employs molecular self-assembly to produce nanoscale designs by assembling nanomaterials atom-by-atom or molecule by molecule.

Due to the limitations of the surface roughness of conventional materials and the limited flexibility in both top down and bottom up approaches, it has been found extremely difficult to fabricate nanochannels/capillaries of tunable angstrom scale dimensions. Boya *et al.*[37]developed a novel approach by utilizing the atomic flatness of van der Waals layered materials for the fabrication of sub-nm channels, beating the surface roughness limit traditionally encountered in lithographically fabricated systems. This technique utilizes a combination of van der Waals assembly of layered materials and lithography to create fluidic channels with predetermined physical and chemical characteristics.

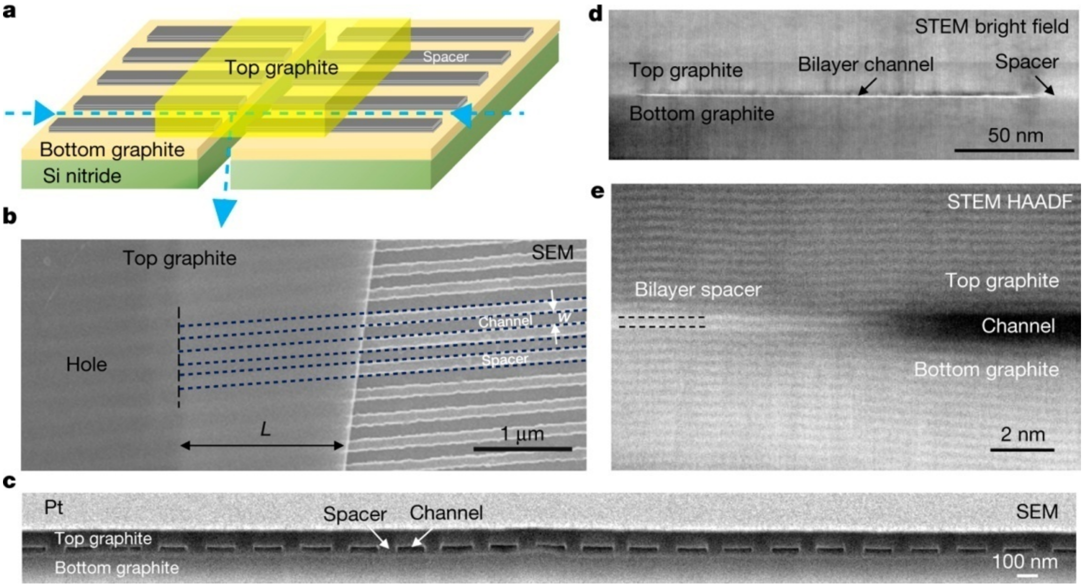

Figure 2.7 Atomic scale graphene capillary devices. *(**a**) Schematic of the fabricated graphene capillary devices. The arrow indicates the flow direction. (**b**) SEM image of the fabricated device containing trilayer graphene channels. The three spacers used in the trilayer devices were shown by dotted lines. (**c**) SEM micrograph of one of the fabricated device showing a bench of capillaries with height h ≈ 15 nm. (**d**) STEM bright field cross sectional image of a bilayer capillary (h ≈ 7 Å). (**e**) High-angle annular dark field (HAADF) image of the edge of the channel. Reproduced from ref*[37]*.Copyright 2016, Springer Nature.*

The structure of graphene capillary devices consists of atomically flat top and bottom graphite crystals that are separated by a bunch of spacers made from graphene with a precisely controlled number of layers (Figure 2.7) and the assembly is held together by vdW forces. While the capillary structure is constructed, the individual atomic planes have been removed from a bulk crystal, which results in flat voids or cavities of desired height with precision in the atomic scale. The highlight of the structure is the vast variety of options to study the ion/water transport behaviour in different conditions. The provision to examine the fluid behaviour not only at different capillary heights but also with different spacer materials to account their exciting surface properties is uniquely achieved by this method.

2.3.2 Water flow through graphene nanocapillaries

To understand the behaviour of nanoconfined water and its dynamics in atomically smooth graphene capillaries, Boya *et al.*[37] performed gravimetric measurements. For the weight loss measurements a Si nitride chip containing graphene capillary device was used to seal the small water filled container. The observed water flux *Q* was found to vary with 1/*L,* which explains that the evaporation rate was limited by permeation through the capillary. As the height of the capillary *h* decreases from~ 10 nm, *Q* also decreases, as expected. When the capillary height is decreased down to 2 nm, a sudden jump in the *Q* value can be observed with an order of magnitude difference compared to bulk 30 layer channels with a sharp peak at *N* = 4–5 (Figure 2.8). MD simulations show that the slip length is high (~60nm), but didn't vary much with the capillary height *h*. The large slip length inside the capillary could be due to the higher hydrophobicity of the spacers and the confining graphitic wall which makes the water flow faster, due to the frictionless interaction with the graphitic surface. To match the experimental *Q* with the theoretical value given by the classical Hagen-Poiseuille (HP) equation, the capillary pressure should be in the order of 1000 bar. The water flow in 4-5 layers showed some unprecedented behaviour quite different from the rest and is explained by the coupled effect of two kinds

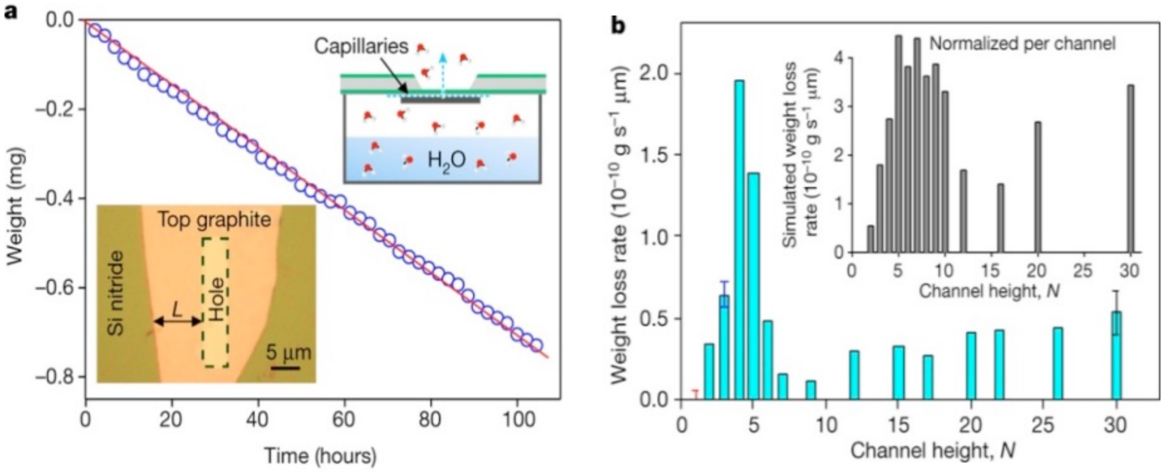

Figure 2.8 Water transport through graphene nanoslit. (a) *weight loss by water evaporation through a graphene trilayer device, capillary height Na=10.2 Å. Bottom inset, optical image the trilayer device containing 200 parallel channels with L ranging from 3.6 μ m to 10.1 μm. Top inset, schematic of the gravimetric measurements* ***(b)*** *Functional dependence of water flux Q on capillary height. Inset, flow rates found molecular dynamics simulations. Reproduced from ref[37], Copyright 2016. Springer Nature*

of pressure; pressure due to a curved meniscus and disjoining pressure [38-40]. Inspired from the demonstrated graphene channel assembly, Xie *et al.*[41, 42]also fabricated a graphene nanofluidic channel on Si substrate and studied the interplay between slippage effect and fast water transport.

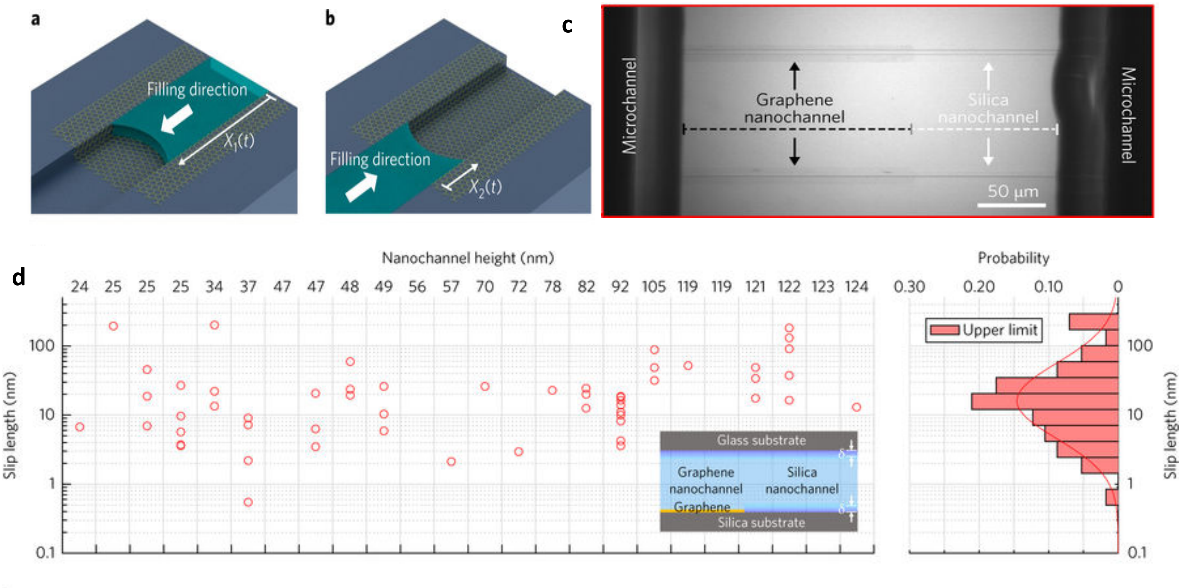

Figure 2.9 Hybrid Si-graphene nanochannel design and water transport measurements.(a), (b) *schematic of the water filling in in graphene and silicon nanochannel from graphene and silica side.* ***(c)*** *Optical image of fabricated hybrid nanochannel.* ***(d)*** *Extracted slip length from for different channel height which entails the graphene coverage/quality. The histogram on the right side shows the slip length distribution with statistical median of 16 nm. Reproduced from ref[41]. Copyright 2018, Springer Nature.*

The hybrid nanochannel structure consists of a graphene nanochannel connected with a silicon nanochannel (Figure 2.9). In the capillary filling measurements, water is introduced into the hybrid channel. The mass flow resistance ratio in the 2 channels was determined from tracking the water meniscus. The flow resistance ratio was examined for a range of nanochannel heights ranging from 24 nm up to124 nm and extracted the slip length accordingly. The extracted slip length varies largely from 0-200 nm and no functional dependence on the channel height with a statistical median of 16 nm. The observed large variations in the value for slip length were due to the functional groups charges bearing at the graphene surfaces.

2.3.3 Ion transport through graphene nanocapillaries

Ion drift measurements on artificial graphene nanochannels were done for the first time by Xie *et al.*[42]. The ionic conductance of silica channels coated with graphene films was higher than the bare silica channels, leading to an enhanced electro-osmotic flow, which is attributed to the presence of surface charge on graphene surface. Following the water transport measurements on the angstrom scale graphene capillaries, the ion conductance through angstrom scale slits (Figure 2.10) with different confining wall materials such as graphite, MoS_2 and hBN[43] were performed. For the spacer layer, two layer (L) graphene and 1L MoS2 were used. The nanoslit device had a height of 6.6 and 6.7 Å defined by the vdW thicknesses 2L graphene 1L MoS_2 crystals. The ions flow through the slit when voltage was applied and the channel conductivity was observed to be dependent on the cation types. More interestingly, a cut-off was not observed even with cations with hydrated diameter larger than the channel height. This anomaly is easily understood if we consider the fact that, when flowing through the angstrom scale capillaries, ions are not like hard balls, but instead behave like soft balls, but instead they can squeeze and rearrange their solvation shell to get inside the capillary The ease of such reconfigurations of the hydration layer depends on the hydration energy of the ions. Ion mobility measurements using electro diffusion showed that the chloride ion mobility was different for different salt as evident from the membrane potential measurements.

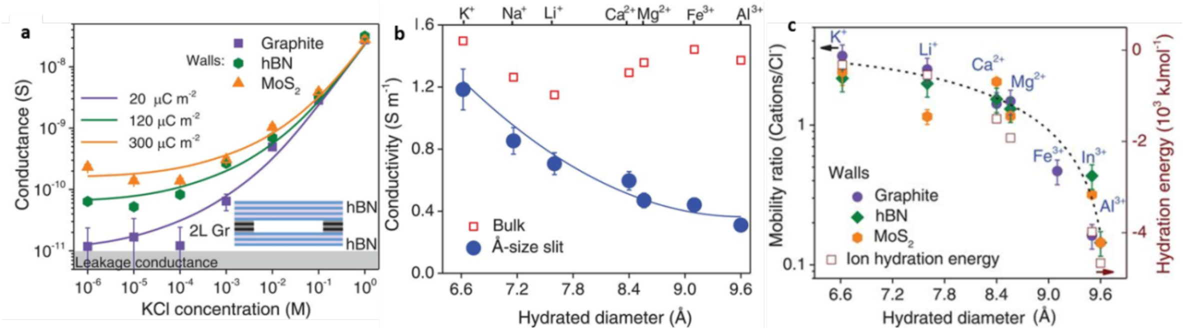

***Figure 2.10 Ion transport and mobility under angstrom scale confinement**.*

***(a)** Conductance of slit device with Graphite, hBN and MoS2 as confining wall and 2L graphene as spacer. **(b)** Effect of ion's size in channel conductivity. **(c)** Mobility ratio* μ^+/μ^- *as a function of cations hydrated diameter for slits made from graphite, hBN, and MoS2 using 2L graphene as spacer. Open squares represent the ions' hydration energy. Reproduced with permission from ref*[43]*. Copyright 2017, American Association for the Advancement of Science*

2.4 Assembled GO laminates

2.4.1 GO Membrane: the ultimate membrane material

It has been found that creating high-density and controllable sub-nm pores in graphene membrane by ion bombardment and etching processes is extremely difficult and challenging, because of the stochastic nature of the involved processes. Even though the water permeability value of porous single layer graphene membrane is a benchmark against the existing commercial desalination membranes[7], the deterioration of its mechanical properties with high density pore generation and lack of industrial scalability limits its practical application. To address these challenges the idea of self-assembly has come up, where 2D materials can be restacked via vacuum filtration or evaporation assisted self-assembly of exfoliated 2D sheets (Figure 2.11) into a macroscopic well-ordered membrane form. The 2D sheet assembly is held together by van der Waals interactions, which is proportional to the overlapping surface area and the fourth power of the inverse inter-sheet distance. For instance, each individual GO sheets can be piled on top of each other to form a tightly packed interlocked laminate, having a structure similar to nacre with exceptional sieving properties, which makes GO an interesting candidate in filtration and separation applications. Briefly, graphene oxide is an oxygenated graphene sheet, which is randomly decorated with oxygen rich functionalities, such as epoxy, hydroxyl, carbonyl and carboxyl groups, in the basal planes and edges [44-46]. Furthermore, this oxygen containing functional groups act as specific sites for covalent or non-covalent modifications[47]. The carbon atoms bonded to the oxygen atoms in the form of functionalities will distort the lattice, forming nanoscale wrinkles and structural defects creating amorphous region due to the formation of sp^3C-O bonds[45, 48]. Due to the enriched oxygen containing molecules on the GO, the material can easily be dispersed in water by sonication without the aid of any additional surfactants[49, 50], which helps to assemble the individual GO sheet into multilayer laminar membrane with desired thickness. In addition, the presence of oxygen rich functional groups gives a wide range of opportunities to tailor the mechanical, electrical, chemical and thermal properties of GO membranes, highlighting GO as an interesting platform to develop new nanostructures with novel multifunctionalities. GO sheet become negatively charged when dispersed in water due to the ionization of the carboxyl groups on the edges of GO sheets[51] and this was demonstrated through zeta potential measurements[52]. The GO suspension is highly stable in water even for months due to the strong electrostatic repulsion between the negatively charged GO layers preventing GO from agglomeration. The layered structure of GO can be considered as a cascading array of parallel individual nanosheets which are locked together by hydrogen bonding and span the complete thickness of the membrane, leaving behind a network of pristine graphene nanocapillaries [53]. The individual layers of GO are heterogeneous in their composition, consisting of holes, oxidized regions and graphitic region. The distribution of these three domains depends on the degree of oxidation. On membrane assembly, the various sp^2 clusters are interconnected across the stacking layers to form a capillary network, which creates a highway for the transport of water and ions[53, 54]. The ease of the self- assembly of GO sheets is benefiting from the size L of the GO flakes, typically around 0.5-30 micrometres. The sheets are separated by a distance d; the interlayer spacing is highly dependent on the water content inside the membrane[53]. The resistance free permeation of water, precise size cut-off and ultrafast molecular sieving of ions[53, 54]through GO membranes opens a new horizon in the membrane field, where graphene oxide could be widely used for filtration and separation applications.

2.4.2 Preparation of GO membranes

The large aspect ratio of 2D materials will increase the mutual interaction between the 2D sheets, which promotes individual sheets to form laminar membranes. The one important merit of graphene oxide nanosheets over nanoporous graphene membranes is the cost effective way of its mass production via simple chemical oxidation of the parent material graphite and the ultrasonic exfoliation, which significantly reduces the manufacturing cost of GO laminates.

2.4.2.1 Vacuum Filtration

Vacuum filtration is known to be the most commonly used method for the preparation of GO membranes. Here, the graphene oxide suspension with a known concentration is filtered through a support membrane (alumina anodisc, porosity~ 20nm-200 and other polymeric support) in a vacuum filtration assembly. The applied differential pressure pushes water through the anodisc (or any substrate) leaving behind the GO crystallites on the substrate. The thickness of the membrane depends on the volume and concentration of the GO suspension used and ranges from few nanometres [55] to tens of micrometres [56]. It is worth noting that the vacuum filtration method didn’t alter the physicochemical properties of the GO membrane .This is because; the interactions between the GO sheets; electrostatic, hydrogen bonding and van der Walls interactions are purely non-covalent in nature. As the size of the film, prepared by this method, is limited by the size of the filtration apparatus, this method is not practically viable for the mass production of large area GO membranes.

2.4.2.2 Drop-casting

Drop casting is a coating technique where GO membrane assembly is formed by drop casting few ml's of GO solution onto a smooth surface such as silica or paper and drying at room temperature [57]. After proper drying, free standing GO membrane can be peeled off from the underlying substrate.

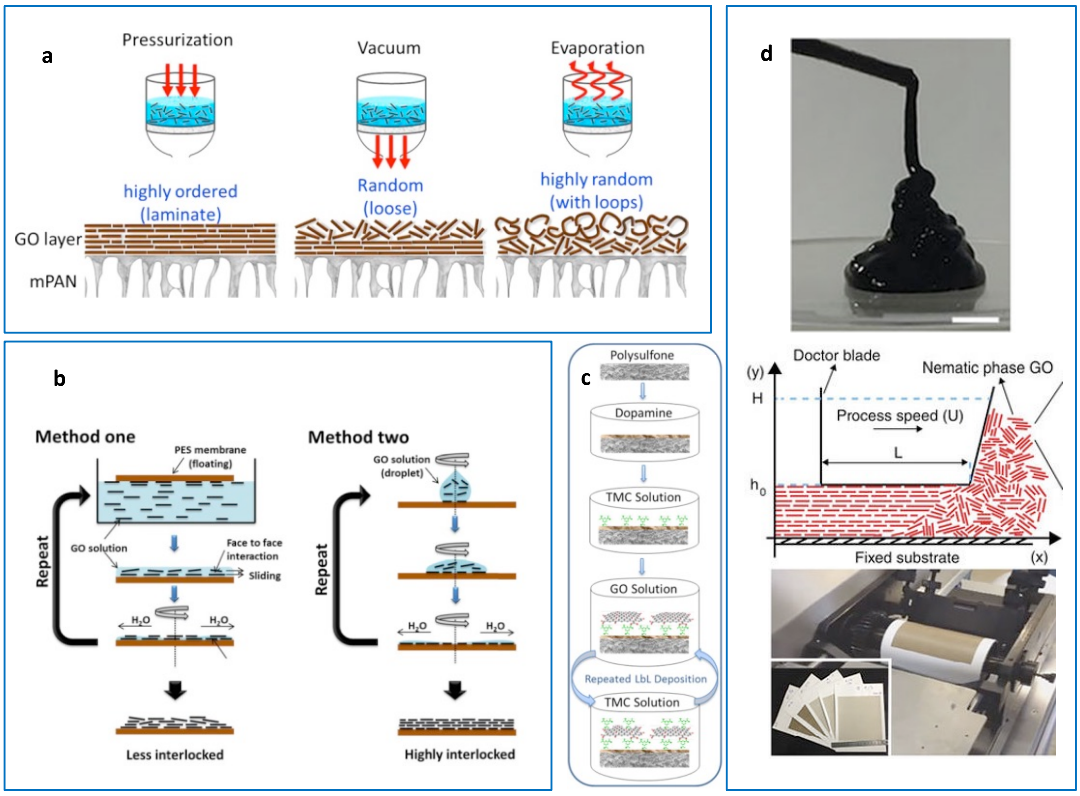

Figure 2.11 Schematic of GO membrane preparation by different techniques.

(a) *Pressure assisted self-assembly, vacuum filtration, evaporation induced self-assembly. Adapted from ref[58]. Copyright 2015, Elsevier* ***(b)*** *Spin coating methods, method 1 is similar to the Langmuir-Schaefer (LS) method. Reproduced from ref[59].Copyright 2013, American Association for the Advancement of Science.* ***(c)*** *layer-by-layer method. Reproduced from ref.[60].Copyright 2013, American Chemical Society.****(d)*** *Fabrication of shear-aligned membrane from nematic GO; Scale bar, 1 cm and the schematic of the shear alignment process using a doctor blade and the film obtained in the shear aligned process. Reproduced from ref[61], Copyright 2016, Springer Nature.*

2.4.2.3 Spin-coating

Spin coating is a type of coating technique used to deposit uniform films onto flat substrates[53, 62]. The substrate with minimum roughness is preferred, usually Cu foil or a polymeric support. In order to increase the deposition rate, the substrate is normally heated to~ 50 °C prior to the coating procedure. Normally, a small amount of coating material is applied on the middle of the substrate. The substrate is then rotated at a higher speed by centrifugal force so that the suspension will uniformly spread onto the substrate forming a continuous film. Free standing membrane can be obtained by etching away the underlying substrate through acid treatments. Finally, the membrane was cleaned in distilled water and dried on a hot plate (<50°C). By carefully controlling the rotation speed of the substrate and the concentration of the GO suspension, membranes with broad ranges of thickness can be fabricated. In spin coating, dense packing of the GO layers is obtained because, face to face attractive capillary force created by the spin coating will easily overcome the repulsive edge-to-edge GO sheet interactions[59].

2.4.2.4 Spray coating

The spray coating method involves using a spray coating unit to spray the suspension onto a target and the solvent is evaporated subsequently to get a film of desired thickness[63]. An airbrush is used to nebulize the GO suspension, forming small droplets. Some carrier gases, for example N_2 can be used to spray the suspension. The advantage of this spray method over other technique is the remarkably high production efficiency and scalability. A large area membrane can be prepared on any substrate with relatively simple fabrication procedures. However, the homogeneity of the membrane prepared by this method needs to be improved.

2.4.2.5 Langmuir–Blodgett (LB) method

The Langmuir–Blodgett (LB) method is a technique for the fabrication of single layer thick films with great control over the packing density. When a monolayer is fabricated on a gas-liquid interface or a liquid –liquid interface, the film is called Langmuir film and the Langmuir film deposited on any solid substrate is called a Langmuir-Blodgett film. In this method, insoluble monolayers are formed on top of a clean liquid with high surface tension (e.g. water) by spreading the non-volatile material over the Langmuir trough with a controlled speed. Spreading happens when the molecules of the material to be filmed consists of a hydrophilic head and a hydrophobic tail. The molecules interaction with water molecules should be greater than the internal interactions[64]. As GO is an amphiphilic material[65] (contain both hydrophobic and hydrophilic regions), the method is suitable for preparing GO monolayers[50, 66]. In LB technique, Langmuir trough was first cleaned with chloroform and filled with distilled water. The GO suspension was then carefully dispensed on the surface of water at a particular speed and the surface pressure of GO film was monitored using a tensiometer. By bringing the substrate slowly onto the trough and then pulling it up, GO monolayers present on the water surface were transferred onto the substrate. After drying the GO membrane in an oven followed by repeating the same protocol, bi-layer, tri-layer GO can be prepared.

2.4.2.6 Layer by layer (LbL) assembly

GO membranes can also be synthesized by the layer-by-layer assembly of GO nanosheets. The deposited sheets were stabilized internally from the combined effect of covalent and electrostatic interaction between the GO and the cross linking agents. Thickness of the membrane can be adjusted by varying the number of layer-by-layer deposition cycles[67]. B Mi *et al.*[60] demonstrated the LbL assembly of GO membrane and studied the impact on water desalination applications. Porous polysulfone membrane is used as the support which was dip coated it in dopamine solution. The support is dried in oven and immersed in 1, 3, 5-benzenetricarbonyl trichloride (TMC) solution. Soaking the support membrane in GO solution will attach the first GO layer to the support membrane. The subsequent soaking in TMC and GO creates additional numbers of TMC and GO layers and adjusting the number of deposition cycle will create GO-composite membranes with a desired thickness.

2.4.2.7 Shear alignment

An industrially adaptable, scalable method for graphene oxide membrane fabrication was achieved recently by Akbari *et al.*[61]. As the conventional methods like vacuum filtration and evaporation are time consuming and limited by the size of the filtration apparatus, it has become necessary to develop a technique, by which, GO membrane can be mass produced. The discotic nematic phase of GO can be shear aligned to form a homogeneous continuous films of multi-layered GO membrane using a commercially viable doctor blade technique. A nematically ordered liquid crystal phase of GO is obtained by using strong hydrophilic super absorbent hydrogel beads, which absorb water from GO, making it more concentrated, resulting in the phase transition from isotropic to nematic liquid crystalline phase. The non- Newtonian flow characteristics of the nematic liquid crystal phase of GO further facilitates the large scale production of GO membranes by blade coating and the shear thinning behaviour facilitate the formation of highly ordered laminated films. The doctor blade has a rectangular outlet through which a movable blade spreads the GO suspension over a porous substrate. The prepared large area (13 × 14 cm^2) membranes exhibit highly ordered laminar structures superior to GO laminates obtained by vacuum filtration.

2.4.3 Interlayer graphene capillaries in GO membranes

In monolayer graphene, the only transport pathway for the movement of ions is through the in-plane pores. Once the individual nanoporous graphene layers are stacked on top of each other into a laminar form, another transport pathway is introduced in the membrane structure known as inter-layered pores or interlayer channels. By controlling the size of the spacer layer, membranes with extremely narrow pore distribution can be obtained. It has been found extremely difficult to synthesize such laminar graphene membranes with narrow and controlled inter-layered pore distribution using vacuum filtration method because of the following two reasons:(1) pore size can't be tunable (2) difficult to produce a narrow pore distribution in every stacking layer. However, in GO membranes, the presence of oxygen rich functional groups restricts the structure from collapsing into graphitic spacing while assembling GO nanosheets into a membrane. If the water content and the functional groups are properly modulated; it is possible to achieve extremely narrow channels of sizes in the range of~ 6-10 Å[56]. Unlike the pores in nanoporous graphene membrane, the pores in GO membrane are the interlayer channels formed between every two stacked GO sheets, these channels are well connected across the membrane thickness to form a tortuous capillary network, through which ions and water molecules can realize transport from one side of the membrane to the other. The interlayer pores or channels are nanometer in size, if well controlled; provide even sub nanometre channels, which are pivotal for desalination and water filtration applications. The water and ion transport across the 2D layered GO membrane is confined in the interlayer space and the ion/ water migration can occur possibly through two pathways, along/across the plane of the laminate[53, 5456, 68]. Regardless of the transport route, the mass transport is governed by the surface properties of the reassembled GO nanosheets. Precise tuning of the inter layer spacing is inevitable to achieve the sieving of common salt in GO membrane. Different approaches have been proposed recently to achieve size controlled channels in GO membranes such as physical approaches (stacking GO sheets with nanoscale wrinkles[69] and epoxy confinement[56]), chemical approaches (covalent cross linking with molecules) and thermal treatment to name a few.

2.4.3.1 Structure of graphene capillaries

The ions and water molecules enter into the interlayer gallery of GO membranes through the edge of the GO sheet. As oxygen rich functional groups are known for clustering, they induce puckering leading to the corrugation of the nanosheets[70]. This phenomenon gives rise to the formation of large percolating regions of non-oxidized (sp^2) graphene domains with empty spaces in between, forming an interconnected network of graphene capillaries (Figure 2.12) across the thickness of the membrane.[53]. In GO membranes, water molecules and ions permeate through these nanocapillaries following a tortuous path primarily over the hydrophobic (non-oxidized) region rather than the hydrophilic (oxidized) part of GO, which leads to a slip enhanced water flow. Due to the narrow size distribution of sp^2 nanocapillaries together with the existence of oxygen containing functional groups, GO membranes are getting tremendous attention in the membrane technology field.

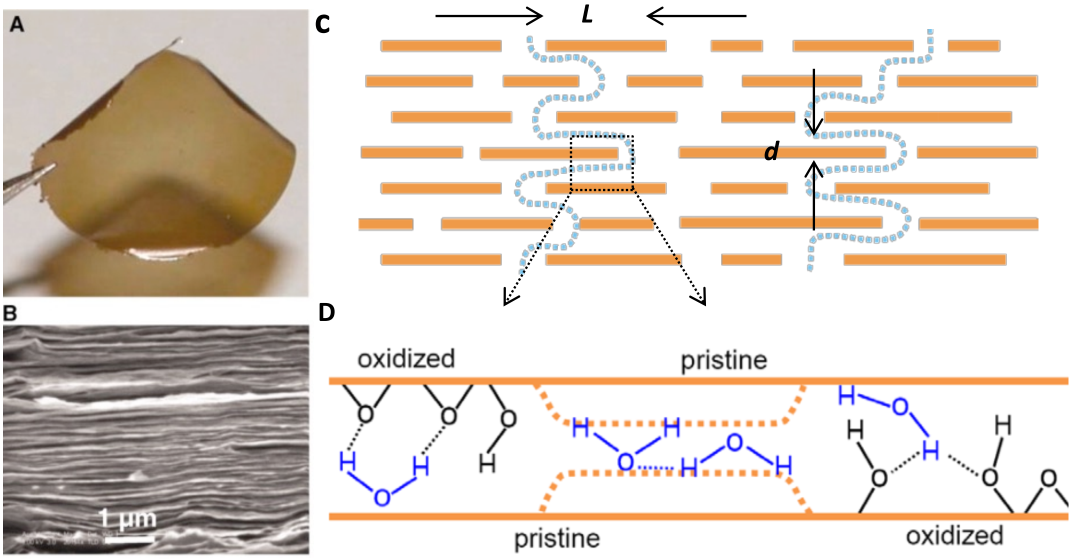

Figure 2.12 Structure of graphene oxide membrane.(a) *Optical image of a 1-µm-thick GO membrane.* ***(b)*** *SEM micrograph of the film's cross section showing the layered structure* ***(c)*** *and* ***(d)*** *Schematic showing the permeation pathway in graphene oxide laminate and the model of graphene capillaries. Reproduced from ref[53].Copyright 2012, American Association for the Advancement of Science.*

2.4.3.2 Water permeability of GO membranes

One of the game-changing breakthroughs in graphene based materials is the discovery of graphene oxide membrane which exhibits unimpeded permeation of water [53]. To study the permeation rate for water and other organic solvents through GO membrane, Nair *et al.* used a metal container filled with corresponding solutions and the aperture was sealed with a 0.5 µm thick GO membrane.

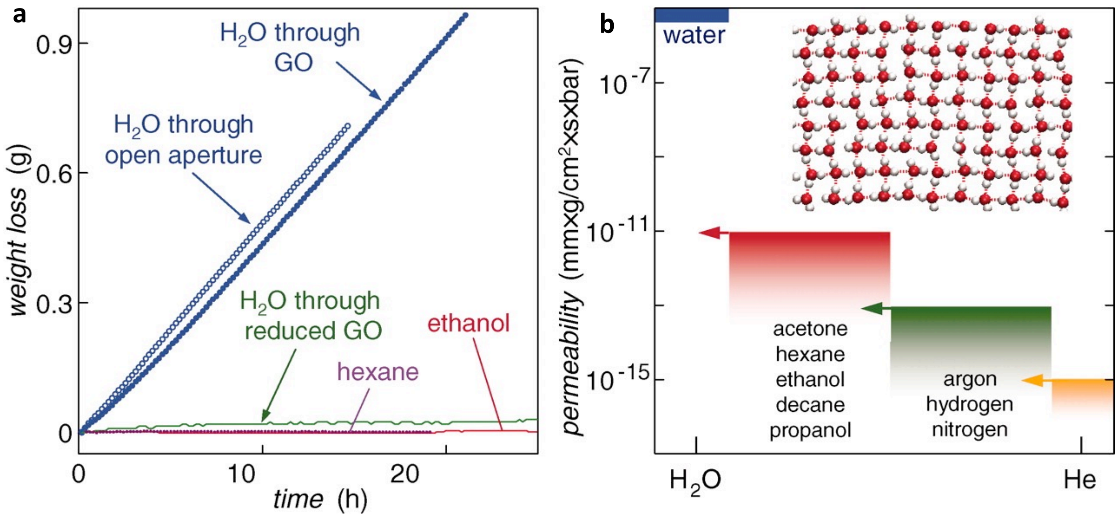

Figure 2.13 Molecular permeation through GO membrane**.** ***(a)*** *Weight loss for a container sealed with a GO film No loss was detected for ethanol, hexane, etc. But water evaporated from the container as freely as through an open aperture (blue curves). The measurements were carried out room temperature in zero humidity.* ***(b)*** *Permeability of GO membrane with respect to water and other organic solvents (arrows indicate the upper limits set by our experiments). (Inset) Schematic of the structure of monolayer water inside a graphene capillary with d = 7 Å, as found in MD simulations. Reproduced with permission from ref[53]. Copyright 2012, American Association for the Advancement of Science.*

Organic solvents used were ethanol, hexane, acetone, decane and propanol. The weight loss due to evaporation was precisely measured using a computer controlled precision balance. No weight loss could be detected with an accuracy of <1 mg when the container was filled with organic solvents during the measurements lasting a couple of days. Surprisingly, a huge weight loss (Figure 2.13) was observed when the container was filled with water. More interestingly evaporation rate was same as through an open aperture (no GO film sealing), which shows nanocapillaries provide negligible resistance towards water permeation. Furthermore, no leakage was observed through the GO membrane when the container was filled with gases such as He, H_2, N_2. The helium gas is very hard to stop in normal conditions. For instance, a 12μm thick PET sheet shows a significant helium leakage which is 1000 times higher than the leakage observed in GO membranes (thickness of 0.5μm).

The ultrafast and unimpeded permeation of water was attributed to the formation 2D graphene nanocapillaries formed by the joining of sp^2 clusters in GO membrane. Graphene oxide membrane is hygro-responsive i.e. the interlayer spacing varies with humidity. In dry state, the d spacing of GO varies from 6-10 Å depending on the water content and amount of oxidation. For a membrane with d~8-9 Å, the available free space δ can be estimated as d-a, (where a is the thickness of the graphene sheet) resulting with a free space of ≈5 Å, which is adequate to accommodate a monolayer of water[71, 72]. Diffusion of organic solvents vapours were blocked by the collapsing of the 2D capillaries in low humidity or the partial clogging with water.

2.4.3.3 Mechanism of water transport and slippage effect

The anomalous water permeation rate through helium leak tight graphene-based membranes was result from the combined effect of capillary-like driving force inside the membrane and frictionless nature of carbon walls of the 2D graphene capillaries. These two effects make the water molecules inside the channel move as a single file system as in the case of carbon nanotubes and other hydrophobic pores[73-76]. If the water inside graphene nanocapillaries behaves as a classical liquid, the mass flow through the capillaries should follow the HP equation. The measured water flux shows a flow enhancement, by a factor of 10^7 with respect to the classical laminar regime. The basic assumption of the HP equation are laminar flow and no slip boundary condition (boundary layer velocity is zero). The significant deviation of the experimentally measured water flux value from the classical HP equation questions the validity of the no slip boundary condition. MD simulation predicted that velocity of the water layer near to the graphitic surface is non-zero, reaching 20m/s resulting from the water slippage at graphitic surface[53].

The measured fluid slippage at the solid wall is denoted in terms of the slip length, defined as the extrapolated distance λ relative to the wall, where the tangential component the of fluid velocity vanishes (Figure 2.14). The slip length is introduced to connect the interaction between the solid wall and the fluid. It is straightforward to interpret the slip length in terms of liquid–solid friction at the interface and large slip lengths are associated with reduced friction

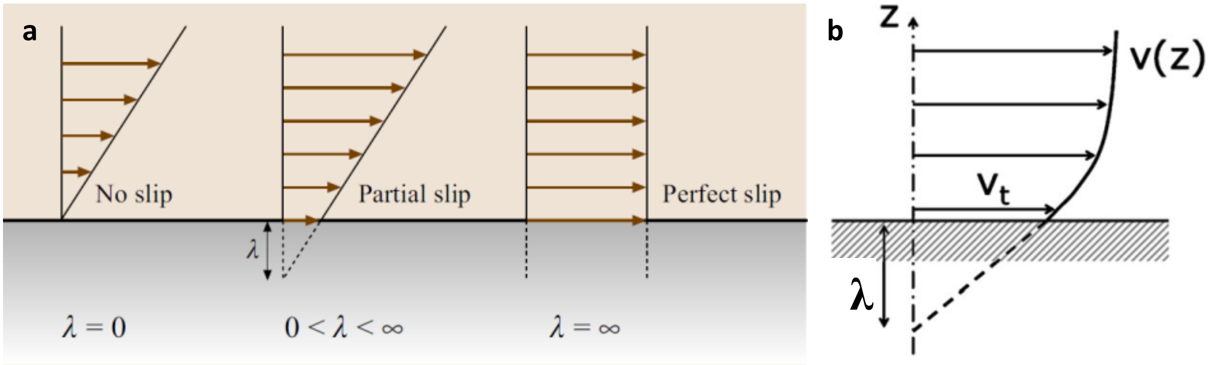

Figure 2.14 Slippage effects (a) *Interpretation of the slip. Reproduced with permission from ref[77].Copyright 2007, Springer Nature.* ***(b)*** *Schematic representation of the definition of the slip length λ. Reproduced from ref[78]. Copyright 2007, Royal Society of Chemistry*

The slip length of water at the solid surface depends on the wettability of the surface. Slip lengths in the range of tens of nanometres are usually seen at hydrophobic surfaces; whereas, it is in the sub-nanometres scale for hydrophilic surfaces[40, 78]. In GO membranes, water flows through the interconnected graphene capillaries. As the capillary walls are purely hydrophobic by nature, water molecules experience reduced friction with the wall, which results in the correlated single file movement as evident from the enhanced water flow. When the effect of water slippage at hydrophobic graphene capillaries are taken into account in the HP equation, the measured water flux matches quite well with the theory and the estimated slip length λ are ≈ 10-100 nm, in conjunction with the behaviour observed for the correlated water flow in carbon nanotubes

2.4.3.4 Precise ionic sieving

Due to the presence of oxygen containing functional groups on the GO sheets, the interlayer space of GO membrane is ~6−10 Å under dry conditions, which is larger than interlayer space of graphite (3.4 Å). When GO membranes are immersed in water or any ionic solutions, hydrophilic oxygen-containing groups, including hydroxyl, carboxyl and epoxy absorb water molecules into the inter-layer gallery, which leads to an expansion of the GO's interlayer spacing to~ 13-14 Å[54]. The hydration of GO capillaries by the absorption of water molecules is known as swelling. The effective free space in the interlayer galleries increases to 9 Å for the permeation of ions and molecules when the space occupied by the carbon atoms in the swelled state is accounted.

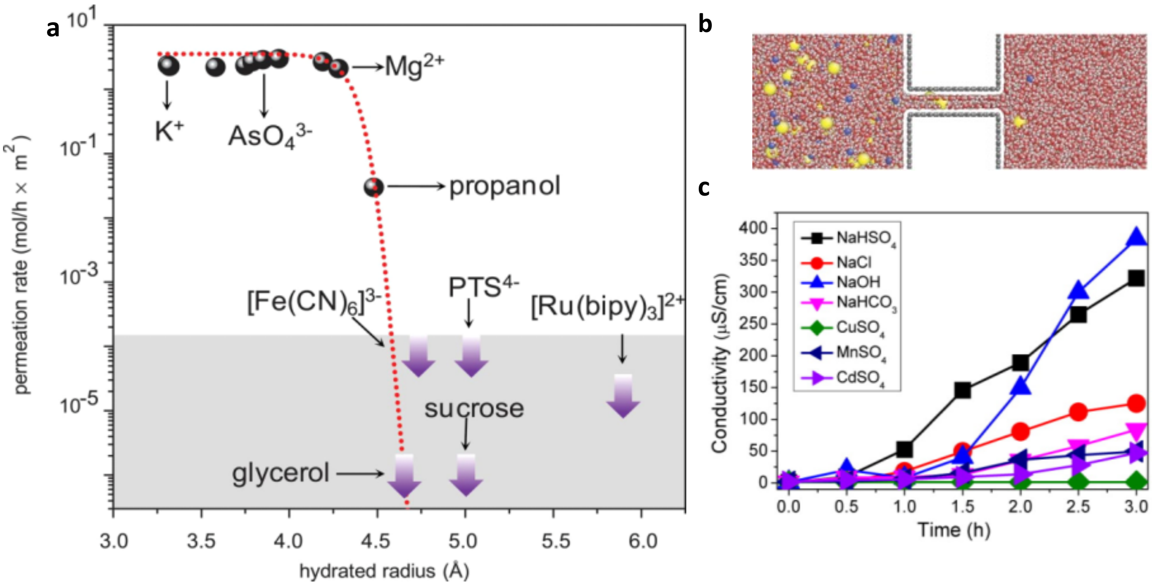

Figure 2.15 Graphene oxide membrane as molecular sieve. (a) Permeation rates of various molecules and ions of different size through a 5 µm thick GO membrane showing a sharp sieving cut-off at 4.5 Å, demonstrating GO as a physical sieve. ***(b)*** Snapshot of NaCl diffusion through a 9 Å graphene capillary allowing two layers of water. Reproduced with permission from ref[54]. Copyright 2014, the American Association for the Advancement of Science [54]. ***(c)*** Conductivity of the permeated salt solution with time through GO membranes showing the difference in the ion interaction. Reproduced from ref [57]. Copyright 2014, American Chemical Society.

Any ions or molecules having a hydrated radius of 4.5 Å or less can enter and permeate through the channel and bigger ions are fully blocked (Figure 2.15), thus behaving like a physical sieve[54, 79]. Furthermore, the ion permeation rates were found to be around 1000 times faster than predicted by the simple diffusion model, which could be related to the capillary-like pressures acting on ions inside GO nanocapillaries. The sharp size cut-off and precise sieving of ions demonstrated by GO membranes is very much appealing as it has enormous potentials in size based separation applications such as desalination and water filtration.

2.4.3.5 Ion exclusion mechanism

The potential application of graphene oxide membranes for ion separation and filtration applications were demonstrated first by Sun *et al.*[57]. A series of ion- permeation experiments of metallic salt solution using a conductivity meter has shown that the permeation rate of ions follows the order $Na^+ > Mn^{2+} > Cd^{2+}$, but variation of ion size shows a different trend $Mn^{2+} > Cd^{2+} > Cu^{2+} > Na^+$ which clearly demonstrates that the ion sieving is not a geometric effect, ruling out the size exclusion theory. The degree of ion interaction with sp^3 and sp^2 sites of GO membrane is different for alkali, alkaline-earth and transition metal cations. In the case of transition metal cations, the ions prefer to interact with the sp^3 C–O matrix through coordination interactions. In contrast, alkali and alkaline-earth cations prefer to interact with the sp^2 domains within the GO sheets facilitated through "cation-π" interactions. The difference in the degree of electrostatic interaction between the ion and GO surface results in the selective permeation of alkali/alkaline earth cations over transition metal cations.

Another mechanism for the selective passage of ions is physical size sieving as discussed in precise ionic sieving session (section 2.4.3.4).

Dehydration defined ion selectivity in sub-nm pores is a recently proposed mechanism for the ion exclusion in GO membranes[56, 80]. Angstrom scale channels in GO membranes were fabricated by physical confinement. Where, although the channel size is smaller than the typical ion size, ions still pass through the membrane, albeit with reduced speed, violating the size exclusion theory. This can be explained by a simple mechanism called dehydration. When a salt is dissolved in water, the water molecules will stabilize the ion by forming a water baggage containing concentric shells of water molecules. When the channel size is less than the ion size, for the ions to get into the capillary, it needs to remove some of its excess baggage, which requires a substantial amount of energy[81]. The extent of ion dehydration is different for different ions which depend on a parameter called hydration energy of ions. As the charge of the ion increases, electrostatic attraction between the ion and water molecules also increases and is reflected in the magnitude of their hydration free energies, which increases in the order
$K^+ < Na^+ < Li^+ < Ca^{2+} < Mg^{2+}$. Due to the higher hydration energy, Mg^{2+} ions are expected to have a strongly bound water shell which results largest barriers for permeation and slowest permeation rates. On the other hand, ions with less strongly bound shells (K^+ and Na^+) can enter into the channel by reconfiguring their water shells.

2.4.3.6 Tunable interlayer spacing

Controlling the inter-layer spacing of GO below 10 Å has proved to be challenging because of the swelling of GO capillaries. Various chemical/physical approaches have been reported to restrict the swelling of GO capillaries. The physical approaches reported so far include, assembling GO sheets with nanoscale wrinkles [4, 82], focussed laser beams[83, 84], thermal reduction[59], controlling the lateral size of GO sheets[85, 86], varying the thickness of GO[56, 87] and constructing epoxy walls between GO membranes for physical confinement[56] etc. The various chemical approaches attempted include, inserting certain linker molecules between the GO sheets [52, 88-92] and chemical reduction[93, 94]. In spite of all the efforts, controlling the inter-layer spacing of GO membrane below 10 Å has proved to be challenging because of the swelling of graphene capillaries when contacted with water.

2.4.4 Applications of GO membranes

Utilizing the potential of GO membranes for desalination and water filtration applications has been a major area of research. The filtration performance and desalination efficiency of graphene oxide membranes can be examined by conducting forward osmosis (FO), and pressure assisted reverse osmosis (RO) experiments. The excellent sieving behaviour and resistance free permeation of water molecules is utilized in many areas from liquid/gas separation to salinity gradient power generation[4, 95, 96]. The GO membranes when soaked in water, behave like a tiny molecular sieve, filtering out ions and molecules with sizes greater than 9 Å. Sieving characteristics of GO membranes can be improved by different means such as layer by layer assembly and thermal treatment. The resulting membrane may find application in water treatment. M.Hu *et al.* fabricated a water separation membrane by layer-by-layer deposition of GO nanosheets on a polydopamine-coated polysulfone support and the sheets were cross linked by 1,3,5-benzenetricarbonyl trichloride[60]. This is the first report demonstrating the potential of GO for water treatment applications. Water flux and organic molecules/salt rejection performance was evaluated in a dead end filtration system. Despite low rejection of (6−46%) monovalent and divalent salts, the membrane exhibited 46-66 and 95% rejection for methylene blue Rhodamine-WT molecules. The water permeability of the membrane was reasonably high (between 80 and 276 LMH/ MPa), 4−10 times higher than that of most commercial nanofiltration membranes. Ultrafiltration nano-strand graphene oxide channels with a size distribution of 3-5nm showed a water flux, which is around 100 times higher than that of commercial membranes with a reasonably good rejection performances[52]. Very recently graphene- graphene oxide- composite membranes, prepared by vacuum filtration showed NaCl salt rejection of~ 95% in the FO experiments with a water flux, of ~ 3 Lm^{-2} h^{-1} which is comparable to commercial desalination membranes[56]. Another area, where graphene oxide membranes are greatly explored is for the gas separation applications. The micrometre thick graphene oxide membrane is impermeable to all the gases. But when the thickness is reduced to around few nanometres, selective separation of gaseous molecules occur through the structural defects originating from the imperfect coverage or interlocking of GO sheets, giving rise to selectivities as high as 3400 and 900 [59, 97] for H_2/CO_2 and H_2/N_2 mixtures, respectively. Apart from the liquid and gas separation, graphene oxide membranes are also used in electrochemical energy storage, such as batteries[98], fuel cells[99] and supercapacitors[100]. The voltage generation by making use of the ion selectivity of the GO membrane is also an attractive area of research, which is getting tremendous attention due to its potential in the renewable and environmentally friendly way to generate electric power, typically known as blue energy[95, 101, 102].

2.4.5 Current Challenges

Good water permeability, water-ion selectivity, mechanical stability of the membrane under prolonged use and good fouling resistance are the ideal characteristics of a commercially viable membrane. The ultimate goal of graphene oxide membrane research is to develop a filtration unit which can produce potable water from waste water and seawater at a minimal energy cost. For making full use of the ultrafast permeation and precise sieving properties in desalination and water filtration applications, size of the graphene capillaries in GO membrane should not exceed 6-7 Å. A number of efforts have been made recently to control the interlayer spacing below sub nanometre by incorporating foreign molecules in the interlayer gallery of GO membranes and thermal annealing. But precise control of interlayer spacing in wet state has proved to be a major challenge. Another big challenge facing now is the industrial scalability of the membranes. Durability and stability of the membrane under prolonged contact with salty water and the fouling through bacteria or any other organic matter is another major concern when GO membranes are employed in desalination and water filtration[81]. Overall, the research on desalination membranes is mostly focussed on enhancing the water flux rather than improving the ion selectivity of the membranes. The modelling results shows that enhanced water permeability above the currently achievable rates (2–3

$\mathrm{lm^{-2}h^{-1}bar^{-1}}$[103, 104]) would not ensure a reduction in energy requirements. Instead of focussing more on improving the water permeability of the membrane, an effective strategy is to improve the water-ion selectivity of the membrane which will further increase the efficiency of desalination[56, 103].

2.5 References

1. Bunch, J. S.; Verbridge, S. S.; Alden, J. S.; van der Zande, A. M.; Parpia, J. M.; Craighead, H. G.; McEuen, P. L. *Nano Lett.* **2008,** 8, (8), 2458-2462.

2. Berry, V. *Carbon* **2013,** 62, (Supplement C), 1-10.

3. Hu, S.; Lozada-Hidalgo, M.; Wang, F. C.; Mishchenko, A.; Schedin, F.; Nair, R. R.; Hill, E. W.; Boukhvalov, D. W.; Katsnelson, M. I.; Dryfe, R. A. W.; Grigorieva, I. V.; Wu, H. A.; Geim, A. K. *Nature* **2014,** 516, 227.

4. Liu, G.; Jin, W.; Xu, N. *Chem. Soc. Rev.* **2015,** 44, (15), 5016-5030.

5. Sint, K.; Wang, B.; Král, P. *J. Am. Chem. Soc.* **2008,** 130, (49), 16448-16449.

6. Suk, M. E.; Aluru, N. R. *J. Phys. Chem. Lett.* **2010,** 1, (10), 1590-1594.

7. Cohen-Tanugi, D.; Grossman, J. C. *Nano Lett.* **2012,** 12, (7), 3602-3608.

8. Jiang, D.-e.; Cooper, V. R.; Dai, S. *Nano Lett.* **2009,** 9, (12), 4019-4024.

9. Lozada-Hidalgo, M.; Hu, S.; Marshall, O.; Mishchenko, A.; Grigorenko, A. N.; Dryfe, R. A. W.; Radha, B.; Grigorieva, I. V.; Geim, A. K. *Science* **2016,** 351, (6268), 68.

10. Wanunu, M. *Phys. Life Rev.* **2012,** 9, (2), 125-158.

11. Branton, D.; Deamer, D. W.; Marziali, A.; Bayley, H.; Benner, S. A.; Butler, T.; Di Ventra, M.; Garaj, S.; Hibbs, A.; Huang, X.; Jovanovich, S. B.; Krstic, P. S.; Lindsay, S.; Ling, X. S.; Mastrangelo, C. H.; Meller, A.; Oliver, J. S.; Pershin, Y. V.; Ramsey, J. M.; Riehn, R.; Soni, G. V.; Tabard-Cossa, V.; Wanunu, M.; Wiggin, M.; Schloss, J. A. *Nat. Biotechnol.* **2008,** 26, 1146.

12. Dekker, C. *Nat. Nanotechnol.* **2007,** 2, 209.

13. Garaj, S.; Liu, S.; Golovchenko, J. A.; Branton, D. *Proc. Natl. Acad. Sci. U.S.A.* **2013,** 110, (30), 12192-12196.

14. Merchant, C. A.; Healy, K.; Wanunu, M.; Ray, V.; Peterman, N.; Bartel, J.; Fischbein, M. D.; Venta, K.; Luo, Z.; Johnson, A. T. C.; Drndić, M. *Nano Lett.* **2010,** 10, (8), 2915-2921.

15. Schneider, G. F.; Kowalczyk, S. W.; Calado, V. E.; Pandraud, G.; Zandbergen, H. W.; Vandersypen, L. M. K.; Dekker, C. *Nano Lett.* **2010,** 10, (8), 3163-3167.

16. Cheng, Y. C.; Kaloni, T. P.; Zhu, Z. Y.; Schwingenschlögl, U. *Appl. Phys. Lett.* **2012,** 101, (7), 073110.

17. Wu, S.; Yang, R.; Shi, D.; Zhang, G. *Nanoscale* **2012,** 4, (6), 2005-2009.

18. Liu, L.; Ryu, S.; Tomasik, M. R.; Stolyarova, E.; Jung, N.; Hybertsen, M. S.; Steigerwald, M. L.; Brus, L. E.; Flynn, G. W. *Nano Lett.* **2008,** 8, (7), 1965-1970.

19. Koenig, S. P.; Wang, L.; Pellegrino, J.; Bunch, J. S. *Nat. Nanotechnol.* **2012,** 7, 728.

20. Hahn, J. R.; Kang, H.; Lee, S. M.; Lee, Y. H. *J. Phys. Chem. B* **1999,** 103, (45), 9944-9951.

21. Yang, R. T.; Wong, C. *J. Chem. Phys.* **1981,** 75, (9), 4471-4476.

22. Hahn, J. R.; Kang, H. *Surf. Sci.* **2000,** 446, (1), L77-L82.

23. Russo, C. J.; Golovchenko, J. A. *Proc. Natl. Acad. Sci. U. S. A.* **2012,** 109, (16), 5953-5957.

24. Fischbein, M. D.; Drndić, M. *Appl. Phys. Lett.* **2008,** 93, (11), 113107.

25. O'Hern, S. C.; Boutilier, M. S. H.; Idrobo, J.-C.; Song, Y.; Kong, J.; Laoui, T.; Atieh, M.; Karnik, R. *Nano Lett.* **2014,** 14, (3), 1234-1241.

26. Surwade, S. P.; Smirnov, S. N.; Vlassiouk, I. V.; Unocic, R. R.; Veith, G. M.; Dai, S.; Mahurin, S. M. *Nat. Nanotechnol.* **2015,** 10, 459.

27. O'Hern, S. C.; Stewart, C. A.; Boutilier, M. S. H.; Idrobo, J.-C.; Bhaviripudi, S.; Das, S. K.; Kong, J.; Laoui, T.; Atieh, M.; Karnik, R. *ACS Nano* **2012,** 6, (11), 10130-10138.

28. Boutilier, M. S. H.; Sun, C.; O'Hern, S. C.; Au, H.; Hadjiconstantinou, N. G.; Karnik, R. *ACS Nano* **2014,** 8, (1), 841-849.

29. O'Hern, S. C.; Jang, D.; Bose, S.; Idrobo, J.-C.; Song, Y.; Laoui, T.; Kong, J.; Karnik, R. *Nano Lett.* **2015,** 15, (5), 3254-3260.

30. Eijkel, J. C. T.; Berg, A. v. d. *Microfluidics and Nanofluidics* **2005,** 1, (3), 249-267.

31. Schoch, R. B.; Han, J.; Renaud, P. *Rev. Mod. Phys.* **2008,** 80, (3), 839-883.

32. Howorka, S.; Siwy, Z. *Chem. Soc. Rev.* **2009,** 38, (8), 2360-2384.

33. Duan, C.; Wang, W.; Xie, Q. *Biomicrofluidics* **2013,** 7, (2), 026501.

34. Li, D., *Encyclopedia of microfluidics and nanofluidics*. Springer Science & Business Media: 2008.

35. Tagliazucchi, M.; Szleifer, I., *Chemically Modified Nanopores and Nanochannels*. William Andrew: 2016.

36. Mijatovic, D.; Eijkel, J. C. T.; van den Berg, A. *Lab Chip* **2005,** 5, (5), 492-500.

37. Radha, B.; Esfandiar, A.; Wang, F. C.; Rooney, A. P.; Gopinadhan, K.; Keerthi, A.; Mishchenko, A.; Janardanan, A.; Blake, P.; Fumagalli, L.; Lozada-Hidalgo, M.; Garaj, S.; Haigh, S. J.; Grigorieva, I. V.; Wu, H. A.; Geim, A. K. *Nature* **2016,** 538, 222.

38. Israelachvili, J. N., *Intermolecular and surface forces*. Academic press: 2011.

39. Mate, C. M. *IEEE Trans. Magn.* **2011,** 47, (1), 124-130.

40. Gravelle, S.; Ybert, C.; Bocquet, L.; Joly, L. *Physical Review E* **2016,** 93, (3), 033123.

41. Xie, Q.; Alibakhshi, M. A.; Jiao, S.; Xu, Z.; Hempel, M.; Kong, J.; Park, H. G.; Duan, C. *Nat. Nanotechnol.* **2018**.

42. Xie, Q.; Xin, F.; Park, H. G.; Duan, C. *Nanoscale* **2016,** 8, (47), 19527-19535.

43. Esfandiar, A.; Radha, B.; Wang, F. C.; Yang, Q.; Hu, S.; Garaj, S.; Nair, R. R.; Geim, A. K.; Gopinadhan, K. *Science* **2017,** 358, (6362), 511.

44. Zhu, Y.; Murali, S.; Cai, W.; Li, X.; Suk, J. W.; Potts, J. R.; Ruoff, R. S. *Adv. Mater.* **2010,** 22, (35), 3906-3924.

45. Dreyer, D. R.; Park, S.; Bielawski, C. W.; Ruoff, R. S. *Chem. Soc. Rev.* **2010,** 39, (1), 228-240.

46. Gómez-Navarro, C.; Meyer, J. C.; Sundaram, R. S.; Chuvilin, A.; Kurasch, S.; Burghard, M.; Kern, K.; Kaiser, U. *Nano Lett.* **2010,** 10, (4), 1144-1148.

47. Dreyer, D. R.; Todd, A. D.; Bielawski, C. W. *Chem. Soc. Rev.* **2014,** 43, (15), 5288-5301.

48. Dikin, D. A.; Stankovich, S.; Zimney, E. J.; Piner, R. D.; Dommett, G. H. B.; Evmenenko, G.; Nguyen, S. T.; Ruoff, R. S. *Nature* **2007,** 448, 457.

49. Chua, C. K.; Pumera, M. *Chem. Soc. Rev.* **2014,** 43, (1), 291-312.

50. Huang, H.; Ying, Y.; Peng, X. *J. Mater. Chem. A* **2014,** 2, (34), 13772-13782.

51. Huang, H.; Mao, Y.; Ying, Y.; Liu, Y.; Sun, L.; Peng, X. *Chem. Commun.* **2013,** 49, (53), 5963-5965.

52. Huang, H.; Song, Z.; Wei, N.; Shi, L.; Mao, Y.; Ying, Y.; Sun, L.; Xu, Z.; Peng, X. *Nat. Commun.* **2013,** 4, 2979.

53. Nair, R. R.; Wu, H. A.; Jayaram, P. N.; Grigorieva, I. V.; Geim, A. K. *Science* **2012,** 335, (6067), 442.

54. Joshi, R. K.; Carbone, P.; Wang, F. C.; Kravets, V. G.; Su, Y.; Grigorieva, I. V.; Wu, H. A.; Geim, A. K.; Nair, R. R. *Science* **2014,** 343, (6172), 752.

55. Yang, Q.; Su, Y.; Chi, C.; Cherian, C. T.; Huang, K.; Kravets, V. G.; Wang, F. C.; Zhang, J. C.; Pratt, A.; Grigorenko, A. N.; Guinea, F.; Geim, A. K.; Nair, R. R. *Nat. Mater.* **2017,** 16, 1198.

56. Abraham, J.; Vasu, K. S.; Williams, C. D.; Gopinadhan, K.; Su, Y.; Cherian, C. T.; Dix, J.; Prestat, E.; Haigh, S. J.; Grigorieva, I. V.; Carbone, P.; Geim, A. K.; Nair, R. R. *Nat. Nanotechnol.* **2017,** 12, 546.

57. Sun, P.; Zhu, M.; Wang, K.; Zhong, M.; Wei, J.; Wu, D.; Xu, Z.; Zhu, H. *ACS Nano* **2013,** 7, (1), 428-437.

58. Tsou, C.-H.; An, Q.-F.; Lo, S.-C.; De Guzman, M.; Hung, W.-S.; Hu, C.-C.; Lee, K.-R.; Lai, J.-Y. *J. Membr. Sci.* **2015,** 477, 93-100.

59. Kim, H. W.; Yoon, H. W.; Yoon, S.-M.; Yoo, B. M.; Ahn, B. K.; Cho, Y. H.; Shin, H. J.; Yang, H.; Paik, U.; Kwon, S.; Choi, J.-Y.; Park, H. B. *Science* **2013,** 342, (6154), 91.

60. Hu, M.; Mi, B. *Environ. Sci. Technol.* **2013,** 47, (8), 3715-3723.

61. Akbari, A.; Sheath, P.; Martin, S. T.; Shinde, D. B.; Shaibani, M.; Banerjee, P. C.; Tkacz, R.; Bhattacharyya, D.; Majumder, M. *Nat. Commun.* **2016,** 7, 10891.

62. Becerril, H. A.; Mao, J.; Liu, Z.; Stoltenberg, R. M.; Bao, Z.; Chen, Y. *ACS Nano* **2008,** 2, (3), 463-470.

63. Pham, V. H.; Cuong, T. V.; Hur, S. H.; Shin, E. W.; Kim, J. S.; Chung, J. S.; Kim, E. J. *Carbon* **2010,** 48, (7), 1945-1951.

64. Oliveira Jr, O. N. *Braz J Phys* **1992,** 22, (2), 60-69.

65. Xu, C.; Wu, X.; Zhu, J.; Wang, X. *Carbon* **2008,** 46, (2), 386-389.

66. Wang, X.; Bai, H.; Shi, G. *J. Am. Chem. Soc.* **2011,** 133, (16), 6338-6342.

67. Richardson, J. J.; Cui, J.; Björnmalm, M.; Braunger, J. A.; Ejima, H.; Caruso, F. *Chem. Rev.* **2016,** 116, (23), 14828-14867.

68. Raidongia, K.; Huang, J. *J. Am. Chem. Soc.* **2012,** 134, (40), 16528-16531.

69. Qiu, L.; Zhang, X.; Yang, W.; Wang, Y.; Simon, G. P.; Li, D. *Chem. Commun.* **2011,** 47, (20), 5810-5812.

70. Eda, G.; Chhowalla, M. *Adv. Mater.* **2010,** 22, (22), 2392-2415.

71. Zangi, R.; Mark, A. E. *Phys. Rev. Lett.* **2003,** 91, (2), 025502.

72. Giovambattista, N.; Rossky, P. J.; Debenedetti, P. G. *Phys. Rev. Lett.* **2009,** 102, (5), 050603.

73. Majumder, M.; Chopra, N.; Andrews, R.; Hinds, B. J. *Nature* **2005,** 438, 44.

74. Peng, X.; Jin, J.; Nakamura, Y.; Ohno, T.; Ichinose, I. *Nat. Nanotechnol.* **2009,** 4, 353.

75. Qin, X.; Yuan, Q.; Zhao, Y.; Xie, S.; Liu, Z. *Nano Lett.* **2011,** 11, (5), 2173-2177.

76. Whitby, M.; Quirke, N. *Nat. Nanotechnol.* **2007,** 2, 87.

77. Lauga, E.; Brenner, M.; Stone, H., Microfluidics: The No-Slip Boundary Condition. In *Springer Handbook of Experimental Fluid Mechanics*, Tropea, C.; Yarin, A. L.; Foss, J. F., Eds. Springer Berlin Heidelberg: Berlin, Heidelberg, 2007; pp 1219-1240.

78. Bocquet, L.; Barrat, J.-L. *Soft Matter* **2007,** 3, (6), 685-693.

79. Mi, B. *Science* **2014,** 343, (6172), 740.

80. Sahu, S.; Di Ventra, M.; Zwolak, M. *Nano Lett.* **2017,** 17, (8), 4719-4724.

81. Devanathan, R. *Nat. Nanotechnol.* **2017,** 12, 500.

82. Yang, T.; Lin, H.; Zheng, X.; Loh, K. P.; Jia, B. *J. Mater. Chem. A* **2017,** 5, (32), 16537-16558.

83. Zhang, Y.-L.; Chen, Q.-D.; Xia, H.; Sun, H.-B. *Nano Today* **2010,** 5, (5), 435-448.

84. Zhou, Y.; Bao, Q.; Varghese, B.; Tang, L. A. L.; Tan, C. K.; Sow, C.-H.; Loh, K. P. *Adv. Mater.* **2010,** 22, (1), 67-71.

85. Sun, P.; Wang, K.; Wei, J.; Zhong, M.; Wu, D.; Zhu, H. *J. Mater. Chem. A* **2014,** 2, (21), 7734-7737.

86. Sun, P.; Zheng, F.; Zhu, M.; Song, Z.; Wang, K.; Zhong, M.; Wu, D.; Little, R. B.; Xu, Z.; Zhu, H. *ACS Nano* **2014,** 8, (1), 850-859.

87. Coleman, M.; Tang, X. *Nano Res.* **2015,** 8, (4), 1128-1138.

88. Wang, W.; Eftekhari, E.; Zhu, G.; Zhang, X.; Yan, Z.; Li, Q. *Chem. Commun.* **2014,** 50, (86), 13089-13092.

89. Park, S.; Lee, K.-S.; Bozoklu, G.; Cai, W.; Nguyen, S. T.; Ruoff, R. S. *ACS Nano* **2008,** 2, (3), 572-578.

90. An, Z.; Compton, O. C.; Putz, K. W.; Brinson, L. C.; Nguyen, S. T. *Adv. Mater.* **2011,** 23, (33), 3842-3846.

91. Cheng, Q.; Wu, M.; Li, M.; Jiang, L.; Tang, Z. *Angew. Chem. Int. Ed.* **2013,** 52, (13), 3750-3755.

92. Stankovich, S.; Dikin, D. A.; Compton, O. C.; Dommett, G. H. B.; Ruoff, R. S.; Nguyen, S. T. *Chem. Mater.* **2010,** 22, (14), 4153-4157.

93. Liu, H.; Wang, H.; Zhang, X. *Adv. Mater.* **2015,** 27, (2), 249-254.

94. Su, Y.; Kravets, V. G.; Wong, S. L.; Waters, J.; Geim, A. K.; Nair, R. R. *Nat. Commun.* **2014,** 5, 4843.

95. Ji, J.; Kang, Q.; Zhou, Y.; Feng, Y.; Chen, X.; Yuan, J.; Guo, W.; Wei, Y.; Jiang, L. *Adv. Funct. Mater.* **2017,** 27, (2), 1603623.

96. Gao, J.; Feng, Y.; Guo, W.; Jiang, L. *Chem. Soc. Rev.* **2017,** 46, (17), 5400-5424.

97. Li, H.; Song, Z.; Zhang, X.; Huang, Y.; Li, S.; Mao, Y.; Ploehn, H. J.; Bao, Y.; Yu, M. *Science* **2013,** 342, (6154), 95.

98. Huang, J.-Q.; Zhuang, T.-Z.; Zhang, Q.; Peng, H.-J.; Chen, C.-M.; Wei, F. *ACS Nano* **2015,** 9, (3), 3002-3011.

99. Hatakeyama, K.; Tateishi, H.; Taniguchi, T.; Koinuma, M.; Kida, T.; Hayami, S.; Yokoi, H.; Matsumoto, Y. *Chem. Mater.* **2014,** 26, (19), 5598-5604.

100. Han, S.; Wu, D.; Li, S.; Zhang, F.; Feng, X. *Adv. Mater.* **2014,** 26, (6), 849-864.

101. Siria, A.; Bocquet, M.-L.; Bocquet, L. *Nat Rev Chem* **2017,** 1, 0091.

102. Sun, P.; Zheng, F.; Zhu, M.; Wang, K.; Zhong, M.; Wu, D.; Zhu, H. *Sci. Rep.* **2014,** 4, 5528.

103. Werber, J. R.; Osuji, C. O.; Elimelech, M. *Nat Rev Mater* **2016,** 1, 16018.

104. Cohen-Tanugi, D.; McGovern, R. K.; Dave, S. H.; Lienhard, J. H.; Grossman, J. C. *Energy Environ. Sci.* **2014,** 7, (3), 1134-1141.

Blank Page

Chapter 3-Characterization Techniques and Methodology

Blank Page

3.1 Introduction

The scope of this chapter is to provide a brief overview of the main characterization techniques and the methodology adopted in this entire study. The first section provides a brief description of the research methodology and the material synthesis including graphene oxide synthesis, membrane fabrication, and water/ion permeation through physically confined GO (PCGO) membranes. The second phase of this chapter describes the physical characterization techniques used in the study. A brief outline of the working principle of the experimental tools such as X-ray diffraction (XRD), scanning electron microscopy (SEM) and transmission electron microscopy (TEM) for the imaging and structure determination purposes are also summarized. The ion permeation behaviour was analysed using spectroscopic and chromatographic techniques such as ICP-AES (Inductively coupled plasma-atomic emission spectrometry) and IC (Ion chromatography).

3.2 GO membrane synthesis and PCGO membrane fabrication

3.2.1 Material Synthesis

The graphene oxide suspension was prepared by a modified Hummers method[1-3]. In a typical procedure, millimetre sized flakes of graphite (1 g) and sodium nitrate (0.5 g) were dispersed in concentrated sulphuric acid (24 ml). The dispersion was cooled down using an ice bath and potassium permanganate (3 g) was added over period of 3 hours keeping the temperature below 10 °C. The mixture was stirred for an additional 16 h and the reaction temperature was kept in the same temperature range. Diluted sulphuric acid (20ml, 10%) was added drop wise over a period of 2 h keeping the temperature below 10 °C. Followed by this; 60ml water was added and stirred continuously. Hydrogen peroxide (20ml, 3%) was added and kept under stirring for more time. The graphite oxide slurry was then washed several times until the pH of the supernatant became neutral .The obtained graphite oxide was dispersed in water by sonication to make graphene oxide crystallites. The thicker flakes were removed by centrifugation at 8000 rpm for several times. The GO membrane was prepared by vacuum filtration of the resulting supernatant GO suspension through an alumina anodisc membrane (AAO, 200 nm pore size and a diameter of 47 mm purchased from Merck Millipore). GO membranes with a wide range of thicknesses can be prepared by varying the volume and concentration of the GO

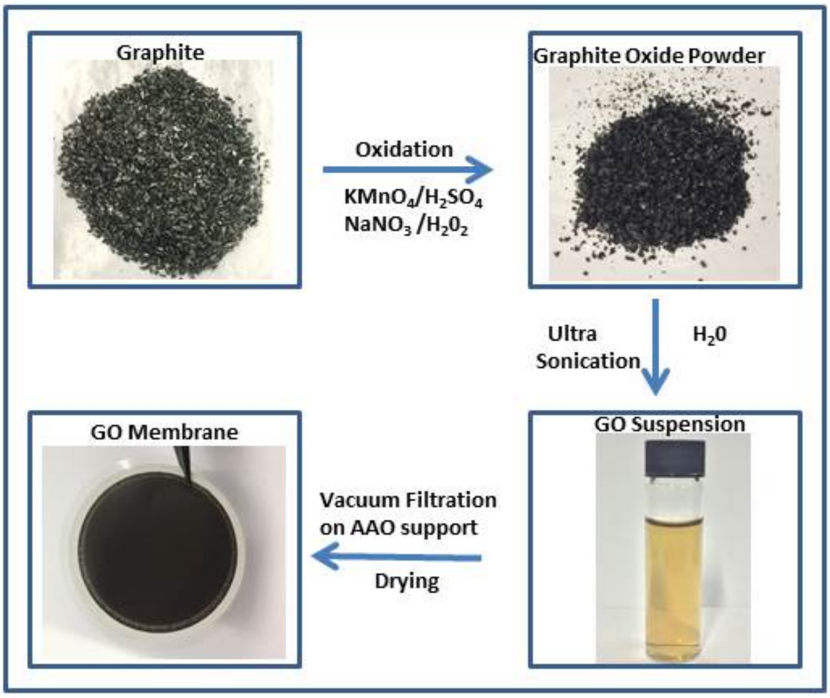

Figure 3.1 Preparation of Graphene Oxide membranes

suspension in the filtration assembly and the typical thickness of the membrane prepared in the present study is~80-100 µm. The as prepared membrane was dried inside a vacuum oven for 10 h at 45 degree to remove the excess water inside the membrane.

3.2.2 Tuning interlayer spacing of GO membranes

The GO membrane is very hygro-responsive [4-6]; the interlayer spacing of GO varies with humidity and we used this property to tune the interlayer spacing of GO membranes. For tuning the interlayer spacing, GO membranes prepared by vacuum filtration were cut into rectangular strips of dimension 4 mm× 10 mm. It is well known that saturated salt solution provides a stable spectrum of relative humidity (RH) values as the vapor-liquid and solid phases gives an independent water vapour pressure and can't alter the moisture content present in the system with time[7, 8]. GO membranes with correspoding interlayer spacing were prepared by storing the rectangular strips inside a closed container with differrent relative humidities inside. The salt solutions used and the corresponding humidities is gven in table 3.1

Salt Used	Humidity (a.u)
LiCl	12%
MgCl2	33%
$Mg(NO_3)_2$	55%
NaCl	75%
KCl	84%

Table 3.1 Saturated salt solutions used and the corresponding humidity's

Saturated salt solutions were prepared by wetting excess amounts of salt with distilled water and poured into the bottom of a plastic container. The freshly cut rectangular strips of GO membranes were kept inside a small mesh made of PTFE, without any contact with the bottom salt solution. A humidity meter was also used to verify that the salt is fully saturated and gave the reported values of RH[7]. The zero humidity condition was created by keeping the rectangular GO strips inside a glove box filled with Ar. RH-100% was achieved by keeping the GO membrane inside plastic container filled with water vapour.

3.2.3 Fabrication procedure of PCGO membrane

After adjusting the interlayer spacing of GO membranes, each rectangular strip was glued together and stacked vertically using two component 1266 stycast epoxy resin, mixed by a weight percentage ratio of 3.5:1.

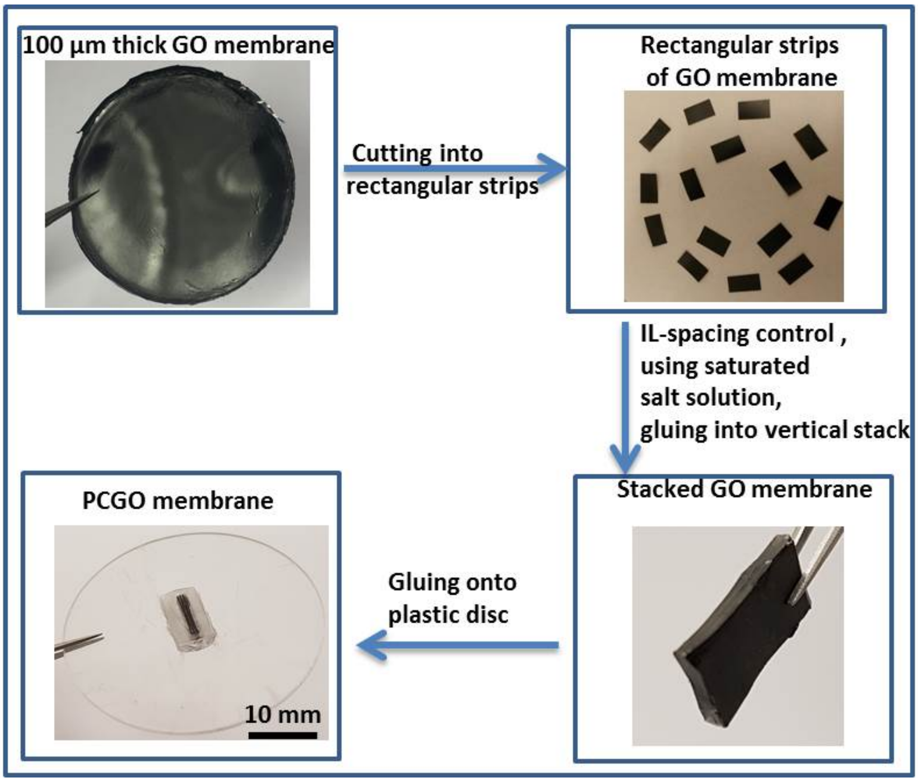

Figure 3.2 Fabrication procedure of PCGO membrane

For curing of the epoxy resin, the glued stack was transferred into the same humidity environment where the laminates were initially kept for adjusting the interlayer spacing. The resulting vertical stack of GO membrane was finally glued onto a slot made of either plastic/ copper disc with a rectangular slot in the middle. The possible coverage of the epoxy resin at the top and bottom cross sectional surface was carefully trimmed off so that all the nanochannels are completely open for the permeation experiments. The same is verified using an optical microscope as well and the cleaved cross sectional surface was free from any epoxy residues.

3.3 Diffusion and water permeability test through PCGO membrane

3.3.1 Experimental set up for permeation experiments

All the diffusion experiments were performed using a custom designed set up made from Teflon, which consist of two compartments, feed and permeate (Figure 3.3). The PCGO membrane contained plastic disc was clamped between two O-rings between feed and permeate side to provide a leak tight environment for the permeation tests. In the permeation experiments, each compartment was filled with an equal volume (10 ml) of salt solution (feed side) and deionized water (permeate side) respectively to avoid a hydrostatic pressure difference due to the asymmetry in the liquid column height.

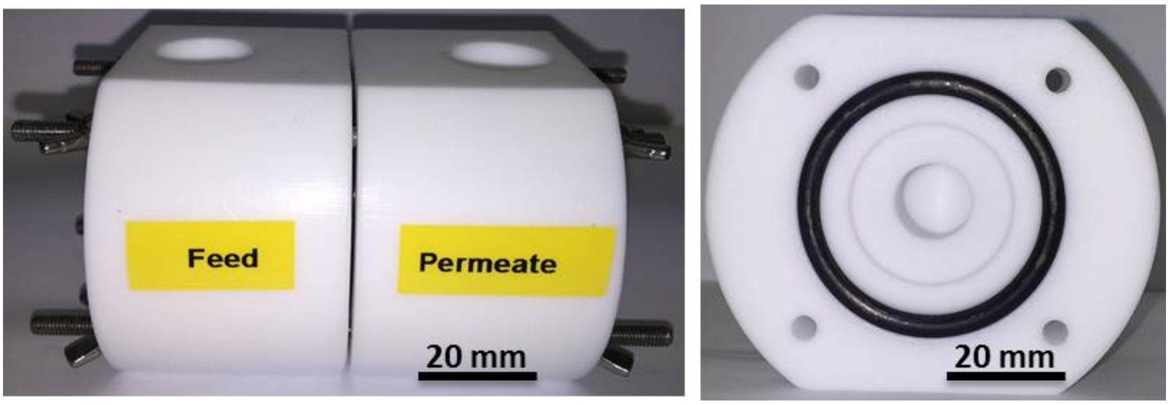

Figure 3.3 Experimental set for permeation experiments and its cross sectional view

The salt solutions we used in our permeation experiments were KCl, NaCl, LiCl, $CaCl_2$ and $MgCl_2$ respectively. Salt permeation across the PCGO membranes is mainly driven by the concentration gradient across the membrane and the quantitative estimation of the permeated salt was analysed using different analytical techniques such as inductively coupled plasma-atomic emission spectrometry (ICP-AES) and ion chromatography (IC) respectively.

3.3.2 Ion permeation studies through PCGO membranes

Ion diffusion through PCGO membranes with different interlayer spacing was performed using the Teflon made set up following the experimental procedure as described in section3.3.1. In a typical experiment, the feed side was filled with 1M salt solution and the permeate side with deionized water. Stirring was done on both sides to avoid concentration polarization effects. The ion permeation through epoxy encapsulated PCGO membranes was monitored as a function of concentration gradient and time; normally for 20-25 hour. After 25 hour, the permeated salt solution was collected from the permeate side and the quantitative estimation of the permeated ions was done using chemical analysis (ICP/IC analysis). The slope of the permeation vs time graph provides the permeation rates. Diffusion experiments were done for all the capillary sizes ranging from 6.4 to 9.8 Å for 5 different salts such as KCl, NaCl, LiCl, $CaCl_2$ and $MgCl_2$. Using the known volume of the permeate the number of ions permeated though the membrane was calculated and normalization with respect to time and area, giving the ion permeation rate.

The classical diffusion equation was used to compare the theoretically expected value of the ion permeation to the experimentally observed value. For the classical diffusion equation, permeation rate *J* is given by

$$J = \mathrm{Diff} \times \Delta C \times A_{\mathrm{eff}} / L \qquad (1)$$

where ΔC is the concentration gradient across the membrane (1 M for for the diffusion experiments), A_{eff} is the total cross-sectional area of nanocapillaries (≈3–8 mm^2), L is the diffusion length through the PCGO membrane (≈3 mm). Diff is the diffusion coefficient for ions in water (typically, Diff $\sim 10^{-5}$ $cm^2\ s^{-1}$).

3.3.3 Tested solutes and their hydrated diameters

The hydration shell, in a more generic way the solvation shell represents a shell of solvent molecules that adhere or bind to the central charged ions when, salts are dissolved in polar solvents. On solvation, the solvent molecules stabilizes the central ions by forming concentric shell of water molecules (Figure 3.4), by which the salt is dissociated into free ionic species. If water is the solvent, it is known as a hydration shell. The ion-water interactions in the aqueous environment can be represented in terms of hydration shell with a formula $M^{z+}(H_2O)_n$, where n corresponds to the hydration number that is associated or adhered to the ion M^{z+}. Hence, the apparent ion size in aqueous phase is the hydrated radius (i.e., $M^{z+}(H_2O)_n$) instead of bare ionic radius(i.e., M^{z+}). On the basis of the experimental investigation of the cation-oxygen distance and electrostatic phenomena, the relative positioning of the water molecules around small cations such as K^+ or Ca^{2+} remains at a stable thickness, with the individual water molecules being exchanged continuously with those in the bulk solution. The ion interaction with the water molecules depends on the charge and crystallographic radius of the central ion.

.

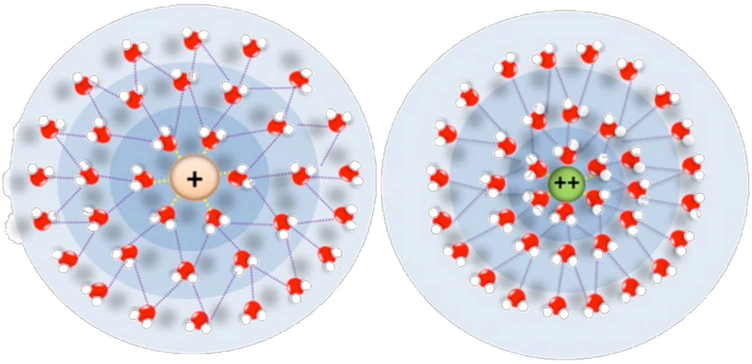

Tested ions	**Ionic Radius (Å)**	**Hydrated Radius (Å)**
K^+	1.52	3.3
Na^+	1.16	3.55
Li^+	0.9	3.8
Ca^{2+}	1.1	4.1
Mg^{2+}	0.72	4.25

Figure 3.4 Hydration shell and hydrated radius of ions. Schematic representation of the hydration shell of monovalent and divalent cations demonstrating their ordering and stability of hydration shell. Table on the right side shows the hydrated diameters of ions chosen in the study.

In the case of monovalent cations, for example, K^+, Na^+ and Li^+, the ionic radius varies in the order $K^+ > Na^+ > Li^+$ (Figure 3.4). As the size of K^+ ion is greater than both Na^+ and Li^+ ions, more number of water molecules will be adhered to its first hydration shell compared to other ions leading to increased water density in the first hydration shell with respect to successive water shells. Whereas, for Na^+ and Li^+ ions, due their reduced ion-size, the enhanced electrostatic interaction will bind more and more water molecules to the ions. The extent of water adherence to the primary hydration shell is limited by the size of the ions which leads to the formation of secondary and tertiary water shells where it was not that dominant in K^+ ion case. As a consequence of this, ion-volume in aqueous phase will be more for Li^+ ions compared to both Na^+ and Li^+ ions and is reflected in the magnitude of their hydrated radius which varies in the fashion $Li^+ > Na^+ > K^+$.

There is significant variation in the value of the hydrated diameter in the literature due to the difference in the value of the modelling parameters. The hydrated diameters considered here are chosen from the most cited values and were taken from reference[9, 10].

3.3.4 Temperature dependent ion permeation and activation energy.

Temperature dependent ion permeation experiments were carried out for a temperature range of 2-43 °C in a temperature controlled environmental chamber. The measurement set-up, KCl solution and deionized water were equilibrated at each temperature prior to the experiment. Magnetic stirring was used in both compartments to avoid concentration polarization effects. The same experimental protocol used in the permeation experiments was followed in the temperature studies as well. The ion permeation rate (P) in 4 different temperature ranges was measured using ICP. The temperature dependence of ion permeation is given by the Arrhenius equation [11-13]

$$P = P_0 exp\left(-\frac{E_A}{RT}\right) \tag{2}$$

where $P_0$is the pre-exponential factor, E_A is the activation energy,T is the temperature and R is the universal gas constant. To determine the activation energy $E_{A,}$ the natural logarithm of permeation rate was plotted against $\frac{1000}{T}$. From the slope of the curve, i.e. $\frac{E_A}{R}$, the activation energy for the entry of ions to the 2D capillaries is calculated.

3.3.5 Water flow through epoxy encapsulated GO membranes

Gravimetric measurements and pressure assisted water permeation experiments were carried out to understand the flow of water molecules through the constrained PCGO membranes. Stainless steel made container were used for the water permeation experiments. To provide a leak tight environment for the measurements, PCGO incorporated metal/plastic disc was sealed with two O-rings that clamp the disc from both sides. The schematic of the experimental set-up is shown in fig 3.5 (a). During the typical gravimetric measurements, weight loss of the stainless steel container filled with liquid water was monitored over time using a computer-controlled precision balance (Denver Instrument SI-203 with a sensitivity of 1 mg). All gravimetric measurements were conducted under an Ar atmosphere inside a glove box with a negligible water pressure ($<10^{-3}$ mbar). To measure the water permeation rate as a function of interlayer spacing; GO membranes with a channel size of 6.4, 7.4, 7.9, 8.6, 9.0 and 9.8 Å were fabricated following the physical confinement recipe.

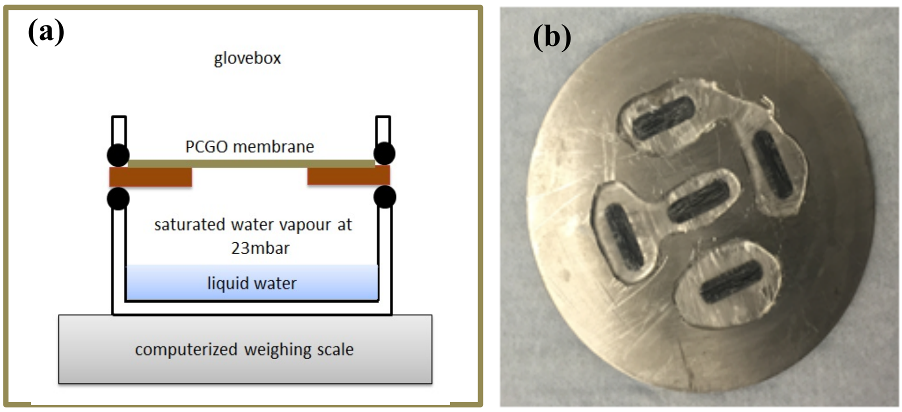

***Figure 3.5 Water flow through PCGO membranes**. (a) Schematic of water permeation measurement through PCGO membranes using gravimetric method inside a glove box environment. **(b)** Photograph of PCGO membrane with multiple stacks glued onto a stainless steel for the pressure filtration measurement*

The classical Hagen-Poiseuille equation was used to compare the experimentally observed water evaporation rate to the theoretically predicted value. For a classical incompressible Newtonian fluid, the mass flow through a slit geometry follows the HP equation,

$$Q = \frac{1}{12\eta}\frac{\Delta P}{L}\delta^{3}\,W\rho \qquad (3)$$

where η is the viscosity of water (1 mPa.s), ΔP is driving pressure, l is the permeation length (3 mm), δ is the effective pore size, W is the lateral width of nanochannels (9 mm) and ρ is the density of water. The water flux through the PCGO membranes can be calculated as $Q\times S$, where S is the area density of nano channels defined as $A/W\times d$, where A is the area and d is the interlayer distance. In addition to the gravimetric measurements, we also estimated the liquid water permeation through the PCGO membranes using dead end filtration experiments in a Sterlitech HP4750 stirred cell. The cross sectional area of the membrane is increased by gluing multiple stacks of GO membrane onto a stainless steel plate (Figure 3.5b) by which the effective water flow through the membrane could be increased.

3.4 Characterization Techniques

3.4.1 X-ray diffraction

3.4.1.1 Basics

X-ray diffraction is a non-destructive technique used for the identification of the crystalline nature of the sample and its unit cell parameters [14-16]. When a beam of monochromatic X-rays interacts with a target material, the atoms in the sample act as scattering centres and the electrons will diffract the incident x-ray in different directions. The diffracted X –rays from the sample interfere constructively at some specific directions when Bragg's law[17, 18],

$$n\lambda = 2d\sin\theta \tag{4}$$

is satisfied, where n is an integer known as the order of diffraction, λ is the wavelength of the incident x-rays, d is the distance between the diffracting planes, θ is the scattering angle also known as the glancing angle. When the diffracted x-rays are in phase with each other, the wave trains superimpose each other constructively and appear as intense spots in the diffraction pattern called Bragg reflections. The diffraction pattern is obtained by scanning the sample through all possible 2θ angles. The intensity of the diffracted waves depends on the particular arrangement of atoms in the crystal structure. The conversion of the diffraction peaks into the corresponding d-spacing values allows finding the lattice spacing of the material.[19]

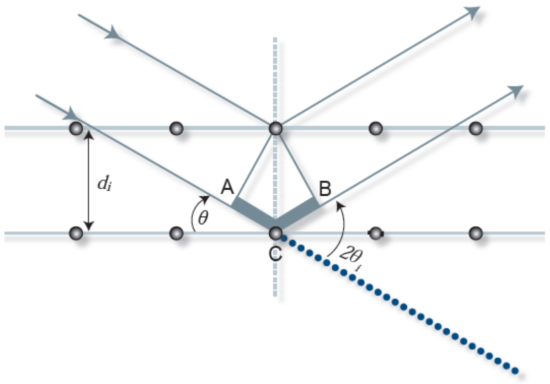

Figure 3.6 Bragg's Diffraction. *Two identical X rays with same phase and wavelength is scattered by two different atoms in 2 parallel planes. Source URL: https://my.bruker.com/acton/attachment/2655/f-0814/1/-/-/-/-/X-Ray%20Powder%20Diffraction%20Bragg-Brentano%20Poster%20XRD%20XRS.pdf*

The x-ray diffractometer basically consist of three different units: the X-ray tube, a sample holder, and a X-ray detector. X-rays are generated in a cathode ray tube in the following manner. The filament heating will produce electrons and the application of voltage will direct them to copper target. The sudden deceleration of the fast moving electrons when hitting the copper target will produce a characteristic X-ray spectrum. The characteristic spectra consist of several components such as K_α and K_β. The wavelength of the CuK_α radiation is around 1.5418 Å. In a typical X-ray diffraction measurement, the K_α line is collimated and directed onto the sample. The x-ray tube and the detector rotate and scan the sample at all possible 2θ values and the detector records the intensity of the reflected rays.

3.4.1.2 Analysis of the interlayer spacing of GO membrane using x-ray diffraction

X ray diffraction (XRD) was employed to evaluate the interlayer spacing d between the (001) plane of graphene oxide membranes. The layer spacing (d_{001}) was measured at different humidity conditions ranging from RH-0%-100%. The measurement was done in the 2θ range of 5° to 15° (with a step size of 0.02° and scanning rate of 0.1 s) using a Bruker D8 diffractometer operated at 40 kV and 20 mA with Cu Kα radiation ($\lambda = 1.5406$ Å). Before collecting the XRD spectrum of the GO membranes stored at specific RHs, we have created the same humidity environment inside the XRD specimen holder (Bruker, C79298A3244D83/85) and sealed it with the corresponding GO membrane. For the zero humidity environments, an airtight sample holder (Bruker, A100B36/B37) was used. All the X-ray diffraction measurements were done in a short scanning time to avoid heating effect of X-rays and the moisture build up inside the membrane. The d spacing of the membranes was calculated using the Bragg's equation

3.4.2 Scanning electron microscopy

The scanning electron microscope (SEM) is a type of electron microscope that produces images by focussing a beam of high-energy electrons on a surface. The high energy electron beam will interact with a surface of solid specimens, producing several signals that can be used to obtain information about the surface topography, chemical composition, crystalline structure and crystal orientations of the sample. In most imaging applications, the two dimensional image is constructed by collecting the electron-sample interaction signals. The maximum spatial resolution and magnification achievable using the SEM technique is 1 nanometre and a magnification of 30,000X respectively[20, 21].

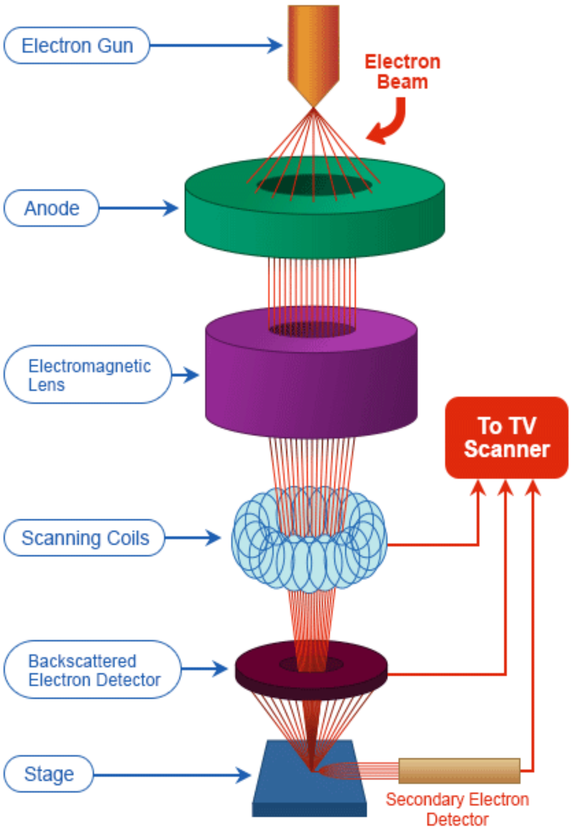

Figure 3.7 Schematic diagram of scanning electron microscope.

Image courtesy: http://www.nanoimages.com/sem-technology-overview/

The kinetic energy, possessed by t high energy electrons is dissipated as various signals due to electron sample interactions. The signals generated by these interactions include secondary electrons, backscattered electrons (BSE), characteristic X-rays , visible light (cathodoluminescence–CL) and absorbed current (specimen current). Backscattered electrons and secondary electrons are used for the imaging of the specimen. The most commonly used SEM mode is the detection of the secondary electrons emitted by the atoms excited by electron beams that are close to the specimen surface.

The secondary electron detection provides valuable information regarding morphology and topography. Back-scattered electrons (BSE) are produced by elastic scattering from deep within the sample. BSE images are useful for the determination of different elements in the sample.

3.4.3 Transmission electron microscopy

A Transmission Electron Microscope (TEM) utilizes energetic electrons to provide morphologic, compositional and crystallographic information on samples in which a stream of high energy electrons is transmitted through a specimen to form an image. A high energy beam of electrons is exposed through a very thin sample, and the interactions between the electrons and the specimen can be used to observe many features such as the crystal structure and chemical information[22-25]. The TEM operates on the same principle as the light microscope but uses electrons instead of light as the wavelength of electrons is much smaller than that of light providing the optimal resolution far better than the light microscope. The TEMs can reveal the finest details of internal structure -in some cases as small as individual atoms.

TEM consist of various components such as an electron source, thermionic gun, electron beam, electromagnetic lenses, vacuum chamber, 2 condensers, sample stage and phosphor or fluorescent screen, and is shown in figure 3.8. A TEM functions under the same basic principles as an optical microscope. In a TEM, electrons replace photons, electromagnetic lenses replace glass lenses and images are viewed on a screen rather than through an eyepiece. There are essentially three types of lenses used to form the final image in the TEM. These are the condenser, objective, and projector lenses. The main function of the condenser lens is to concentrate and focus the beam of electrons coming off of the filament onto the sample to give a uniformly illuminated sample. The objective lens and its associated pole pieces are the heart of the TEM and the most critical of all the lenses. It forms the initial enlarged image of the illuminated portion of the specimen in a plane that is suitable for further enlargement by the projector lens. When an electron beam passes through a thin-section specimen of a material, electrons are scattered. The sophisticated system of electromagnetic lenses focuses the scattered electrons into an image or a diffraction pattern, or a nano analytical spectrum, depending on the mode of operation. Each of these modes offers a different insight about the specimen.

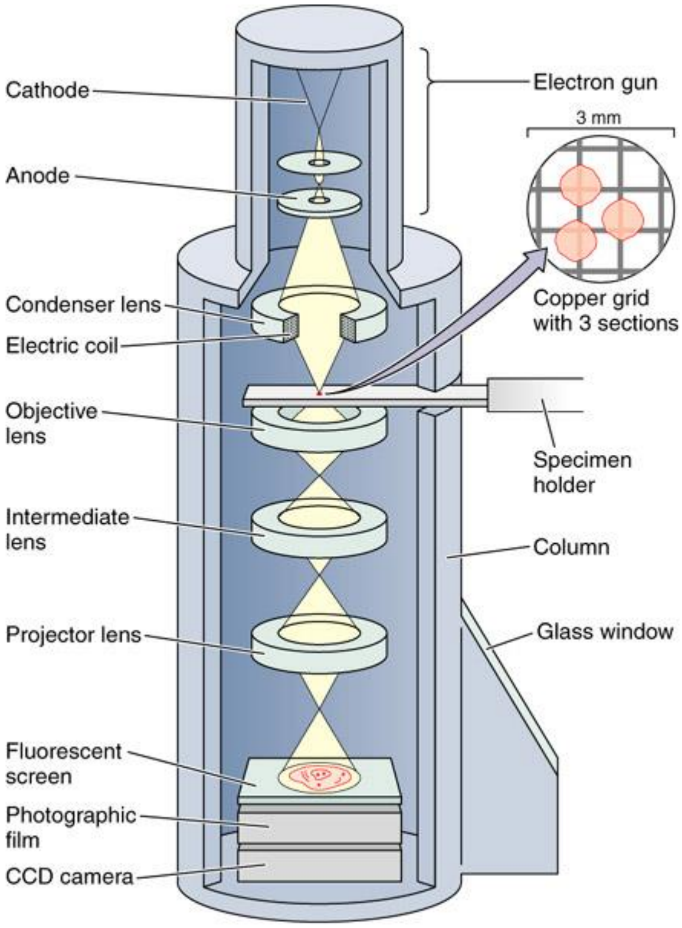

Figure 3.8 Schematic view of the transmission electron microscope. *Image courtesy Reproduced with permission from ref*[26]*, copyright 2005, The McGraw-Hill Companies*

The imaging mode provides a highly magnified view of the micro- and nanostructure, while in the high resolution imaging mode a direct map of atomic arrangements can be obtained (high resolution TEM or HRTEM). The diffraction mode (selected area electron diffraction, SAED) displays accurate information about the local crystal structure. The nano analytical modes (x-ray and electron spectrometry) give an idea about the elements that are present in the tiny volume of material.

TEM builds an image through differential contrast. The electrons that pass through the sample go on to form the image, while those that are stopped or deflected by dense atoms in the specimen are subtracted from the image. In this way a black and white image is formed. Some electrons pass close to heavy atom and are thus only slightly deflected. Thus many of these scattered electrons eventually make their way down the column and contribute to the image. In order to eliminate these scattered electrons from the image an aperture is placed in the objective lens that will stop all those electrons that have deviated from the optical path. The smaller the aperture used, the more of these scattered electrons will be stopped and the greater will be the image contrast. The projector lens is to project the final magnified image onto the phosphor screen or a photographic emulsion. It is in the projector lens that the majority of the magnification occurs. Thus total magnification is a product of the objective and projector magnifications. For higher magnifications an intermediate lens is often added between the objective and this lens serves to further magnify the image**.**

3.4.4 Inductively coupled plasma-atomic emission spectrometry

Inductively coupled plasma atomic emission spectroscopy (ICP-AES); also known as inductively coupled plasma optical emission spectrometry (ICP-OES) is an element specific, sensitive trace analytical technique used for the detection of trace levels of metals in the sample[27-30].

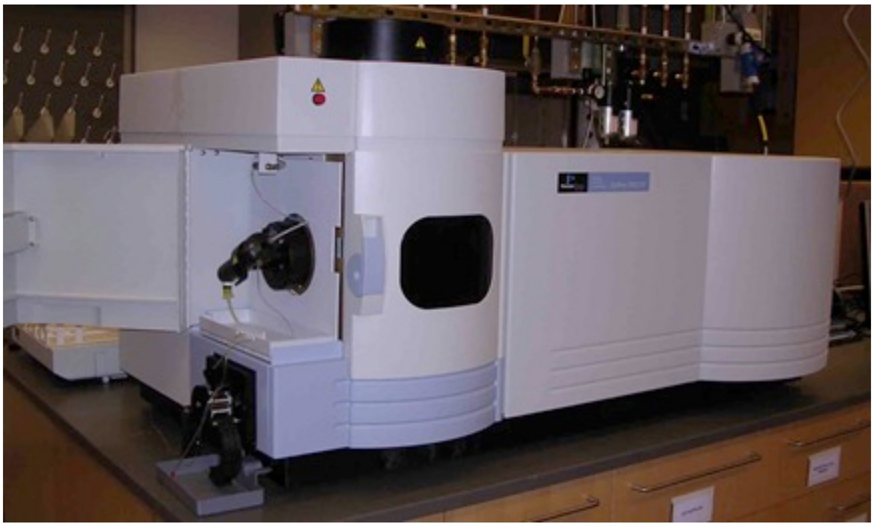

Figure 3.9 Perkin-Elmer optima 5300 dual view ICP-AES

Source URL: http://www.ecs.umass.edu/eve/facilities/inorganics.html

The term atomic spectrometry generally implies, electromagnetic radiation being absorbed or emitted from atoms or ions. As the name indicates, the spectra is measured and characterized by an atomic emission spectrometer (AES) using concentration-intensity correlation[31-33]. Quantitative and qualitative information of the sample can be obtained from this spectroscopic technique. The intensity of the electromagnetic radiation emitted by the charged ions is proportional to the concentration of the ions (quantitative information). An element present in the sample (qualitative information) is related to the wavelengths of the emission lines[34, 35]. The ICP-AES generally composes of two parts: the ICP torch and the optical spectrometer[33] (Figure 3.10)

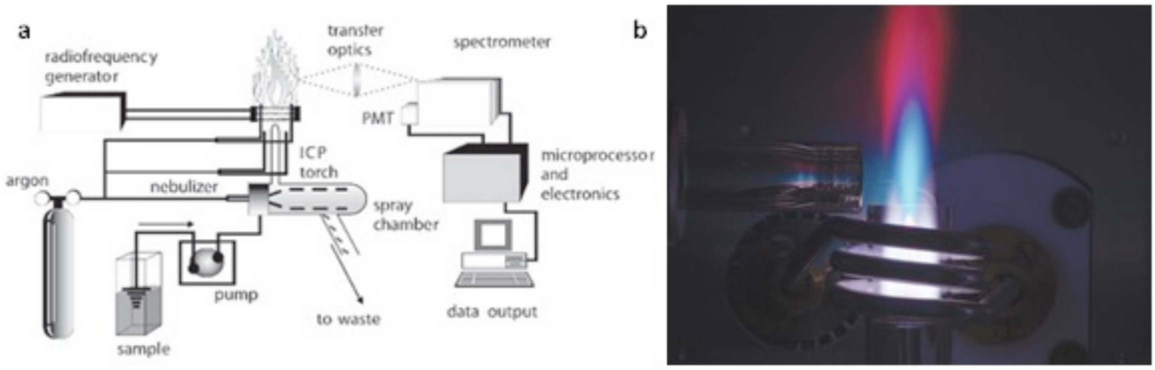

Figure 3.10 ICP-AES Instrument. (a) *Typical layout of an ICP-AES instrument.* ***(b)*** *plasma torch, Source URL:*

(a) *https://www.azom.com/article.aspx?ArticleID=12874.****(b)*** *http://www.analytica-world.com/en/whitepapers/1126584/selecting-your-icp-oes-analyzer-s-plasma-interface-axial-view-radial-view-dual-view-or-new-multiview.html*

The ICP torch consists of three concentric quartz glass tubes surrounded by a copper coil, which is connected to a radio frequency (RF) generator[36, 37]. Argon gas is used to create the plasma and is purged through the ICP torch.

When the ICP torch is switched on, an alternating current will be generated within the coil, oscillating at a rate proportional to the frequency of the RF generator. This RF oscillation of the current in the coil will generate RF electric and magnetic fields which will build up at the top end of the torch[36]. As the argon gas flows through the torch, a spark is applied to the gas by a tesla unit to initiate the ionization of the argon gas. With this spark, some of the electrons will be stripped off and argon atoms become ionized. The free electrons are then attracted by magnetic fields generated by the RF coil which provides additional acceleration. The extra energy gained by the electrons in this way is known as inductive coupling. The high energy electrons again collide with other argon atoms causing further ionization leading to the stripping off more electrons and this collisional ionization continues in a chain reaction. This process causes the splitting up off argon gas into plasma; composed of free electrons, argon ions and argon atoms. The plasma generation by the inductive coupling is known as the inductively coupled plasma (ICP) discharge. In inductive coupling, the RF energy transferred to the free electrons will make them energetic and will lead to the collision with argon atoms and ions causing a rapid increase in the temperature of the plasma to as high as 10,000K[38].

The sample either in aqueous or non-aqueous form is delivered into the analytical nebulizer using a peristatic pump, where it is transformed into mist and introduced directly into the plasma flame by a stream of argon gas. In the extreme temperature of the plasma, the various molecules will break down into their respective atoms, which again collide with argon ion and free electrons causing the breakdown of various atoms present in the analyte to its corresponding ionic form. The excited electrons will emit energy at a characteristic wavelength as they return to ground state by a process called recombination[39]. The emitted light is focussed into the optical chamber using a pair transfer lenses and directed onto a diffraction grating, where it is split into the constituent wavelengths. The intensity of the separated light components is measured by a photomultiplier tube or using a charge coupled device (CCD) and compared with previously measured known concentration of the elements. This allows to find the concentration of the sample by interpolation along the calibration lines. Detection limits typically range from parts per million (ppm) to parts per billion (ppb), depending on the elements present.

3.4.5 Ion Chromatography

Ion chromatography (IC) or ion exchange chromatography is a kind of liquid chromatography used to separate ions and polar molecules based on their affinity to the ion exchange resins. IC works for almost all kinds of charged molecules including large proteins, small nucleotides and amino acids[40]. Ion exchange resins are loaded into columns and are used as the stationary phase. The liquid or analyte pumped through this resin is known as the mobile phase. The stationary phase consists of an immobile resin that is composed of charged ionisable functional groups or ligands. The functional groups that are attached to the stationary phase will interact with the analyte ions of opposite polarity through columbic interaction. A pump is used to deliver the mobile phase to the ion exchange resins. The sample ions contained in the mobile phase will interact with the ion exchange sites in the resin. If the column is an anion column, the resin will consist of several positively-charged sites[41].

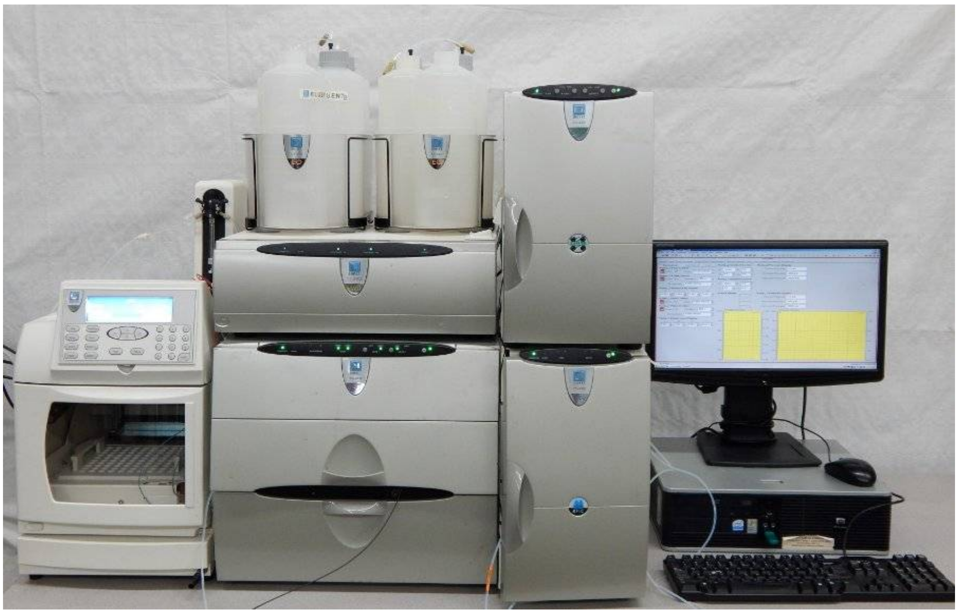

Figure 3.11 Dionex ICS Series 3000 Ion Chromatography System

Source URL: http://www.rollabiotech.com/dionex-ics-series-3000-ion-chromatography-system-with-computer-w-software-and-dongle

The stream of ions is passes into a suppressor, where the background conductivity of the mobile phase is reduced by a neutralisation reaction. The conductivity of the ions is thus increased, relative to the background. As the ions pass through the conductivity detector, a peak is formed and the area under the measured peak is compared with the peaks from calibration standards. The peak area is proportional to the concentration of ions.

3.5 References

1. Eigler, S.; Enzelberger-Heim, M.; Grimm, S.; Hofmann, P.; Kroener, W.; Geworski, A.; Dotzer, C.; Röckert, M.; Xiao, J.; Papp, C.; Lytken, O.; Steinrück, H.-P.; Müller, P.; Hirsch, A. *Adv. Mater.* **2013,** 25, (26), 3583-3587.

2. Hummers, W. S.; Offeman, R. E. *J. Am. Chem. Soc.* **1958,** 80, (6), 1339-1339.

3. Marcano, D. C.; Kosynkin, D. V.; Berlin, J. M.; Sinitskii, A.; Sun, Z.; Slesarev, A.; Alemany, L. B.; Lu, W.; Tour, J. M. *ACS Nano* **2010**, 4806–4814.

4. Rezania, B.; Severin, N.; Talyzin, A. V.; Rabe, J. P. *Nano Lett.* **2014,** 14, (7), 3993-3998.

5. Lerf, A.; Buchsteiner, A.; Pieper, J.; Schöttl, S.; Dekany, I.; Szabo, T.; Boehm, H. P. *J. Phys. Chem. Solids* **2006,** 67, (5), 1106-1110.

6. Cerveny, S.; Barroso-Bujans, F.; Alegría, Á.; Colmenero, J. *J. Phys. Chem. C* **2010,** 114, (6), 2604-2612.

7. Greenspan, L. *J Res Natl Bur Stand* **1977** 81 A.

8. Rockland, L. B. *Anal. Chem.* **1960,** 32, (10), 1375-1376.

9. Tansel, B. *Sep. Purif. Technol.* **2012,** 86, 119-126.

10. Tansel, B.; Sager, J.; Rector, T.; Garland, J.; Strayer, R. F.; Levine, L.; Roberts, M.; Hummerick, M.; Bauer, J. *Sep. Purif. Technol.* **2006,** 51, (1), 40-47.

11. Chua, C. K.; Pumera, M. *Chem. Soc. Rev.* **2014,** 43, (1), 291-312.

12. Jung, I.; Field, D. A.; Clark, N. J.; Zhu, Y.; Yang, D.; Piner, R. D.; Stankovich, S.; Dikin, D. A.; Geisler, H.; Ventrice, C. A.; Ruoff, R. S. *J. Phys. Chem. C* **2009,** 113, (43), 18480-18486.

13. Perera, R. T.; Johnson, R. P.; Edwards, M. A.; White, H. S. *J. Phys. Chem. C* **2015,** 119, (43), 24299-24306.

14. Birkholz, M., *Thin Film Analysis by X-Ray Scattering*. 2005; p 378.

15. Brady, J. B.; Boardman, S. J. *Journal of Geological Education* **1995,** 43, (5), 471-476.

16. Copeland, L. E.; Bragg, R. H. *Anal. Chem.* **1958,** 30, (2), 196-201.

17. *Proceedings of the Royal Society of London. Series A* **1913,** 89, (610), 248.

18. Warren, B. E., *X-ray Diffraction*. Courier Corporation: 1969.

19. Klug, H. P.; Alexander, L. E. *X-Ray Diffraction Procedures: For Polycrystalline and Amorphous Materials, 2nd Edition, by Harold P. Klug, Leroy E. Alexander, pp. 992. ISBN 0-471-49369-4. Wiley-VCH, May 1974.* **1974**, 992.

20. Dehm, G.; Howe, J. M.; Zweck, J., *In-situ electron microscopy: applications in physics, chemistry and materials science*. John Wiley & Sons: 2012.

21. McMullan, D. *Scanning* **1995,** 17, (3), 175-185.

22. Fultz, B.; Howe, J. M., *Transmission electron microscopy and diffractometry of materials*. Springer Science & Business Media: 2012.

23. Champness, P. E., *Electron diffraction in the transmission electron microscope. RMS Microscopy handbook no. 47*. Oxford.: BIOS Scientific publishers Ltd: 2001.

24. Egerton, R. F., *Physical principles of electron microscopy*. Springer: 2005.

25. Williams, D. B.; Carter, C. B., The transmission electron microscope. In *Transmission electron microscopy*, Springer: 1996; pp 3-17.

26. Junqueira, L. C.; Carneiro, J., *Basic histology: text and atlas*. McGraw-Hill Professional: 2005.

27. Dahlquist, R.; Knoll, J. *Appl. Spectrosc.* **1978,** 32, (1), 1-30.

28. Manning, T. J.; Grow, W. R. *The chemical educator* **1997,** 2, (1), 1-19.

29. Thomas, R., *Practical guide to ICP-MS: a tutorial for beginners*. CRC press: 2013.

30. Hou, X.; Amais, R. S.; Jones, B. T.; Donati, G. L. *Encyclopedia of analytical chemistry* **2000**.

31. Charles, B.; Fredeen, K. J.

32. de Villiers, S.; Greaves, M.; Elderfield, H. *Geochemistry, Geophysics, Geosystems* **2002,** 3, (1).

33. Charles, B.; Fredeen, K. J. *Perkin Elmer Corporation* **1997**.

34. Winge, R.; Peterson, V.; Fassel, V. A. *Appl. Spectrosc.* **1979,** 33, (3), 206-219.

35. Winge, R.; Fassel, V.; Peterson, V.; Floyd, M.; McLeod, C., Inductively coupled plasma-atomic emission spectroscopy. An atlas of spectral information: Elsevier, Amsterdam, 1985 (ISBN 0-444-42358-3). x+ 584 pp. Price Dfl. 500.00/US $192.25. elsevier: 1989.

36. Rezaaiyaan, R.; Hieftje, G.; Anderson, H.; Kaiser, H.; Meddings, B. *Appl. Spectrosc.* **1982,** 36, (6), 627-631.

37. McClenathan, D. M.; Wetzel, W. C.; Lorge, S. E.; Hieftje, G. M. *J. Anal. At. Spectrom.* **2006,** 21, (2), 160-167.

38. Huang, M.; Marshall, K. A.; Hieftje, G. M. *Anal. Chem.* **1986,** 58, (1), 207-210.

39. Winge, R. K.; Peterson, V. J.; Fassel, V. A. *Appl. Spectrosc.* **1979,** 33, (3), 206-219.

40. Fritz, J. S. *Anal. Chem.* **1987,** 59, (4), 335A-344A.

41. Duong-Ly, K. C.; Gabelli, S. B., Chapter Eight - Using Ion Exchange Chromatography to Purify a Recombinantly Expressed Protein. In *Methods Enzymol.*, Lorsch, J., Ed. Academic Press: 2014; Vol. 541, pp 95-103.

Blank Page

Chapter 4- Tunable Sieving of Ions using Graphene Oxide Membranes

Introduction

The results presented in this section were published in the article: " Tunable sieving of ions using graphene oxide membranes" *Nature Nanotechnology* **12**, 546-550 (2017).

Selectively permeable membranes with sub-nanometre sieve size are getting tremendous attraction due to their similarities with biological ion channels, unique mechanism of ion selectivity and potential applications in water filtration, molecular separation and desalination[1-8]. Sub-nm pores with pore size comparable or smaller than the size of hydrated ions are predicted to show enhanced ion selectivity[8-11] due to the difference in ion dehydration behaviour defined by the electrostatic interactions between ions and water. Despite many theoretical predictions related to dehydration[8-11] and its relevance in important applications such as desalination, its application for ion sieving or water filtration has not been achieved experimentally due to the difficulty in fabricating uniform and exclusive sub-nm pores. Considering these facts, realisation of new generation membranes with dehydration defined ion selectivity might be very important due to the several drawbacks like low water permeation, poor ion selectivity, low chemical stability and high cost of the conventional membrane materials such as zeolites, silica, metal-organic frameworks and polymeric membranes[12-15]. Recently, carbon nanomaterials particularly carbon nanotubes (CNT) and graphene have emerged as an efficient alternate membrane materials to overcome the above-mentioned difficulties but the former is found to be difficult to manufacture in large scale[4-6, 12, 16]. Graphene-based membranes with sub-nm pores are predicted to show ion selectivity, high salt rejection and enhanced water flux, therefore, are suitable for water filtration and desalination applications[6, 8]. Several approaches have been employed recently to use single layer graphene as a membrane for ionic separation by intentionally creating sub-nm sized pores by ion bombardment and etching process[1-4]. However, stochastic pore distribution and lack of industrial scalability limit its practical application. In contrast, GO, a chemical derivative of graphene with oxygen functionalities[17] has attracted enormous attention in the membrane technology due to its exceptional water permeation properties[18] and ease in scaling up for large scale production[19, 20].Wide range of permeation properties such as, unimpeded permeation of water[18], precise and ultrafast molecular sieving[21-23] and complete impermeability[24] made GO as a suitable candidate in the membrane technology for filtration, separation and coating applications[20]. Molecular permeation through GO membranes involves the tortuous inter-layer graphene channels and its sieving properties are defined by the IL-spacing which is susceptible to the water content in the environment[18, 21]. Despite the remarkable properties shown by GO membranes, hydration of graphene capillaries expands the interlayer spacing to~ 13-14, typical for GO that exposed to water. If the graphene sheet thickness is removed from this value, the effective free space in the swollen state for ion permeation is close to 10 Å, which is larger than the hydrated diameters of any common salts, limiting the use in desalination technologies. Here we have developed a new strategy to fabricate swelling controlled and tunable sub nanometre capillaries in GO membranes by physical confinement and studied the ion behaviour through such capillaries.

My contribution to this work: Fabricated all PCGO membrane samples, performed all the experiments such as ion permeation, XRD measurements, forward osmosis and water flux measurements. Participated in the data analysis and contributed towards drafting of the manuscript. Introduction and materials and methods section of the main text in particular and forward osmosis measurements/water flux measurements and ion permeation through PCGO membranes part of the supplementary text.

Full author list: Jijo Abraham, Kalangi S. Vasu, Christopher D. Williams, KalonGopinadhan, Yang Su, Christie T. Cherian, James Dix, Eric Prestat, Sarah J. Haigh, Irina V. Grigorieva, [1] Paola Carbone, Andre K. Geim and Rahul R. Nair.

Full author contributions: R.R.N. designed and supervised the project with the help from J.A. K.S.V.; J.A. and K.S.V. prepared the samples, performed the measurements and carried out the analysis with help from R.R.N.; J.D., C.D.W. and P.C. carried out MD simulations and data analysis. K.G., Y.S. and C.T.C. helped in sample preparation, characterization and data analysis. E.P. and S.J.H. contributed to sample characterization. A.K.G. participated in discussions and project design. R.R.N., K.S.V., J.A., C.D.W., I.V.G. and A.K.G. wrote the manuscript. All authors contributed to discussions.

---

[1] K.S Vasu developed a scalable method to prepare swelling controlled GO membrane by incorporating graphene flakes into GO. He participated in the discussion and manuscript preparation. We both are joint first authors for this work.

LETTERS
PUBLISHED ONLINE: 3 APRIL 2017 | DOI: 10.1038/NNANO.2017.21

nature nanotechnology

Tunable sieving of ions using graphene oxide membranes

Jijo Abraham[1,2,3†], Kalangi S. Vasu[1,2†], Christopher D. Williams[2], Kalon Gopinadhan[3], Yang Su[1,2], Christie T. Cherian[1,2], James Dix[2], Eric Prestat[4], Sarah J. Haigh[4], Irina V. Grigorieva[1], Paola Carbone[2], Andre K. Geim[3] and Rahul R. Nair[1,2*]

Graphene oxide membranes show exceptional molecular permeation properties, with promise for many applications[1–5]. However, their use in ion sieving and desalination technologies is limited by a permeation cutoff of ~9 Å (ref. 4), which is larger than the diameters of hydrated ions of common salts[4,6]. The cutoff is determined by the interlayer spacing (*d*) of ~13.5 Å, typical for graphene oxide laminates that swell in water[2,4]. Achieving smaller *d* for the laminates immersed in water has proved to be a challenge. Here, we describe how to control *d* by physical confinement and achieve accurate and tunable ion sieving. Membranes with *d* from ~9.8 Å to 6.4 Å are demonstrated, providing a sieve size smaller than the diameters of hydrated ions. In this regime, ion permeation is found to be thermally activated with energy barriers of ~10–100 kJ mol^{-1} depending on *d*. Importantly, permeation rates decrease exponentially with decreasing sieve size but water transport is weakly affected (by a factor of <2). The latter is attributed to a low barrier for the entry of water molecules and large slip lengths inside graphene capillaries. Building on these findings, we demonstrate a simple scalable method to obtain graphene-based membranes with limited swelling, which exhibit 97% rejection for NaCl.

Selectively permeable membranes with subnanometre pores attract strong interest due to their analogous behaviour with biological membranes and potential applications in water filtration, molecular separation and desalination[7–14]. Nanopores with sizes comparable to, or smaller than, the diameter *D* of hydrated ions are predicted to show enhanced ion selectivity[14–18] because of dehydration required for the permeation of ions through such atomic-scale sieves. Despite extensive research on ion dehydration effects[9,14–19], experimental investigation of the ion sieving controlled by dehydration has been limited because of difficulties in fabricating uniform membranes with well-defined subnanometre pores. The realization of membranes with dehydration-assisted selectivity would be a significant step forward. So far, research into novel membranes has mostly focused on improving the water flux rather than on ion selectivity. On the other hand, modelling of practically relevant filtration processes shows that an increase in water permeation rates above the rates currently achieved (2–3 l m^{-2} h^{-1} bar^{-1}) would not contribute greatly to the overall efficiency of desalination[13,20,21]. Alternative approaches based on higher water-ion selectivity may open new possibilities for improving filtration technologies, as the performance of state-of-the-art membranes is currently limited by the solution-diffusion mechanism, in which water molecules dissolve in the membrane material and then diffuse across the membrane[13]. Recently, carbon nanomaterials including carbon nanotubes and graphene have emerged as promising membrane materials. Unfortunately, such membranes are difficult to manufacture on an industrial scale[10,11,13,22]. In particular, monolayer graphene was suggested as a membrane for ion exclusion by creating subnanometre pores using ion bombardment and selective etching[7–10]. However, it is difficult to achieve the high density and uniformity of such pores, which is required for industrial applications, because of the stochastic nature of the involved processes. In contrast, graphene oxide (GO), a chemical derivative of graphene with oxygen functionalities[23], has attracted widespread interest due to its exceptional water permeation and molecular sieving properties[1,2,4] as well as realistic prospects for industrial-scale production[3,5]. Molecular permeation through GO membranes is believed to occur along a network of pristine graphene channels that develop between functionalized areas of GO sheets[1] (typically, an area of 40–60% remains free from functionalization[24,25]), and their sieving properties are defined by the interlayer spacing, *d*, which depends on the humidity of the surroundings[1,4]. Immersing GO membranes in liquid water leads to intercalation of 2–3 layers of water molecules between individual GO sheets, which results in swelling and *d* ≈ 13.5 Å. A number of strategies have been tried to inhibit the swelling effect, including partial reduction of GO (ref. 26), ultraviolet reduction of GO–titania hybrid membranes[27] and covalent crosslinking[28–30]. In this Letter, we investigate ion permeation through GO laminates with *d* controlled from ≈9.8 to ≈6.4 Å, which is achieved by physical confinement (Fig. 1a).

Thick (≈100 μm) GO laminates prepared as reported previously[1] were cut into rectangular strips (4 mm × 10 mm) and stored for 1 to 2 weeks at different relative humidities (RH), achieved using saturated salt solutions[1,31]. The resulting interlayer spacing (Fig. 1e) was varied from ≈6.4 to 9.8 Å with RH changing from 0 to 100%. GO laminates soaked in liquid water showed *d* ≈ 13.7 ± 0.3 Å. All these values agree with previous reports, where the changes in *d* were attributed to successive incorporation of water molecules into various sites between GO sheets[32]. Individual GO strips with desirable *d* were then encapsulated and stacked together using Stycast epoxy as shown in Fig. 1b,c to increase the available cross-section for filtration to ~1 mm (see Methods and Supplementary Fig. 1). The stacked GO laminates, embedded in the epoxy (Fig. 1c), are referred to as physically confined GO (PCGO) membranes because the epoxy mechanically restricts the swelling of the laminate on exposure to RH or liquid water (see Methods). The stacks were glued into a slot made in either a metal or plastic plate (Fig. 1b). Two sides of these stacked PCGO membranes were then trimmed off to make sure that all the nanochannels

---

[1] National Graphene Institute, University of Manchester, Manchester M13 9PL, UK. [2] School of Chemical Engineering and Analytical Science, University of Manchester, Manchester M13 9PL, UK. [3] School of Physics and Astronomy, University of Manchester, Manchester M13 9PL, UK. [4] School of Materials, University of Manchester, Manchester M13 9PL, UK. †These authors contributed equally to this work. *e-mail: rahul@manchester.ac.uk

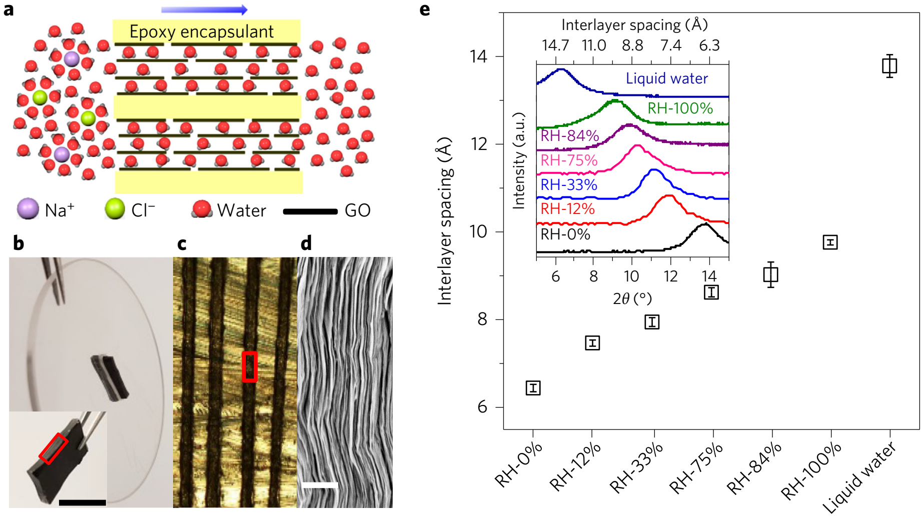

Figure 1 | Physically confined GO membranes with tunable interlayer spacing. a, Schematic illustrating the direction of ion/water permeation along graphene planes. **b**, Photograph of a PCGO membrane glued into a rectangular slot within a plastic disk of 5 cm in diameter. Inset: photo of the PCGO stack before it was placed inside the slot. Scale bar, 5 mm. **c**, Optical micrograph of the cross-sectional area marked by a red rectangle in **b**, which shows 100-μm-thick GO laminates (black) embedded in epoxy. Epoxy is seen in light yellow with dark streaks because of surface scratches. **d**, Scanning electron microscopy image from the marked region in **c**. Scale bar, 1 μm. **e**, Humidity-dependent interlayer spacing, *d*, found using X-ray diffraction (inset). The case of liquid water is also shown. Error bars denote standard deviations using at least two measurements from three different samples.

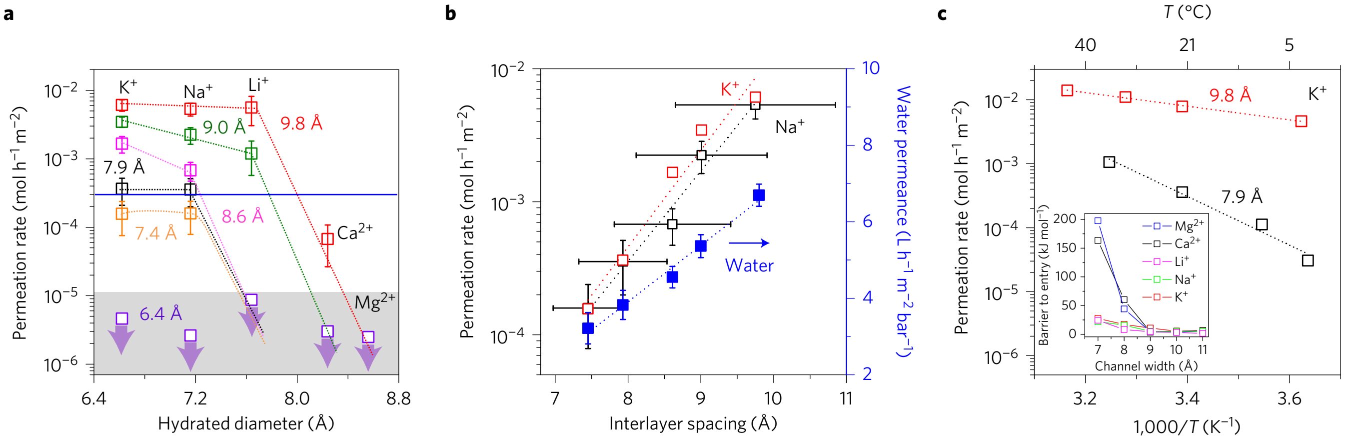

Figure 2 | Tunable ion sieving. a, Permeation rates through PCGO membranes with different interlayer distances (colour coded). The salts used were KCl, NaCl, LiCl, $CaCl_2$ and $MgCl_2$. The hydrated diameters are taken from ref. 6 (Supplementary Section 4). Dashed lines are guides to the eye indicating a rapid cutoff in salt permeation, which is dependent on the interlayer spacing, *d*. Grey area shows the below-detection limit for our measurements lasting five days, with arrows indicating the limits for individual salts. The horizontal blue line indicates our detection limit for Cl^-. Above the latter limit, we found that both cations and anions permeated in stoichiometric quantities. Error bars denote standard deviation. **b**, Permeation rates for K^+ and Na^+ depend exponentially on the interlayer distance (left axis). Water permeation varied only linearly with *d* (blue squares, right axis). The dotted lines are best fits. The horizontal error bars correspond to a half-width for the diffractions peaks in Fig. 1e and are same for all the three data sets. The vertical error bars indicate the standard deviation. The errors for K^+ are similar to those for Na^+ and have been omitted for clarity. **c**, Temperature dependence for K^+ permeation. Dotted lines are best fits to the Arrhenius behaviour. Inset: energy barriers for various ions and different *d*, as found in our molecular dynamics simulations.

were open (Fig. 1d) before carrying out permeation experiments, in which ions and water molecules permeate along the lamination direction as shown in Fig. 1a.

Our measurement set-up was similar to the one previously reported[4] and consisted of two Teflon compartments (feed and permeate) separated by a PCGO membrane (Supplementary Fig. 2). The feed and permeate compartments were filled with 10 ml of a salt solution and deionized water, respectively. As expected, the ion concentration in the permeate compartment increases with time and with increasing concentration of the feed solution (Supplementary Section 3 and Supplementary Fig. 3). Figure 2a summarizes our results obtained for various ions permeating through PCGO membranes with different interlayer spacing. One can see that the permeation rates and the cutoff diameter for salt permeation decrease monotonically with decreasing *d*. Membranes with $d \approx 6.4$ Å showed no detectable ion concentration in the permeate even after 5 days. This further confirms that our PCGO membranes do not swell in water over time, despite a finite mechanical rigidity of the epoxy confinement. When plotted as a function of *d*, the observed ion permeation rates for Na^+ and K^+ showed an exponential dependence, decreasing by two orders of magnitude as *d* decreased from 9.8 to 7.4 Å (Fig. 2b). In contrast, the same PCGO membranes (Supplementary Section 5) showed only a little variation in permeation rates for water (Fig. 2b),

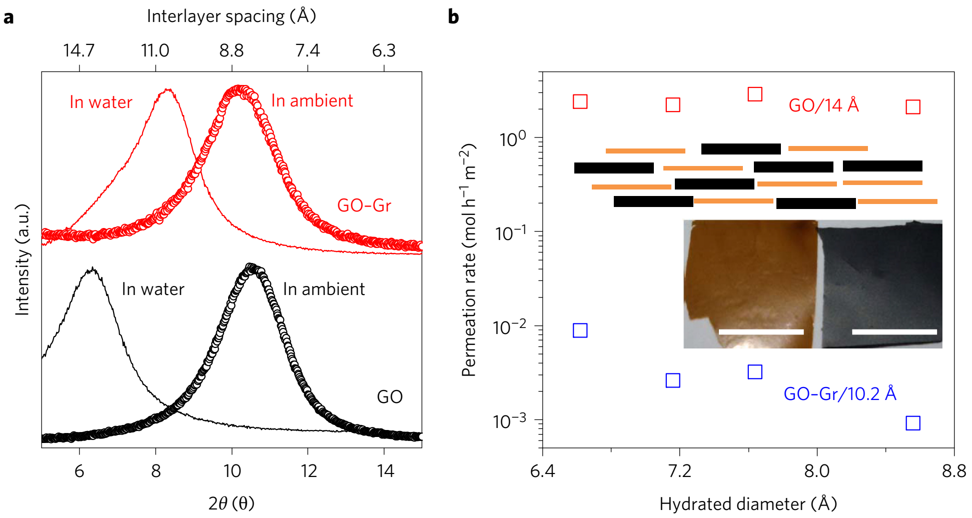

Figure 3 | Graphene oxide membrane with limited swelling. a, X-ray diffraction showing shifts of the (001) peak due to swelling in liquid water for the standard GO laminate and a composite made from graphene and graphene oxide (GO-Gr). **b**, Ion permeation rates (same salts as in Fig. 2) through such GO ($d \approx 14$ Å) and GO-Gr ($d \approx 10.2$ Å) membranes with a thickness of 5 µm. Top inset: schematic of the GO-Gr structure (brown blocks, GO; black, graphene). Bottom inset: photographs of GO and GO-Gr membranes (left, and right, respectively). Scale bars, 1 cm.

decreasing by a factor of ≈2 for the same range of d. We note that this observation rules out that the exponential changes in ion permeation could be related to partial clogging of graphene capillaries.

Both the observed relatively high permeation rates for Li^+, K^+ and Na^+ for $d > 9$ Å and their exponential decay for smaller d are surprising. Indeed, when considering steric (size-exclusion) effects, it is often assumed that ions in water occupy a rigid volume given by their hydrated diameters D. If this simplification was accurate, our PCGO membranes should not allow permeation of any common salt. Indeed, the effective pore size δ can be estimated as $d - a$, where $a \approx 3.4$ Å is the thickness of graphene[1,33]. This yields $\delta \approx 6.4$ Å for our largest capillaries ($d \approx 9.8$ Å), which is smaller than D for all the ions in Fig. 2a. This clearly indicates that ion sieving is not purely a geometric effect. On the other hand, if we assume that hydrated ions do fit into the nanochannels and their permeation is only limited by diffusion through water, the expected permeation rates should be significantly higher than those observed experimentally. For classical diffusion the permeation rate J is given by

$$J = \mathrm{Diff} \times \Delta C \times A_{\mathrm{eff}} / L \qquad (1)$$

where ΔC is the concentration gradient across the membrane (1 M for the experiments in Fig. 2), A_{eff} is the total cross-sectional area of nanocapillaries (≈3–8 mm^2), L is the diffusion length through the PCGO membrane (≈3 mm) and Diff is the diffusion coefficient for ions in water (typically, Diff ~10^{-5} cm^2 s^{-1}; see Supplementary Section 6). Equation (1) yields rates that are 2–4 orders magnitude higher than those shown in Fig. 2. This is in stark contrast to the sieving properties of GO laminates with $d \approx 13.5$ Å that showed an enhancement rather than suppression of ion diffusion[4]. Clearly, the fact that the available space δ in PCGO laminates becomes smaller than D pushes the permeating hydrated ions into a new regime, distinct both from ions moving through wider nanocapillaries and from permeation behaviour of pure water. In the latter case, as shown in Fig. 2b, permeation rates for water molecules (whose size is smaller than δ) are three orders of magnitude higher than those estimated from the standard Hagen–Poiseuille equation using non-slip boundary conditions and the given dimensions of nanocapillaries (Supplementary Section 5). Similar flow enhancement (by three orders of magnitude) was recently reported for artificial graphene capillaries and attributed to a large slip length of ~60 nm for water on graphene[33].

To gain an insight into the mechanism of ion permeation through our membranes, we carried out permeation experiments at different temperatures, T (Fig. 2c). For both channel sizes, $d = 9.8$ Å and $d = 7.9$ Å, the permeation rates follow the Arrhenius equation, $\exp(-E/k_BT)$, that is, show activation behaviour. Here, E is the energy barrier and k_B is the Boltzmann constant. The data yield $E = 72 \pm 7$ kJ mol^{-1} and 20 ± 2 kJ mol^{-1} for K^+ ion permeation through PCGO membranes with $d \approx 7.9$ and 9.8 Å, respectively. The exponential dependence explains the fact that the observed ion diffusion rates are orders of magnitude smaller than those given by equation (1), as at room temperature $E \gg k_BT$ for both channel sizes. The activation behaviour is also in agreement with recent theoretical predictions that nanopores with diameters <10 Å should exhibit significant energy barriers because of the required partial dehydration for the entry of ions[9,14–18]. Qualitatively, this mechanism can be explained as follows. In a bulk solution, water molecules stabilize ions by forming concentric hydration shells. For an ion to enter a channel with $\delta < D$, some water molecules must be removed from the hydration shell. The higher the ion charge, the stronger it attracts water molecules. Accordingly, ions with larger hydration free energies[34] and, therefore, 'tougher' water shells are expected to experience larger barriers for entry into atomic-scale capillaries and exponentially smaller permeation rates. Ions with weakly bound shells are easier to strip from their water molecules to allow their entry into nanochannels. Similar arguments can be used to understand why water does not exhibit any exponential dependence on d: water–water interactions are weak, so it costs relatively little energy to remove surrounding water from water molecules entering the capillaries[16].

To support the proposed mechanism of dehydration-limited ion permeation for our PCGO membranes, we employed the previously suggested model of a network of graphene capillaries, which was developed to account for the fast permeation of water through GO membranes[1,4,18]. Within this model, we performed molecular dynamics simulations to find energy barriers for various ions entering graphene capillaries of different widths (Supplementary Section 6). As seen in Fig. 2c the energy barrier E exhibits a sharp increase for d < 9 Å and is considerably larger for divalent ions compared with monovalent ions, in agreement with our experiments and the above discussion (Fig. 2a). Quantitatively, the obtained E are of the same order of magnitude as those found experimentally; the discrepancy in exact values can be expected because realistic GO channels contain non-stoichiometric functionalities, rough edges and so on, which are difficult to model accurately. We also performed simulations to evaluate a possible contribution of diffusion rates through capillaries themselves to the overall permeation rates. Our results show that the diffusion coefficient for K^+ changes with d but the effect is small compared with the exponential decrease in permeation rates, which was observed experimentally (Supplementary Section 6). This suggests that the energy barrier associated with dehydration is the dominant effect in our case of subnanometre capillaries.

Finally, the exponential suppression of ion permeation combined with fast water transport in PCGO membranes make them an interesting candidate for water filtration applications. Even though scalable production of such membranes is difficult, one can envisage using alternative fabrication techniques to control d in GO laminates. To this end, we show that it is possible to restrict the swelling of GO membranes in liquid water, for example, simply by incorporating graphene (Gr) flakes into GO laminates (Supplementary Section 7). The resulting composites referred to as GO–Gr membranes exhibit notably less swelling (difference in d of ≈4 Å) with respect to the standard GO laminates (Fig. 3a). The observed large difference in d can be due to graphene's hydrophobicity that limits the water intake. The ion permeation rate through GO–Gr membranes was found to be suppressed by more than two orders of magnitude compared with GO (Fig. 3b), in agreement with the projected rates for the given extent of swelling if the exponential dependence of Fig. 2 is extrapolated. At the same time, water permeation rates are essentially unaffected by the incorporation of graphene into GO laminates (decrease only by 20%; Supplementary Section 7). The salt rejection properties of our GO–Gr membranes were further investigated using forward osmosis, where we employed concentrated sugar (3 M) and NaCl (0.1 M) solutions as the draw and feed solutions, respectively (Supplementary Section 7). Salt rejection was calculated as $1 - C_d/C_f$, where C_d and C_f are the concentration of NaCl at the draw and feed sides, respectively. Our analysis yielded ≈97% salt rejection for the GO–Gr membranes with a water flux of $\approx 0.5\,\mathrm{l\,m^{-2}\,h^{-1}}$. Even though the flux is lower than $5–10\,\mathrm{l\,m^{-2}\,h^{-1}}$ typical for forward osmosis[35], we believe this characteristic can be significantly improved by decreasing the membrane thickness to 1 μm or less (Supplementary Section 7). Such thicknesses are readily achievable for GO laminates[2] and can result in fluxes $>5\,\mathrm{l\,m^{-2}\,h^{-1}}$.

In conclusion, we have demonstrated the possibility to control the interlayer spacing in GO membranes in the range below 10 Å. In this regime, the capillary size is smaller than the hydrated diameters of ions and their permeation is exponentially suppressed with decreasing d. The suppression mechanism can be described in terms of additional energy barriers that arise because of the necessity to partially strip ions from their hydrated shells so that they can fit inside the capillaries. Water transport is much less affected by d. Our work shows a possible route to the production of GO membranes with controllable interlayer spacing for desalination applications.

Methods

Methods and any associated references are available in the online version of the paper.

Received 29 September 2016; accepted 2 February 2017;

References

1. Nair, R. R., Wu, H. A., Jayaram, P. N., Grigorieva, I. V. & Geim, A. K. Unimpeded permeation of water through helium-leak-tight graphene-based membranes. *Science* **335,** 442–444 (2012).
2. Sun, P. Z., Wang, K. L. & Zhu, H. W. Recent developments in graphene-based membranes: structure, mass-transport mechanism and potential applications. *Adv. Mater.* **28,** 2287–2310 (2016).
3. Liu, G. P., Jin, W. Q. & Xu, N. P. Graphene-based membranes. *Chem. Soc. Rev.* **44,** 5016–5030 (2015).
4. Joshi, R. K. *et al.* Precise and ultrafast molecular sieving through graphene oxide membranes. *Science* **343,** 752–754 (2014).
5. Akbari, A. *et al.* Large-area graphene-based nanofiltration membranes by shear alignment of discotic nematic liquid crystals of graphene oxide. *Nat. Commun.* **7,** 10891 (2016).
6. Tansel, B. Significance of thermodynamic and physical characteristics on permeation of ions during membrane separation: hydrated radius, hydration free energy and viscous effects. *Sep. Purif. Technol.* **86,** 119–126 (2012).
7. O'Hern, S. C. *et al.* Selective ionic transport through tunable subnanometer pores in single-layer graphene membranes. *Nano Lett.* **14,** 1234–1241 (2014).
8. Rollings, R. C., Kuan, A. T. & Golovchenko, J. A. Ion selectivity of graphene nanopores. *Nat. Commun.* **7,** 11408 (2016).
9. Jain, T. *et al.* Heterogeneous sub-continuum ionic transport in statistically isolated graphene nanopores. *Nat. Nanotech.* **10,** 1053–1057 (2015).
10. Surwade, S. P. *et al.* Water desalination using nanoporous single-layer graphene. *Nat. Nanotech.* **10,** 459–464 (2015).
11. Cohen-Tanugi, D. & Grossman, J. C. Water desalination across nanoporous graphene. *Nano Lett.* **12,** 3602–3608 (2012).
12. Wang, L. D. *et al.* Molecular valves for controlling gas phase transport made from discrete ångström-sized pores in graphene. *Nat. Nanotech.* **10,** 785–790 (2015).
13. Werber, J. R., Osuji, C. O. & Elimelech, M. Materials for next-generation desalination and water purification membranes. *Nat. Rev. Mater.* **1,** 16018 (2016).
14. Sahu, S., Ventra, M. D. & Zwolak, M. Dehydration as a universal mechanism for ion selectivity in graphene and other atomically thin pores. Preprint at http://arXiv.org/abs/1605.03134 (2016).
15. Richards, L. A., Schafer, A. I., Richards, B. S. & Corry, B. The importance of dehydration in determining ion transport in narrow pores. *Small* **8,** 1701–1709 (2012).
16. Thomas, M., Corry, B. & Hilder, T. A. What have we learnt about the mechanisms of rapid water transport, ion rejection and selectivity in nanopores from molecular simulation? *Small* **10,** 1453–1465 (2014).
17. Song, C. & Corry, B. Intrinsic ion selectivity of narrow hydrophobic pores. *J. Phys. Chem. B* **113,** 7642–7649 (2009).
18. Williams, C. D. & Carbone, P. Selective removal of technetium from water using graphene oxide membranes. *Environ. Sci. Technol.* **50,** 3875–3881 (2016).
19. Feng, J. *et al.* Observation of ionic Coulomb blockade in nanopores. *Nat. Mater.* **15,** 850–855 (2016).
20. Cohen-Tanugi, D., McGovern, R. K., Dave, S. H., Lienhard, J. H. & Grossman, J. C. Quantifying the potential of ultra-permeable membranes for water desalination. *Energy Environ. Sci.* **7,** 1134–1141 (2014).
21. Deshmukh, A., Yip, N. Y., Lin, S. H. & Elimelech, M. Desalination by forward osmosis: identifying performance limiting parameters through module-scale modeling. *J. Membr. Sci.* **491,** 159–167 (2015).
22. Das, R., Ali, M. E., Abd Hamid, S. B., Ramakrishna, S. & Chowdhury, Z. Z. Carbon nanotube membranes for water purification: a bright future in water desalination. *Desalination* **336,** 97–109 (2014).
23. Dreyer, D. R., Park, S., Bielawski, C. W. & Ruoff, R. S. The chemistry of graphene oxide. *Chem. Soc. Rev.* **39,** 228–240 (2010).
24. Wilson, N. R. *et al.* Graphene oxide: structural analysis and application as a highly transparent support for electron microscopy. *ACS Nano* **3,** 2547–2556 (2009).
25. Loh, K. P., Bao, Q., Eda, G. & Chhowalla, M. Graphene oxide as a chemically tunable platform for optical applications. *Nat. Chem.* **2,** 1015–1024 (2010).
26. Liu, H. Y., Wang, H. T. & Zhang, X. W. Facile fabrication of freestanding ultrathin reduced graphene oxide membranes for water purification. *Adv. Mater.* **27,** 249–254 (2015).
27. Sun, P. Z. *et al.* Highly efficient quasi-static water desalination using monolayer graphene oxide/titania hybrid laminates. *NPG Asia Mater.* **7,** e162 (2015).
28. Hu, M. & Mi, B. X. Enabling graphene oxide nanosheets as water separation membranes. *Environ. Sci. Technol.* **47,** 3715–3723 (2013).
29. Hung, W. S. *et al.* Cross-linking with diamine monomers to prepare composite graphene oxide-framework membranes with varying *d*-spacing. *Chem. Mater.* **26,** 2983–2990 (2014).
30. Zhang, Y., Zhang, S. & Chung, T. S. Nanometric graphene oxide framework membranes with enhanced heavy metal removal via nanofiltration. *Environ. Sci. Technol.* **49,** 10235–10242 (2015).
31. Greenspan, L. Humidity fixed-points of binary saturated aqueous-solutions. *J. Res. Natl Bur. Stand. Sect. A* **81,** 89–96 (1977).
32. Rezania, B., Severin, N., Talyzin, A. V. & Rabe, J. P. Hydration of bilayered graphene oxide. *Nano Lett.* **14,** 3993–3998 (2014).
33. Radha, B. *et al.* Molecular transport through capillaries made with atomic-scale precision. *Nature* **538,** 222–225 (2016).
34. Tissandier, M. D. *et al.* The proton's absolute aqueous enthalpy and Gibbs free energy of solvation from cluster ion solvation data. *J. Phys. Chem. A* **102,** 7787–7794 (1998).

35. Chekli, L. *et al.* A comprehensive review of hybrid forward osmosis systems: performance, applications and future prospects. *J. Membr. Sci.* **497,** 430–449 (2016).

Acknowledgements

This work was supported by the Royal Society and the Engineering and Physical Sciences Research Council, UK (EP/K016946/1 and EP/M506436/1). K.G. acknowledges Marie Curie International Incoming Fellowship. K.S.V. and R.R.N. acknowledge support from BGT Materials Limited.

Author contributions

R.R.N. designed and supervised the project with J.A. and K.S.V.; J.A. and K.S.V. prepared the samples, performed the measurements and carried out the analysis with help from R.R.N.; J.D., C.D.W. and P.C. carried out MD simulations and data analysis. K.G., Y.S. and C.T.C. helped in sample preparation, characterization and data analysis. E.P. and S.J.H. contributed to sample characterization. A.K.G. participated in discussions and project design. R.R.N., K.S.V., J.A., C.D.W., I.V.G. and A.K.G. wrote the manuscript. All authors contributed to discussions.

Additional information

Supplementary information is available in the online version of the paper. Reprints and permissions information is available online at www.nature.com/reprints. Correspondence and requests for materials should be addressed to R.R.N.

Competing financial interests

The authors declare no competing financial interests.

Methods

Preparation of GO membranes. The aqueous suspension of graphene oxide (GO) was prepared by dispersing millimetre-sized graphite oxide flakes (purchased from BGT Materials Limited) in distilled water using bath sonication for 15 h. The resulting dispersion was centrifuged 6 times at 8,000 r.p.m. to remove the multilayer GO flakes. Subsequently, freestanding GO membranes of thickness ≈100 μm were prepared by vacuum filtration of supernatant GO suspension[4] through an Anodisc alumina membrane filter (0.2 μm pore size and a diameter of 47 mm, purchased from Millipore). As-prepared GO membranes were dried in an oven for 10 h at 45 °C and cut into rectangular strips of dimension of 4 mm × 10 mm (Supplementary Fig. 1).

Tuning interlayer spacing in GO laminates. GO membranes with different interlayer spacing were prepared by storing them in a sealed container with different RH of 0, 12, 33, 75, 84 and 100%. To this end, we used saturated solutions of LiCl (12% RH), $MgCl_2$ (33% RH), NaCl (75% RH) and KCl (84% RH), which were prepared by dissolving excess amounts of salts in deionized water[31,36]. A humidity meter was used inside the container to check that the salts provided the literature values of RH. As a zero humidity environment, we used a glove box filled with Ar and H_2O content below 0.5 p.p.m. 100% RH was achieved inside a sealed plastic container filled with a saturated water vapour at room temperature.

Analysis of the interlayer spacing. X-ray diffraction (XRD) measurements in the 2θ range 5° to 15° (with a step size of 0.02° and recording rate of 0.1 s) were performed using a Bruker D8 diffractometer with Cu Kα radiation ($\lambda = 1.5406$ Å). To collect an XRD spectrum from a GO membrane stored at a specific RH, we created the same humid environment inside a specimen holder (Bruker, C79298A3244D83/85) and sealed it with the GO membrane. For the case of zero humidity, an airtight sample holder (Bruker, A100B36/B37) was used. All spectra were taken with a short scanning time to avoid possible hydration/dehydration of the GO membranes. From XRD analysis of the (001) reflection, d for 0, 12, 33, 75, 84 and 100% RH are found to be 6.4, 7.4, 7.9, 8.6, 9 and 9.8 Å, respectively.

Fabrication of PCGO membranes. After achieving the desired d by using different humidities, each rectangular strip was immediately glued and stacked with Stycast 1266. This stack was then immediately transferred to the same humid environment (where the GO laminates were initially stored) for curing the epoxy overnight. Finally, the resulting stacks were glued into a slot in a plastic or copper plate as shown in Fig. 1. An epoxy layer present at the top and bottom cross-sections of the glued stacks was carefully cleaved to produce a clean surface for permeation experiments. The cleaved cross-section was also checked under an optical microscope to remove any possible epoxy residues. The entire fabrication procedure is illustrated in Supplementary Fig. 1. Swelling of the PCGO membranes on exposure to liquid water was monitored by measuring the cross-sectional thickness of the membranes in an optical microscope immediately after and before performing the ion permeation experiments. The increase in thickness after the permeation experiments was found to be <1%, indicating negligible swelling of PCGO membranes. Similarly, the effect of epoxy encapsulation on d was monitored by measuring the thickness of GO laminates before and after encapsulation. No changes were found. We also carried out an additional check in which the epoxy encapsulation was removed around one of the GO membranes ($d \approx 7.9$ Å) and X-ray measurements were immediately performed. No change in d (with accuracy of 1–2%) was observed, which confirms the stability of d after the encapsulation procedure.

Permeation experiments. All permeation measurements were carried out using the set-up shown in Supplementary Fig. 2, which consists of feed and permeate compartments made from Teflon. PCGO membranes incorporated plastic or metal plates (Supplementary Fig. 1) were clamped between two O-rings and then fixed between the feed and permeate compartments to provide a leak tight environment for the permeation experiments. We filled the compartments with equal volumes (10 ml) of a salt solution (feed) and deionized water (permeate) to avoid any hydrostatic pressure due to different heights of the liquids. Permeation experiments at different temperatures (2–43 °C) were performed in a temperature-controlled environmental chamber. The measurement set-up, feed and permeate solutions were equilibrated at each temperature before performing the experiment. Magnetic stirring was used in both compartments to avoid concentration polarization effects. Anion and cation concentrations in the permeate compartment caused by diffusion through PCGO membranes were accurately measured using ion chromatography (IC) and inductively coupled plasma atomic emission spectrometry (ICP-AES) techniques[4]. Using the known volume of the permeate compartment, the concentrations allowed us to calculate the amount of ions that diffused into it.

Data availability. The data that support the plots within this paper and other findings of this study are available from the corresponding author upon reasonable request. Data related to molecular dynamics simulations are available from P.C. (Paola.Carbone@manchester.ac.uk).

References

36. Rockland, L. B. Saturated salt solutions for static control of relative humidity between 5° and 40° C. *Anal. Chem.* **32,** 1375–1376 (1960).

nature nanotechnology

SUPPLEMENTARY INFORMATION

DOI: 10.1038/NNANO.2017.21

Tunable sieving of ions using graphene oxide membranes

Jijo Abraham, Kalangi S. Vasu, Christopher D. Williams, Kalon Gopinadhan, Yang Su, Christie T. Cherian, James Dix, Eric Prestat, Sarah J. Haigh, Irina V. Grigorieva, Paola Carbone, Andre K. Geim & Rahul R. Nair

1. Fabrication of physically confined GO (PCGO) membranes

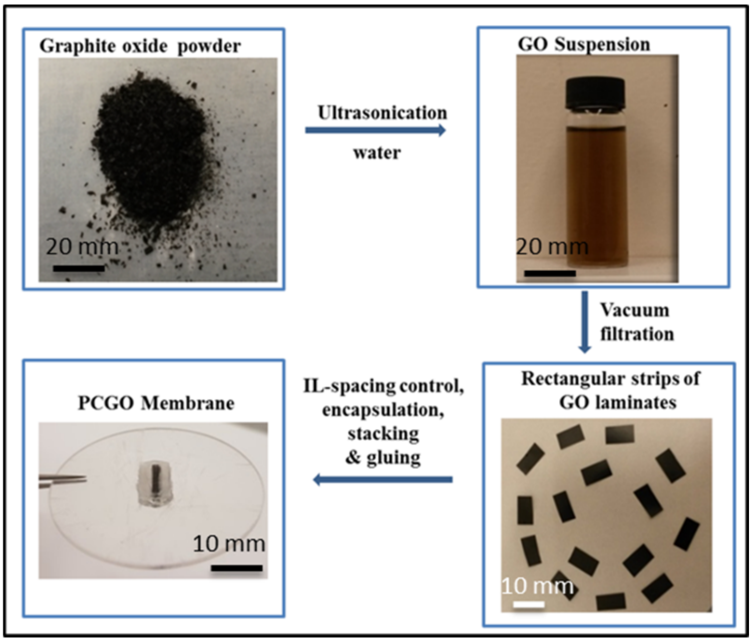

Supplementary Fig. 1. PCGO membrane fabrication. Figure illustrating step-by-step procedure in the fabrication of PCGO membrane.

2. Experimental set-up for permeation experiments

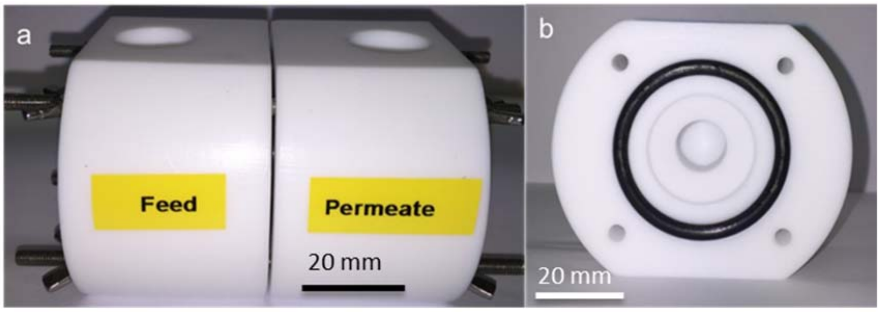

Supplementary Fig. 2. Permeation set-up. (a) Experimental set-up showing Teflon made feed and permeate compartments used for the ion permeation experiments. Membranes were clamped between two O-rings and then fixed between feed and permeate compartments to provide a leak tight environment for the permeation experiments. (b) Cross-sectional view of the feed/permeate compartment showing O-ring arrangement for sealing the membranes.

3. Ion permeation through PCGO membranes

Ion permeation through PCGO membranes was monitored as a function of concentration gradients and duration of the experiment. As an example, supplementary Fig. 3 shows the results for permeation of K^+ and Cl^- ions through PCGO membranes with an interlayer spacing of 9.8 Å. This increases with time in a stoichiometric manner (within our experimental accuracy, as indicated in the figure), to preserve the charge neutrality in both compartments. The slope of such permeation vs time curves gives the permeation rate. As shown in the inset of supplementary Fig. 3, the permeation rate increases linearly with feed concentration, indicating a concentration driven diffusion process[1].

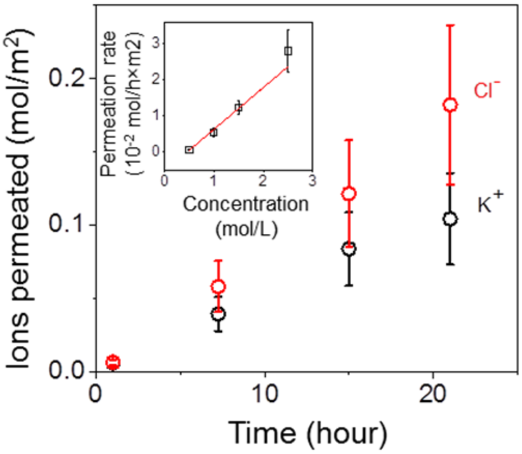

Supplementary Fig. 3. Ion permeation through PCGO membrane. Permeation through a PCGO membrane with an interlayer spacing of 9.8 Å from the feed compartment with 1 M aqueous solution of KCl. The error bars indicate our experimental accuracy (~30%) for this particular type of measurements. The inset shows K^+ ion permeation rate as a function of concentration of the feed solution. Error bars indicate the standard deviation.

4. Tested ions and their hydrated diameters

The hydrated diameters considered for all the ions in Fig. 2 of the main text are obtained from Ref. (2). There are large variations in exact values of hydrated diameters reported in literature[3], due to disparities in the definition and differences in modelling parameters. For example, the reported hydrated diameter of K^+ varies from 4 to 6.6 Å and for Mg^{2+} it varies from 6 to 9.4 Å. The chosen values in the main Fig. 2 are 6.6, 7.1, 7.6, 8.2 and 8.5 Å for K^+, Na^+, Li^+, Ca^{2+} and Mg^{2+} respectively. However, irrespective of the chosen hydrated diameter, the absence of a pure size exclusion mechanism in the ion permeation through PCGO membrane is clear. For example, the smallest reported hydrated diameter for Na^+ ion is 5.4 Å, so it is not expected to permeate through PCGO membranes with an interlayer spacing smaller than 8.8 Å if the permeation cut-off is dictated by the size exclusion. The observed permeation of Na^+ through this membrane confirms that ion permeation through PCGO membranes is not exclusively limited by their hydrated diameter.

5. Water permeation experiments

To understand the permeation of water molecules through PCGO membranes we have performed gravimetric measurements[4] and pressure assisted water permeation experiments. Gravimetric measurements were carried out as reported previously[4] inside a glove box environment (< 0.5 ppm of H_2O) using a stainless steel container sealed with a PCGO membrane. Air-tight sealing was achieved by fixing the PCGO membrane glued plastic plate to a steel container using two rubber O-rings. In a typical experiment, the weight loss of a water filled container sealed with a PCGO membrane was monitored using computer-controlled balance (Denver Instrument SI-203 with a sensitivity of 1 mg). We have performed the weight loss experiments for the PCGO membranes with interlayer spacing, *d*, of 6.4, 7.4, 7.9, 8.6, 9.0 and 9.8 Å to measure the water permeation rate as a function of interlayer spacing. No noticeable weight loss with an accuracy of 0.2 mg/h×cm^2 was observed for the PCGO membranes with 6.4 Å interlayer spacing, indicating that the available free space of ≈ 3 Å is not sufficient for the permeation of water through graphene channels. However, the weight loss rates through PCGO membranes with interlayer spacings of 7.4, 7.9, 8.6, 9.0 and 9.8 Å were measurable and significant: 7.4, 8.8, 10.4, 12.3 and 15.4 mg/h×cm^2, giving a water permeance of 3.2, 3.8, 4.5, 5.3 and 6.6 L/h×m^2×bar, respectively.

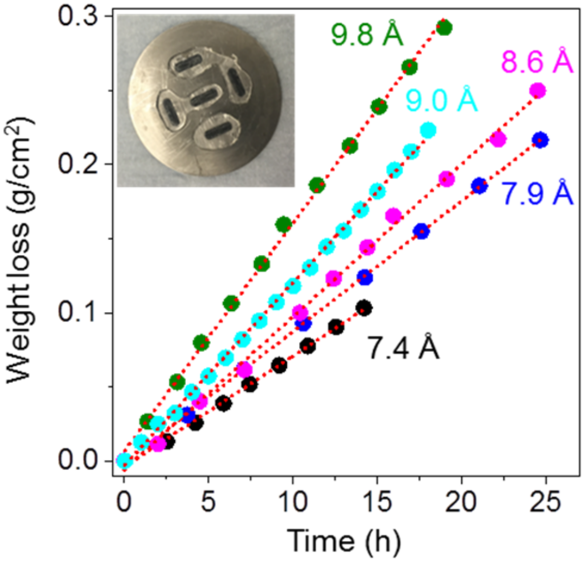

Supplementary Fig. 4. Water permeation through PCGO membrnaes. Weight loss for a container sealed with PCGO membrnaes with different interlayer spacing. Inset shows the PCGO membrane sample used for the pressure filtration experiment (diameter of the disc is 51 mm).

In addition to the gravimetric measurements, we have also estimated the rate of liquid water permeation through PCGO membranes with an interlayer spacing of 7.9 Å using a Sterlitech HP4750 stirred cell. As shown in the inset of supplementary Fig. 4, the area of the membrane available for water permeation was increased by gluing multiple stacks of PCGO samples onto a stainless steel plate to collect a measurable amount of permeated water though PCGO membrane. The typical cross-sectional area and permeation length of the PCGO samples in this experiment was 0.3 cm^2 and 3 mm, respectively. The PCGO membranes assembly was then fixed inside the stirred cell using a rubber gasket to avoid any possible leakage in the experiment. We have used pure water as a feed solution and collected the water on other side by applying a pressure of 15 bar using a compressed nitrogen gas cylinder. Water permeance was found to be ≈ 0.5-1.0 L/h×m^2×bar, which is roughly in agreement with the value obtained from the gravimetric measurements (≈ 4 times smaller). Due to the difficulties of fabricating samples with such large areas for pressure filtration, systematic filtration experiments with salt water were not performed.

Comparison with Hagen-Poiseuille flow equation

Using the standard Hagen-Poiseuille equation with non-slip boundary conditions, we have estimated the water permeation rate through PCGO membranes with different interlayer spacings. Water flow through slit geometry can be described as

$$Q = \frac{1}{12\eta}\frac{\Delta P}{L}\delta^3 W\rho \qquad \text{(S1)}$$

where η is the viscosity of water (1 mPa.s), ΔP is driving pressure, L is the permeation length (3 mm), δ is the effective pore size, W is the lateral width of nanochannels (9 mm) and ρ is the density of water. The water flux through the PCGO membrane can be obtained as $Q \times S$, where S is the area density of nano channels defined as $A/W \times d$, where A is the area and d is the interlayer distance.

For PCGO membranes with an interlayer spacing of 7.4 and 9.8 Å, the estimated water flow rate per cm^2 is ≈ 2×10^{-3} mg/h and 6×10^{-3} mg/h respectively, which is three orders of magnitude lower than the experimentally observed water flow of 7.4 and 15.4 mg/h respectively. That is, water flow through PCGO membranes with interlayer spacings of 7.4 and 9.8 Å exhibits a flow enhancement, compared to the prediction from the Hagen-Poiseuille equation, by a factor of 4000 and 2000, respectively.

6. Molecular Dynamic Simulations

Molecular dynamics simulations (MD simulations) were used to calculate the free energy barriers for ions permeating into modelled graphene channels and the diffusion coefficients of the ions inside the channels. All simulations were performed using GROMACS[5], version 5.0.4, in the NVT ensemble at a temperature of 298.15 K, maintained using the Nose-Hoover thermostat[6,7]. The equations of motion were integrated using the leap-frog algorithm[8] with a time-step of 2 fs. The intermolecular potential between particles i and j, V_{ij}, was evaluated as the sum of a Lennard-Jones 12-6 term and a coulombic term,

$$V_{ij} = 4\varepsilon_{ij}\left[\left(\frac{\sigma_{ij}}{r_{ij}}\right)^{12} - \left(\frac{\sigma_{ij}}{r_{ij}}\right)^{6}\right] + \frac{q_i q_j}{4\pi\varepsilon_0 r_{ij}} \qquad \text{(S2)}$$

for which the coulombic term was evaluated using the particle-mesh Ewald[9,10] summation. In Equation S2, r_{ij} is the distance between the two particles with charges q_i and q_j and ε_0 is the vacuum permittivity. In the 12-6 potential, the cross parameters for unlike atoms, σ_{ij} and ε_{ij}, were obtained using the Lorentz-Berthelot combining rules,

$$\sigma_{ij} = \frac{(\sigma_i + \sigma_j)}{2} \qquad \text{and} \qquad \varepsilon_{ij} = (\varepsilon_i \varepsilon_j)^{\frac{1}{2}} \qquad \text{(S3)}$$

where σ_i and ε_i are the parameters corresponding to an individual atom. Individual carbon atoms in the graphene sheets were modelled as rigid and with zero charge. The parameters for the carbon atoms were obtained from a study in which the water contact angle and adsorption energy were reproduced[11]. The ion parameters were taken from studies in which the hydration free energy and hydrated radius of each ion were calculated and fitted to experimental quantities in bulk solution[12,13]. The original parameterizations of both the carbon and ions were conducted using the SPC/E water model[14] so we have used this model in our simulations. Non-bonded interactions were cutoff for $r_{ij} < 1.0$ nm. The full set of non-bonded interaction parameters used in the simulations is given in Table S1.

Supplementary Table 1. Non-bonded interaction parameters used in this work.

i	σ_i (nm)	ε_i (kJ mol^{-1})	q_i (e)
C	0.3214	0.48990	0.000
K^+	0.4530	0.00061	1.000
Na^+	0.3810	0.00061	1.000
Li^+	0.2870	0.00061	1.000
Ca^{2+}	0.2410	0.94000	2.000
Mg^{2+}	0.1630	0.59000	2.000

Free Energy Barriers

The free energy barrier simulations were set up in a similar manner as described in much greater detail in our previous simulations[15]. Briefly, this consists of five layers of graphene sheets, centered in the x-direction and stacked parallel in the z-direction, with an interlayer spacing of 7, 8, 9, 10 and 11 Å. The interlayer space and adjoining reservoirs were filled with water molecules. A single ion (either Li^+, Na^+, K^+, Mg^{2+} or Ca^{2+}) was then swapped for one of the water molecules in the left-hand reservoir to generate the initial configuration (Supplementary Fig. 5).

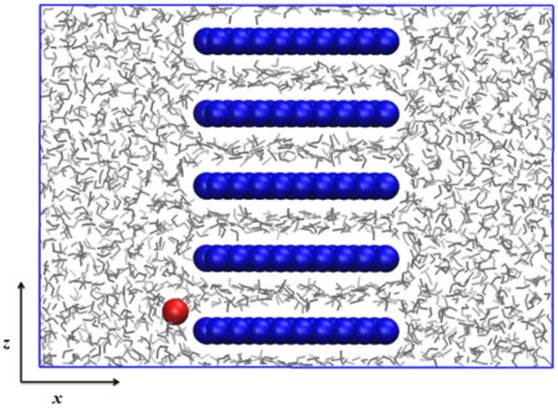

Supplementary Fig. 5. Free energy barrier simulations. A snapshot of the simulation cell used in the free energy barrier simulations. The red sphere, blue spheres, and grey lines represent the ion, carbon atoms and water molecules, respectively.

In order to obtain the energy barriers, a potential of mean force (PMF) describing the process of the ion entering the model membrane was generated for every ion and interlayer spacing. This was calculated using an umbrella sampling procedure[16,17] involving 50 separate simulations, spanning the distance from the center of the reservoir ($x = 0.1$ nm) to the center of the channel ($x = 2.5$ nm), at 0.05 nm intervals. In each simulation, the position of the ion in the x direction was restrained using a harmonic potential with a force constant of 5000 kJ mol^{-1} nm^{-2}. After an initial equilibration period of 1 ns, the PMF was generated from the force data obtained in a further 4 ns of simulation time, using the weighted histogram analysis method[18,19]. The maximum energy along the PMF profile is equal to the barrier to permeation. In all cases, the observed barriers are positive, indicating that this process is energetically unfavorable. In general, the barrier height increases as the interlayer spacing decreases and, in the narrowest capillaries, the barriers are considerably larger for divalent ions than monovalent ions. Fig. 3c inset in the main text and supplementary Table 2 show the free energy barriers for every ion obtained for different interlayer spacing.

Supplementary Table 2. Free energy barriers to ion permeation into graphene capillaries (kJ mol^{-1}). The number in brackets is the uncertainty in the size of the barrier.

Ion	**Interlayer Spacing (Å)**				
	7	**8**	**9**	**10**	**11**
K^+	27.5(0.6)	17.4(0.3)	10.8(0.3)	5.6(0.2)	5.6(0.3)
Na^+	22.0(1.1)	15.9(0.3)	5.3(0.4)	5.0(0.3)	5.3(0.3)
Li^+	24.7(1.3)	8.5(0.3)	4.5(0.4)	3.2(0.3)	1.8(0.2)
Ca^{2+}	163.5(1.0)	60.3(0.4)	3.9(0.3)	5.5(0.4)	6.7(0.4)
Mg^{2+}	197.8(2.2)	44.3(0.5)	4.6(0.3)	3.9(0.4)	5.4(0.4)

The observed trends in barrier energy suggest that the size of the barrier is related to the hydration free energy. The higher charge on divalent ions results in stronger electrostatic attraction between the ion and the surrounding water, and the strength of these interactions is reflected in the magnitude of their experimental hydration free energies (see Supplementary Table 3)[20,21]. Hence, ions with the most negative hydration free energies have the largest barriers to permeation, consistent with permeation data obtained experimentally.

Supplementary Table 3. Experimental hydration free energy of different ions taken from Ref. 2.

Ion	**Hydration free energy (kJ/mol)**
K^+	-321
Na^+	-405
Li^+	-515
Ca^{2+}	-1592
Mg^{2+}	-1922

This ion dehydration effect was further investigated by analyzing the ion hydration numbers in each simulation window along the PMF profile (Supplementary Fig.6 and 7). The hydration numbers for the first, n_1, and second, n_2, hydration shells, were calculated by taking the integral at the first and second minima in the ion-water radial distribution function. The Supplementary Fig. 6a. shows that both n_1 and n_2 decrease as the ions move into a 7 Å channel. Supplementary Fig. 6b. shows that, for K^+, n_1 decreases to the greatest extent in the narrowest channel. There is a small increase in n_1 in the 11 Å channel, relative to bulk solution, and this appears to be because the K-O distance is commensurate with the peaks in the water density profile when K^+ is in the center of the channel. We have discussed this observation in our previous work focusing on anion permeation[15]. Typically, n_1 and n_2 are not integers, because they are averaged over the duration of the simulation and exchange of water molecules between the hydration shells and bulk solution is relatively frequent. However, for the most strongly hydrating ion, Mg^{2+}, n_1 is always an integer. Supplementary Fig. 7 shows the changes in the first hydration number of Mg^{2+} as the ion enters the channel with interlayer spacing of 7 Å, $n_1 = 6.0$ in bulk solution, $n_1 = 5.0$ at the entrance to the channel, and $n_1 = 4.0$ once in the center of the channel.

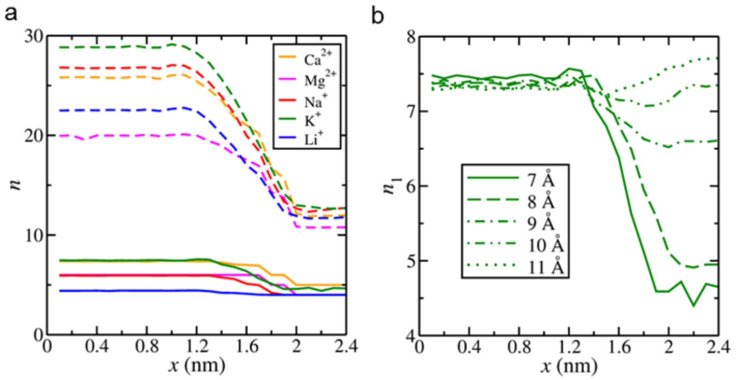

Supplementary Fig. 6. Ion permeation and ion hydration number (a) The decrease in n_1 (solid line) and n_2 (dashed line) as the ions enter a channel with an interlayer spacing of 7 Å. (b) n_1 for K^+ entering channels with interlayer spacing ranging from 7 to 11 Å.

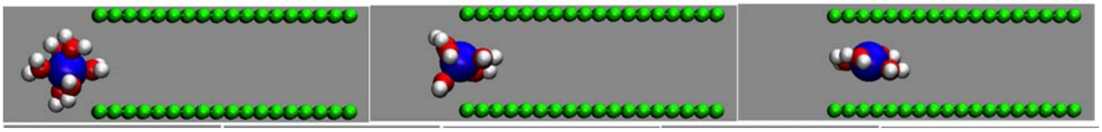

Supplementary Fig. 7. Dehydration of Mg^{2+}. Mg^{2+} (blue) with the first hydration shell entering the 7 Å graphene channel (green) at x = 1.6, 1.8 and 2.0 nm in the simulation box (left to right).

The primary hydration numbers of ions inside the channel were obtained from the last five simulation windows along the PMF profiles. Supplementary Table 4 shows that n_1 decreases with interlayer spacing for all ions. Since the first hydration shell of the Li^+ ion is very small, n_1 is only reduced slightly from 1.1 nm to 0.7 nm. However, for ions with larger ionic radii the decrease in n_1 is more significant. For example, for K^+, n_1 decreases from 7.7 in a 11 Å channel to 4.7 in a 7 Å channel. Combined with the barriers in Supplementary Table 2, this shows that ions with larger electrostatic interaction with the surrounding water molecules hold more water molecules to the primary hydration shell and shows larger energy barrier for permeation. It is interesting to note that for all of the cations there is a maximum in n_1 at some intermediate interlayer spacing. This appears to be the case when the effective interlayer spacing is commensurate with the distance from the ion to the first hydration shell with the ion in the center of the channel. We have also investigated even narrower interlayer spacing (< 0.6 nm) but the channel does not retain any water molecules at this separation so the ions are required to completely dehydrate in order to enter into the membrane in our simulations.

Supplementary Table 4. The number of water molecules in the first hydration shell, n_1.

Ion	**Interlayer Spacing (Å)**				
	7	**8**	**9**	**10**	**11**
K^+	4.7	5.0	6.6	7.4	7.7
Na^+	4.0	4.4	5.6	5.7	5.7
Li^+	4.0	4.0	4.4	4.2	4.2
Ca^{2+}	5.0	7.5	7.9	7.3	7.2
Mg^{2+}	4.0	6.0	6.0	6.0	6.0

All the above calculations have been performed on pristine graphene capillary. Therefore to clarify the role of oxidized regions on the permeation mechanism we have carried out free energy calculations with a deprotonated OH group (the parameters for the oxygen atom, $q = -0.6400$ C, $\sigma = 0.307$ nm, $\varepsilon = 0.65$ kJ/mol were taken from Ref. 22) attached to the carbon atom at the center of the nanochannel with an interlayer spacing of 8 Å. The resulting free energy barrier for K^+ ions turns out to be ~15 kJ/mol similar to that of the pristine channel (17.4 kJ/mol), confirming the dominant importance of the interlayer spacing rather than the chemical functionality for the proposed dehydration mechanism.

Diffusion coefficient of ions inside the sub-nm channels

To calculate the ion's diffusion coefficient, *D,* within the capillary, two graphene sheets with dimensions 6.14 nm x 6.14 nm and interlayer spacing ranging from 7 to 11 Å were used. In this case, unlike the free energy barrier calculations, only one periodic channel was set up, providing an effectively infinitely long 2D capillary for ion diffusion. The density of the water inside the capillary was set up equal to the value obtained from the free energy barrier calculations where the water filled the channel and reached different equilibrium densities as a function of interlayer spacing. After a short equilibration simulation, a single water molecule was exchanged for the ion of interest. Extended simulation runs of 100 ns were used to calculate the mean squared displacement of the ion, and this was used to obtain *D* the from the Einstein relation

$$\left\langle \left| r_i(t_0 + t) - r_i(t_0) \right|^2 \right\rangle = 6Dt \qquad \text{(S4)}$$

where r_i is the position of the particle at time $t_0 + t$ or t_0 and the angled brackets denote ensemble averaging. As well as these simulations, we also calculated the diffusion coefficient of K^+ in an unconfined box of water molecules (bulk), in order to validate the employed parameters. In this case, the simulation box was cubic, with a side length of 7.5 nm and the simulation was run for 10 ns, using only the final 9 ns in the calculation of *D*. In the unconfined system, we obtained $D = 1.60 \times 10^{-5}$ cm^2 s^{-1}, which agrees reasonably well with the experimental bulk diffusion coefficient of 1.96×10^{-5} cm^2 s^{-1} [23]. This shows that our choice of interaction parameters for both the water and K^+ ions produce diffusion coefficient in reasonable agreement with experiment, despite dynamic properties not featuring in the original parameterization of the ion – water intermolecular potential.

In the channel, *D* is reduced relative to the bulk simulation (see supplementary Fig. 8). The difference in diffusion coefficient between bulk and the 8 to 11 Å channel is due to the limited diffusion perpendicular to the graphene sheets. Once the interlayer spacing is reduced below 8 Å, diffusion of K^+ is further reduced relative to the bulk; K^+ is only able to move within the plane of the single water monolayer at these interlayer spacings. The decrease in *D* is however modest compared to the decrease in permeation rates observed experimentally. Thus the exponential decrease in the experimental permeation rate with interlayer spacing cannot be explained by the diffusion-limited permeation. This further suggests that the free energy barrier associated with dehydration is the dominant parameter for the ion permeation in our sub-nm capillaries.

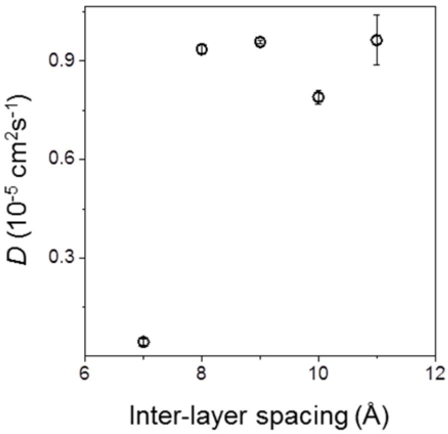

Supplementary Fig. 8. Ion diffusion through sub-nm channels. Diffusion coefficient of K^+ ion in water for interlayer spacing ranging from 7 Å to 11 Å.

Finally, to completely rule out the diffusion contribution on the experimentally observed ion permeation, we have calculated the capillary diffusion activation energies (E_a) of the K^+ ion for interlayer distances of 10, 8 and 7 Å by measuring the ion diffusion coefficient at different temperatures (T). Supplementary Fig. 9 shows that the diffusion process can be described by an Arrhenius relationship from which we can extract E_a. The extracted values of E_a are 15.3 ± 0.4, 12.9 ± 0.3 and 17.7 ± 0.9 kJ mol^{-1} for the interlayer distance 10, 8, and 7 Å, respectively. These values show that E_a is relatively unchanged with interlayer spacing (while the measured barrier increased significantly with decreasing d), hence diffusion cannot explain the experimentally observed ion selectivity in sub-nm channels in PCGO membranes.

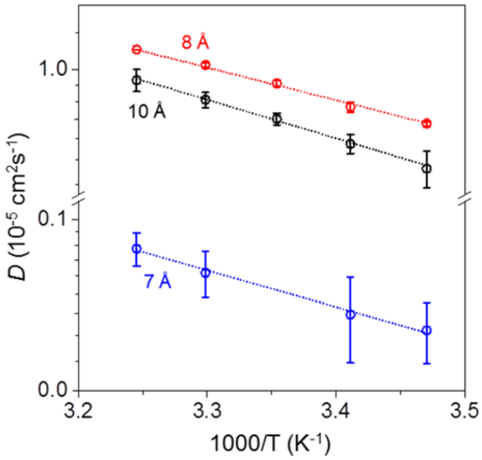

Supplementary Fig. 9. Diffusion activation energy estimation. Temperature dependence of D calculated for K^+ inside a channel of 10, 8, and 7 Å interlayer spacing (Y-axis - natural log scale). The dashed lines are the best fit to calculate the activation energy.

Permeation rate calculations

To further demonstrate the effect of dehydration on ion permeation rates we have calculated the permeation rate of K^+ and Mg^{2+} through a channel with an interlayer spacing of 8 Å. The simulations followed a similar set-up of that used to calculate the energy barrier for ion entry into the channel (Fig S5), except the reservoir of water was larger to allow a concentration of 0.61 mol dm^{-3} of KCl and $MgCl_2$. As at such interlayer spacings there is a large energy barrier associated with the entering of the ions into the channel (Table S2), we do not observe ion permeation over the typical timescale of a simulation. Therefore to calculate the ion permeation rates, a pressure difference of 10 MPa was applied across the simulation cell by adding a constant force on all of the atoms in the simulation box along the direction of the channel, except on those belonging to the graphene sheets[24-27]. During the simulations the temperature was maintained constant at 298.15 K. The interaction parameters for ion, water and graphene atoms were taken the same as the previous simulations. The ion permeation rate was determined by counting the net number of ions that pass from the left to the right reservoir. These simulations were performed for 20 ns, using only the last 15 ns for analysis. The number of K^+ and Mg^{2+} ions permeating through the channel has been plotted against time in Fig. 10. This plot clearly shows that the number of K^+ ions that permeate through the channel is more than that of Mg^{2+} ions and from this, we have calculated a permeation rate for K^+ and Mg^{2+} ions of 1.802(± 0.006) x 10^9 ions s^{-1} and 0.286(± 0.002) x 10^9 ions s^{-1}.

Not surprisingly, these calculated rates are much higher than the experimental values due to the pressure difference applied. However, they clearly show that permeation into the channel is easier for ions with smaller free energy barrier.

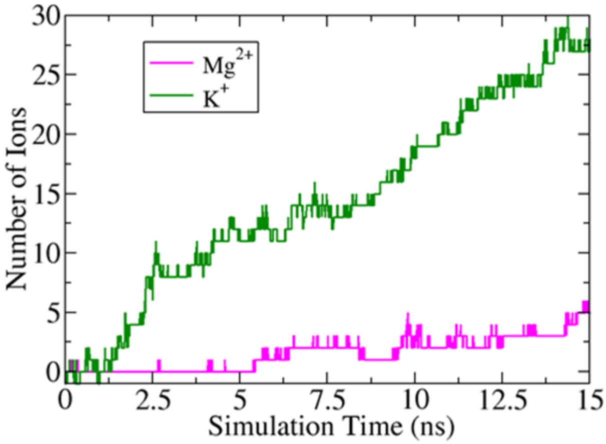

Supplementary Fig. 10. Estimation of Ion permeation rate. Number of ions permeating through a 8 Å channel during the simulation for Mg^{2+} and K^+ with a 10 MPa driving pressure along the channel.

7. Swelling-controlled graphene oxide-graphene (GO-Gr)membranes

On its own, water is a poor solvent for the exfoliation of graphite, whereas surfactant-water solutions can exfoliate graphite to produce stable aqueous dispersions of graphene[28]. Graphene oxide (GO) has previously been suggested as a 2D-surfactant to prepare stable dispersions of graphite and carbon nanotubes (CNTs) in water[29,30]. Here, graphene oxide-graphene (GO-Gr) aqueous dispersions were prepared by exfoliating graphite in water using GO as a surfactant. We have prepared four different concentrations of GO-Gr aqueous dispersions by varying the initial weight of bulk graphite with respect to that of graphite oxide. The graphite oxide to graphite weight ratio was maintained as 1:1, 1:2, 1:5 and 1:9, i.e., four different amounts of graphite (0.175 g, 0.35 g, 0.875 g and 1.575 g) were sonicated for 50 hrs in 120 ml of DI water in the presence of 0.175 g graphite oxide. Resulting GO-Gr dispersion was centrifuged twice for 25 mins at 2500 rpm to remove the unexfoliated graphite and unstable aggregates.

Supplementary Fig. 11 shows the optical photograph of GO and GO-Gr aqueous colloidal suspensions of concentration ≈ 0.1 mg/mL, with increasing amounts of exfoliated graphene (from left to right). The pale brown coloured GO suspension gradually turns into black colour as the amount of exfoliated graphene flakes in GO-Gr dispersions increases. AFM images of the GO-Gr dispersion deposited on oxidised silicon wafer show that most of the exfoliated graphene is a few-layers thick (< 5 nm, see supplementary Fig. 11c). GO-Gr membranes were prepared by vacuum filtering each dispersion through an Anodisc alumina membrane filter (25 mm diameter, 0.02 μm pore size) and drying in ambient condition prior to the permeation and X-ray diffraction experiments.

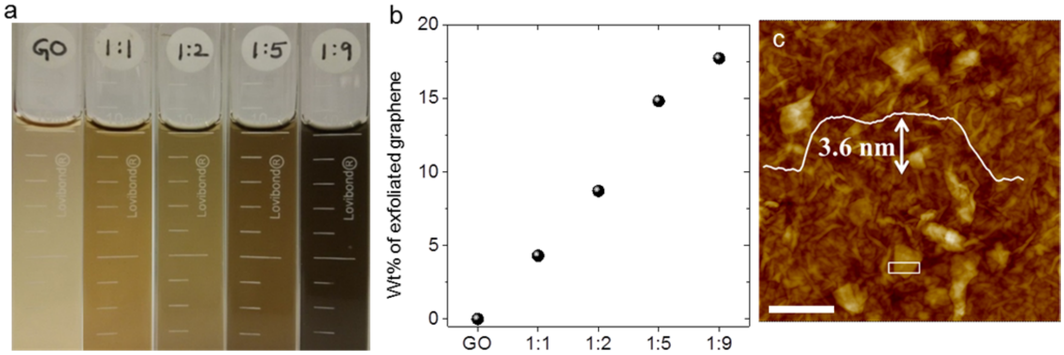

Supplementary Fig. 11. **GO-Gr dispersions** (a) Photograph of GO and GO-Gr aqueous colloidal suspensions (concentration ≈ 0.1 mg/mL) with increasing amount of exfoliated graphene (from left to right). (b) Wt% of exfoliated graphene with respect to GO in different GO-Gr membranes. (c) AFM image of GO-Gr thin film deposited on oxidised silicon wafer showing the presence of exfoliated graphene in GO-Gr film. White curve: height profile along the solid rectangle.Scale bar 0.5 μm.

To estimate the concentrations of exfoliated graphene and GO in the GO-Gr dispersions, we measured the weight of the membranes prepared from the known volume of dispersions. Before weighing, the membranes were completely dried in vacuum and the measurements were performed in a glove box to avoid the influence of absorbed water content in the membranes. Supplementary Fig. 11b shows the weight percentage (wt%) of exfoliated graphene flakes calculated from the weighing measurements for different GO-Gr samples. We found that approximately 18 wt%, 15 wt%, 9 wt% and 4.5wt % of exfoliated graphene (with respect to the weight of GO) in the GO-Gr membranes made from the 1:9, 1:5, 1:2 and 1:1 GO-Gr dispersions, respectively. We note that the estimated wt% of exfoliated graphene flakes in GO-Gr membranes represent the lower bound because we assumed that the concentration GO is the same in pristine GO and GO-Gr dispersions. We have also tried to increase the initial GO-graphite ratio above 1:9 but no appreciable change in the concentration of exfoliated graphene was observed in comparison to 1:9 samples.

Characterization of GO-Gr membranes

Supplementary Fig. 12a shows the cross-sectional SEM image of GO-Gr membrane that confirms the laminar structure similar to the pristine GO membranes. In-plane SEM imaging (Supplementary Fig. 12b) suggests a uniform distribution of exfoliated graphene flakes in GO-Gr membrane. Swelling of GO-Gr membranes in liquid water was probed by X-ray diffraction (see main Fig. 3) that revealed significant changes for GO-Gr membranes compared to pristine GO membranes. For example, interlayer spacing of pristine GO, GO-Gr with 4.5, 9, 15 and 18 wt% graphene are 14, 11.9, 11.5, 10.9 and 10.2 Å respectively in liquid water. GO-Gr membranes with 18 wt% graphene exhibited maximum reductions in swelling (≈ 4 Å) and therefore, we have carried out all the ion permeation and forward osmosis experiments with these samples.

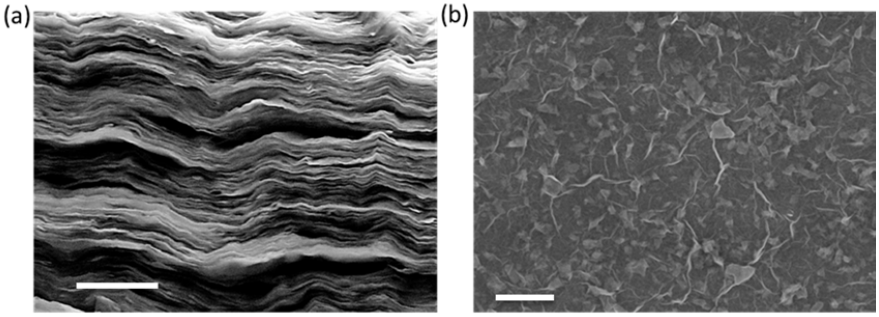

Supplementary Fig. 12. Electron microscopy on GO-Gr membrnae (a) Crosssectional and (b) in-plane scanning electron micrograph from the membrane prepared from the 1:9 GO-Gr dispersion. Scale bars are 1 µm.

Pemeation experiments

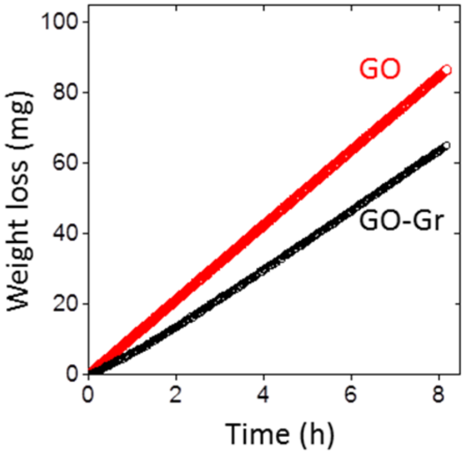

Supplementary Fig. 13. Water permeation through GO-Gr. Weight loss for a container filled water sealed with a GO-Gr and a reference GO membrane with a thickness of 5 µm (Area ≈ 0.5 cm^2).The weight loss rate for GO and GO-Gr membrane is 10.5 and 8.1 mg/h, respectively.

For all ion permeation experiments we used the same set-up (see Supplementary Fig. 2) as that employed for the PCGO membranes. Ion permeation through GO-Gr membranes was studied by separating the feed and permeate compartment by a 5 µm thick GO-Gr membrane on porous Anodisc alumina support glued onto a plastic disc. The feed and permeate compartments were filled with 1 M aqueous solution of various salts (KCl, NaCl, LiCl and $MgCl_2$) and DI water, respectively. Typically, permeation experiments were carried out for 24 hours and the ion permeation was monitored by ion chromatography (IC) and the inductively coupled plasma optical emission spectrometry (ICP-AES). Similar to the PCGO membranes, ion permeation from feed to permeate compartment through GO-Gr membrane is observed to increase with the duration of experiment and feed concentration. Permeation data for GO-Gr membrane with 18 wt% graphene are shown in Fig. 3 of the main text. Compared to pristine GO membranes, the ion permeation rate for GO-Gr membranes is decreased by two to three orders of magnitude. However, when measured by the gravimetric method, water permeation (see supplementary section 5) only showed an approximately 20% reduction with respect to that of pristine GO (supplementary Fig. 13). The relatively small decrease in water permeation and the large decrease in ion permeation through GO-Gr compared to pristine GO membrane confirm that the permeation mechanism for both PCGO and GO-Gr membranes are similar.

To further understand the liquid water flux and salt rejection properties of GO-Gr membranes, we have performed forward osmosis (FO)[31,32] experiments. FO is relatively a new alternative technology to the conventional pressure-driven reverse osmosis (RO) membrane process, where hydraulic pressure is not required for its operation[31,32]. In FO, a concentrated solution of a salt or other molecules (draw solution) is used to generate high osmotic pressure, which pulls the water molecules across a semi-permeable membrane from the low-concentration salt solution (feed solution), effectively filtering the feed water. The draw solute can then be separated from the diluted draw solution to produce clean water. FO has many advantages over conventional RO such as high energy efficiency and low fouling and is considered to be an attractive emerging technology for desalination. The absence of hydraulic pressure in FO makes it highly suitable to evaluate GO-Gr membranes as they have relatively weak mechanical strength. Here, we have performed FO by filling equal volumes (25 mL) of 0.1 M NaCl feed solution and 3 M sucrose draw solution in the feed and permeate compartments, respectively, separated by a GO-Gr membrane (5 μm thick and 0.5 cm^2 area). Nearly 3 M differential concentration leads to a ≈ 75 bar osmotic pressure gradient, which draws water molecules from the NaCl compartment to the sucrose compartment. The amount of water permeation was reflected in the height of sucrose column in the permeate compartment. The observed 0.8 mL increase in the column height over 30 hours corresponds to a water flux of around 0.5 $L/m^2 \times h$. Salt rejection for GO-Gr membrane was estimated by measuring the amount of NaCl in the draw solution. The salt rejection rate was estimated as $1\text{-}C_d/C_f$, where C_d and C_f are the concentrations of NaCl in the draw solution and the feed side, respectively. This yielded a rejection rate of ≈ 97%. For comparison, we have also performed similar FO experiments with pristine GO membranes and the obtained water flux and salt rejection are found to be 0.6 $L/m^2 \times h$ and 60%, respectively. We note that the water flux through GO-Gr membranes is lower than typical FO membranes however it can be improved effectively by decreasing the thickness of GO-Gr membranes. For example, decreasing the GO-Gr membrane thickness from 5 μm to 1 μm yielded the water flux of 2.5 $L/m^2 \times h$ with 94% salt rejection.

Supplementary References

1. Joshi, R. K. *et al.* Precise and ultrafast molecular sieving through graphene oxide membranes. *Science* **343**, 752-754 (2014).
2. Tansel, B. Significance of thermodynamic and physical characteristics on permeation of ions during membrane separation: Hydrated radius, hydration free energy and viscous effects. *Sep. Purif. Technol.* **86**, 119-126 (2012).
3. Marcus, Y. Ionic-Radii in Aqueous-Solutions. *J. Solution Chem.* **12**, 271-275 (1983).
4. Nair, R. R., Wu, H. A., Jayaram, P. N., Grigorieva, I. V. & Geim, A. K. Unimpeded permeation of water through helium-leak-tight graphene-based membranes. *Science* **335**, 442-444 (2012).
5. Van der Spoel, D. *et al.* GROMACS: Fast, flexible, and free. *J Comput Chem.* **26**, 1701-1718 (2005).
6. Nose, S. A molecular-dynamics method for simulations in the canonical ensemble. *Mol. Phys.* **52**, 255-268 (1984).

7. Hoover, W. G. Canonical dynamics - equilibrium phase-space distributions. *Phys. Rev. A* **31**, 1695-1697 (1985).
8. Allen, M. P. & Tildesley, D. J. *Computer simulation of liquids*. (Oxford Univ. Press, Oxford, 1987).
9. Darden, T., York, D. & Pedersen, L. Particle mesh Ewald - an N.Log(N) method for Ewald sums in large systems. *J. Chem. Phys.* **98**, 10089-10092 (1993).
10. Essmann, U. *et al.* A smooth particle mesh Ewald method. *J. Chem. Phys.* **103**, 8577-8593 (1995).
11. Werder, T., Walther, J. H., Jaffe, R. L., Halicioglu, T. & Koumoutsakos, P. On the water-carbon interaction for use in molecular dynamics simulations of graphite and carbon nanotubes. *J. Phys. Chem. B* **107**, 1345-1352 (2003).
12. Horinek, D., Mamatkulov, S. I. & Netz, R. R. Rational design of ion force fields based on thermodynamic solvation properties. *J. Chem. Phys.* **130,** 124507 (2009).
13. Mamatkulov, S., Fyta, M. & Netz, R. R. Force fields for divalent cations based on single-ion and ion-pair properties. *J. Chem. Phys.* **138,** 024505 (2013).
14. Berendsen, H. J. C., Grigera, J. R. & Straatsma, T. P. The missing term in effective pair potentials. *J. Phys. Chem.* **91**, 6269-6271 (1987).
15. Williams, C. D. & Carbone, P. Selective removal of technetium from water using graphene oxide membranes. *Environ. Sci. Technol.* **50**, 3875-3881 (2016).
16. Torrie, G. M. & Valleau, J. P. Monte-Carlo free-energy estimates using non-Boltzmann sampling - application to subcritical Lennard-Jones fluid. *Chem. Phys. Lett.* **28**, 578-581 (1974).
17. Torrie, G. M. & Valleau, J. P. Non-physical sampling distributions in Monte-Carlo free-energy estimation - umbrella sampling. *J. Comput. Phys.* **23**, 187-199 (1977).
18. Kumar, S., Bouzida, D., Swendsen, R. H., Kollman, P. A. & Rosenberg, J. M. The weighted histogram analysis method for free-energy calculations on biomolecules .1. The method. *J. Comput. Chem.* **13**, 1011-1021 (1992).
19. Hub, J. S., de Groot, B. L. & van der Spoel, D. g_wham-A free weighted histogram analysis implementation including robust error and autocorrelation estimates. *J. Chem. Theory Comput.* **6**, 3713-3720 (2010).
20. Marcus, Y. Thermodynamics of solvation of ions .5. Gibbs free-energy of hydration at 298.15 K. *J. Chem. Soc. Faraday T* **87**, 2995-2999 (1991).
21. Tissandier, M. D. *et al.* The proton's absolute aqueous enthalpy and Gibbs free energy of solvation from cluster ion solvation data. *J. Phys. Chem. A* **102**, 7787-7794 (1998).
22. Birkett, G. R. & Do, D. D. Simulation study of water adsorption on carbon black: The effect of graphite water interaction strength. *J. Phys. Chem. C* **111**, 5735-5742 (2007).
23. Marcus, Y. *Ion properties*. (Dekker, 1997).
24. Corry, B. Designing carbon nanotube membranes for efficient water desalination. *J. Phys. Chem. B* **112**, 1427-1434 (2008).
25. Corry, B. Water and ion transport through functionalised carbon nanotubes: implications for desalination technology. *Energy Environ. Sci.4, 751-759 (2011).*
26. Zhu, F.,Tajkhorshid, E. & Schulten, K. Pressure-induced water transport in membrane channels studied by molecular dynamics. *Biophys. J.* **83**, 154-160 (2002).
27. Zhu, F.,Tajkhorshid, E. & Schulten, K. Theory and simulation of water permeation in aquaporin-1. *Biophys. J.* **86**, 50-57 (2004).
28. Lotya, M. *et al.* Liquid phase production of graphene by exfoliation of graphite in surfactant/water solutions. *J. Am. Chem. Soc.* **131**, 3611-3620 (2009).
29. Kim, J. *et al.* Graphene oxide sheets at interfaces. *J. Am. Chem. Soc.* **132**, 8180-8186 (2010).

30. Luo, J. Y. *et al.* Graphene oxide nanocolloids. *J. Am. Chem. Soc.* **132**, 17667-17669 (2010).
31. Cath, T. Y., Childress, A. E. & Elimelech, M. Forward osmosis: Principles, applications, and recent developments. *J. Membrane Sci.* **281**, 70-87 (2006).
32. Zhao, S. F., Zou, L., Tang, C. Y. Y. & Mulcahy, D. Recent developments in forward osmosis: Opportunities and challenges. *J. Membrane Sci.* **396**, 1-21 (2012).

References

1. O'Hern, S. C.; Boutilier, M. S. H.; Idrobo, J.-C.; Song, Y.; Kong, J.; Laoui, T.; Atieh, M.; Karnik, R. *Nano Lett.* **2014,** 14, (3), 1234-1241.

2. Rollings, R. C.; Kuan, A. T.; Golovchenko, J. A. *Nature Commun*. **2016,** 7.

3. Jain, T.; Rasera, B. C.; Guerrero, R. J. S.; Boutilier, M. S. H.; O'Hern, S. C.; Idrobo, J.-C.; Karnik, R. *Nat. Nanotechnol.* **2015,** 10, (12), 1053-1057.

4. Surwade, S. P.; Smirnov, S. N.; Vlassiouk, I. V.; Unocic, R. R.; Veith, G. M.; Dai, S.; Mahurin, S. M. *Nat. Nanotechnol.* **2015,**459–464.

5. Wang, E. N.; Karnik, R. *Nat. Nanotechnol.* **2012,** 7, (9), 552-554.

6. Cohen-Tanugi, D.; Grossman, J. C. *Nano Lett.* **2012,** 12, (7), 3602-3608.

7. Wang, L.; Drahushuk, L. W.; Cantley, L.; Koenig, S. P.; Liu, X.; Pellegrino, J.; Strano, M. S.; Scott Bunch, J. *Nat. Nanotechnol.* **2015,** 10, (9), 785-790.

8. Sahu, S.; Ventra, M. D.; Zwolak, M. *Nano Lett.***2017**, 17, 4719–4724.

9. Richards, L. A.; Schäfer, A. I.; Richards, B. S.; Corry, B. *Small* **2012,** 8, (11), 1701-1709.

10. Thomas, M.; Corry, B.; Hilder, T. A. *Small* **2014,** 10, (8), 1453-1465.

11. Song, C.; Corry, B. *J. Phys. Chem. C* **2009,** 113, (21), 7642-7649.

12. Werber, J. R.; Osuji, C. O.; Elimelech, M. *Nat Rev Mater***2016,** 1, 16018.

13. Li, J.-R.; Sculley, J.; Zhou, H.-C. *Chemical Reviews* **2012,** 112, (2), 869-932.

14. Pendergast, M. M.; Hoek, E. M. V. *Energy Environ. Sci***2011,** 4, (6), 1946-1971.

15. Daer, S.; Kharraz, J.; Giwa, A.; Hasan, S. W. *Desalination* **2015,** 367, 37-48.

16. Das, R.; Ali, M. E.; Hamid, S. B. A.; Ramakrishna, S.; Chowdhury, Z. Z. *Desalination* **2014,** 336, 97-109.

17. Dreyer, D. R.; Park, S.; Bielawski, C. W.; Ruoff, R. S. *Chem. Soc. Rev.* **2010,** 39, (1), 228-240.

18. Nair, R. R.; Wu, H. A.; Jayaram, P. N.; Grigorieva, I. V.; Geim, A. K. *Science* **2012,** 335, (6067), 442-444.

19. Akbari, A.; Sheath, P.; Martin, S. T.; Shinde, D. B.; Shaibani, M.; Banerjee, P. C.; Tkacz, R.; Bhattacharyya, D.; Majumder, M. *Nat Commun.* **2016,** 7.

20. Liu, G.; Jin, W.; Xu, N. *Chem. Soc. Rev.***2015,** 44, (15), 5016-5030.

21. Joshi, R. K.; Carbone, P.; Wang, F. C.; Kravets, V. G.; Su, Y.; Grigorieva, I. V.; Wu, H. A.; Geim, A. K.; Nair, R. R. *Science* **2014,** 343, (6172), 752-754.

22. Li, H.; Song, Z.; Zhang, X.; Huang, Y.; Li, S.; Mao, Y.; Ploehn, H. J.; Bao, Y.; Yu, M. *Science* **2013,** 342, (6154), 95-98.

23. Sun, P.; Zhu, M.; Wang, K.; Zhong, M.; Wei, J.; Wu, D.; Xu, Z.; Zhu, H. *ACS Nano* **2013,** 7, (1), 428-437.

24. Su, Y.; Kravets, V. G.; Wong, S. L.; Waters, J.; Geim, A. K.; Nair, R. R. *Nat Commun.* **2014,** 5, 4843.

Blank Page

Chapter 5- Conclusions and Future Outlook

Blank Page

5.1 Conclusions

The work presented in this thesis focuses on the water/ion transport through GO membrane with an emphasis on the mechanism of ion permeation in channels of size smaller or comparable to the hydrated ion diameter.

GO membranes show some exceptional molecular permeation properties with a promise for desalination technologies. But, the swelling of GO capillaries when exposed to water increases the free space available for permeation to 10 Å, which is larger than the diameter of hydrated ions of common salts, limiting its usage for water treatment applications. A number of approaches have been tried recently to restrict the swelling in GO, for example, thermal treatment and chemical approaches. However, controlled tuning of the interlayer spacing and precise ionic sieving has not yet been achieved. Here by physical confinement, we demonstrated the possibility to control the interlayer spacing in GO membranes below 10 Å. This is a new regime, where the capillary size is smaller than the hydrated ion diameter size. Regardless of steric effects, some ions pass through the membranes even though the capillary size is smaller than the hydrated ion diameter size. Membranes with an interlayer spacing of 9.8 and 7.4 Å completely block the passage of Mg^{2+}, but permitting the passage of K^+ ions. Unlike the size exclusion mechanism, ion permeation rates through graphene oxide membranes with sub-nanometre channels are governed by the energy barrier for ions entry to the capillary as evident from the Arrhenius behaviour of ion permeation rates. The slower permeation rate of ions is described in terms of this activation barrier that originates because of the required reconfiguration of the water shell or partial dehydration of the ions so that they can fit inside the sub nanometre capillaries of the GO membrane. The ease of shredding the water molecules from the hydration shell of the ions depends on the hydration free energy which scales with ion charge, accounting for the permeation differences between monovalent and divalent cations. The relatively small impedance for water permeation is explained by the smaller energy barrier for water molecules entering the channels due to the weaker water-water interaction and enhanced water transport through graphene nanochannels.

Another interesting observation of this work is the very high water-ion selectivity demonstrated by the sub nanometre graphene capillaries. The current research direction in membrane technology has mostly focussed on improving the water flux through the membrane, which occurs at the expense of reduced salt rejection. Without sacrificing the water flux through it, an alternative strategy is to develop membranes exhibiting good water-ion selectivity. Coming to this point, the results we demonstrated for the PCGO membrane appeal promising. For instance, the membrane showed an increase in the water-ion selectivity by more than an order of magnitude when inter-layer spacing is decreased from 9.8 Å to 7.4 Å. Realization of a scalable membrane with excellent water-ion selectivity combined with atomic scale pore tunability (down to sub angstrom precision) is believed to be a promising finding, providing new opportunities to fabricate membranes with on-demand filtration capabilities in the quest for the production of safe drinking water.

5.2 Future Outlook

Controlling ion behaviour in external electric field under extreme confinement has been a major research area in naofluidics. From a fundamental point of view, novel transport properties and phenomena are expected to emerge from the coupled effect of surface chemistry and extreme confinement in the nanoscale regime, and such novel aspects of fluid phenomena may lead to technological breakthroughs. In this regard, PCGO membrane is an ideal system to probe the ions behaviour to external electrical stimulus under such ultra-narrow confinement. Another interesting area is called osmotic blue energy conversion. Creating a salinity gradient between the interfaces of an ion selective membrane has been identified as a promising, clean and renewable source of energy-so-called osmotic blue energy. Intrinsic ion selectivity of PCGO membrane shows a great potential for osmotic blue energy conversion.